Novel characterisation of concentrated dispersions by *in situ* acoustic backscatter systems

Jaiyana Bux

School of Chemical and Process Engineering

University of Leeds

Submitted in accordance with the requirements for the degree of

Doctor of Philosophy

May 2016

The candidate confirms that the work submitted is her own, except where work which has formed part of jointly authored publications has been included. The contribution of the candidate and the other authors to this work has been explicitly indicated below. The candidate confirms that appropriate credit has been given within the thesis where reference has been made to the work of others.

Chapter four is based on the paper: *Bux J., Manga M.S., Hunter T.N. and Biggs S. 2016 "Manufacture of poly(methyl methacrylate) microspheres using membrane emulsification", Phil. Trans. R. Soc. A. 374:20150134*. The candidate was responsible for the experiments, analysis, figures, calculatations and proof reading. The research was driven by Biggs whom wrote the paper, Hunter provided supervisory support, Manga provided experimental support, and all authors provided comments on the content of the paper.

For Nabeel and my girls, Jannah & Inaaya.

Acknowledgements

I would first like to take a moment to thank Timothy Hunter, my primary supervisor, for not only his formal support, but for always being there, encouraging and supporting me, and always taking the time to listen and guide. I would also like to thank my supervisors Jeff Peakall and Simon Biggs. Jeff was always there when needed and happy to provide input, as well as correct my spelling and grammar mistakes on innumerable occasions, and Simon was always happy to provide guidance when needed. I also truly appreciate the support that all three gave me when I had my second child halfway through my PhD.

This research was funded by the EPSRC and the Nuclear Decommissioning Authority (supervised by Dave Goddard from the National Nuclear Laboratory. Part of the research was conducted at the National Nuclear Laboratory with Jonathan Dodds. I am grateful for having had the opportunity to link my research directly with industry, which has been both stimulating and motivating.

I would like to thank each and everyone of my friends and colleagues made along the way, whom made it an inspiring and enjoyable journey, and for providing much needed distractions in the office. In particular I would like to thank Helen Freeman for our frequent lunch dates, joining me and my baby for pram runs in the park and always being there. I am grateful for all of the support I have had from numerous colleagues with respect to experimental work, and I would especially like to thank Susanne Patel.

I am grateful to my two little girls, Jannah and Inaaya, for their infinite amounts of patience and never complaining about constantly

having to hear, "mummy needs to do some work now." My family and my mother-in-law for making the trip to look after my girls when they could. And lastly, my husband for his unwavering support, continued encouragement and guidance, helping me out every time I got stuck on a problem, putting up with my wobbles, and helping me see the light at the end of the tunnel. This wouldn't have been possible without him and I cannot begin to thank him enough.

- Jaiyana Bux, May 2016

Abstract

A range of concentrated dispersions were characterised via a novel *in situ* acoustic backscattering technique. Knowledge of suspension dynamics and concentration is critical for the optimisation of processes which incorporate dispersion systems. The ability to measure and understand these parameters is challenging. Acoustic Backscatter Systems (ABS) offer *in situ* measurement capability in laboratory and industrial suspensions, where the application of other devices is negated due to high concentration or intrusive probe configurations. A robust analytical protocol was established via the ABS, for the characterisation of arbitrary particle types, in any concentration range up to the associated acoustic penetration depth limit.

ABS measurements were analysed via the Rice method (Rice *et al.*, 2014), which was verified herein for relatively larger scale dispersions. This approach enabled quantification of the sediment attenuation constants for a range of particles; barium sulfate (inorganic mineral), oil-in-water emulsions, latex beads and aggregated latex beads, for the first time here, as well as spherical glass beads. A calibration protocol was established for backscattering transducers, with improved data quality and a reduction in experimentation times, relative to published protocolS (Betteridge *et al.*, 2008). This facilitated the decoupling of the transducer constant K_t, from the system constant K_sK_t, enabling quantification of the sediment backscattering constants K_s, for the aforementioned particles. The measured constants for all particles were compared, highlighting the differing scattering influences dominating particles with contrasting physical properties. Importantly this information was extracted via a direct measurement approach,

which didn't require exhaustive derivation of the form function f and the total normalised scattering cross-section χ. f and χ for all particles were normalised with respect to particle density to enable direct comparison. These data highlighted that f and χ do not follow the assumed trend in the lower range of the Rayleigh scattering regime.

The ABS was calibrated for a barium sulfate dispersion, to extract the relationship between measured signal, in the G function form from the Rice method, and concentration. This overcame the non-linearity between concentration and directly measured attenuation. Importantly for the first time, this reference relationship facilitated the qualitative characterisation of an analogous dispersion within an industrial scale tank. Specifically, the tank system utilised impinging jet ballasts to resuspend settled sediment, and air-lifts to homogenise a non-active dispersion, analogous to a radioactive system at Sellafield Ltd (Cumbria, UK). The Rice analysis method proved to be a powerful technique for understanding the mixing and settling dynamics of a complex, large scale processes. The corresponding information was invaluable for mediating operational optimisation, and modelling for future decommissioning operations, of an inaccessible radio-toxic system.

The characterisation of legacy waste suspensions comprising organic flocs, is a current challenge in the nuclear industry. Indeed, aggregated dispersions are abundant, yet their acoustic response is not yet well characterised. A robust, efficient, novel process was established for the manufacture of low density organic Latex particles on a litre scale, within a 'controlled' jetting regime. The dispersions were readily aggregated, and marked differences were observed in their acoustic response with respect to un-aggregated beads. Very complex behaviour was observed, owing to the highly networked structure of the thermally attenuating particles.

Abbreviations

Greek Symbols

α	m^{-1}	Attenuation Coefficient
α_w	m^{-1}	Attenuation due to Water
α_s	m^{-1}	Sediment Attenuation Coefficient
α_{sc}	m^{-1}	Attenuation due to Scattering Effects
α_{th}	m^{-1}	Attenuation due to Thermal Effects
α_{vi}	m^{-1}	Attenuation due to Visco-Inertial Effects
γ	$\mathrm{N\,m}^{-1}$	Interfacial Tension
γ_0	$^\circ$	Beam Divergence Angle
δ_t	m	Thermal Skin Depth
δ_v	m	Viscous Skin Depth
λ	m	Wavelength
μ_c	$\mathrm{kg\,m}^{-1}\,\mathrm{s}^{-1}$	Viscosity (Continuous Phase)
μ_v	$\mathrm{kg\,m}^{-1}\,\mathrm{s}^{-1}$	Viscosity
ν_c	$\mathrm{m\,s}^{-1}$	Velocity (Continuous Phase)
ν_d	$\mathrm{m\,s}^{-1}$	Velocity (Dispersed Phase)
ξ	$\mathrm{kg}^{-1}\,\mathrm{m}^{-2}$	Sediment Attenuation Constant
ρ	$\mathrm{kg\,m}^{-3}$	Density
ϱ	-	Specific Gravity
σ	-	Standard Deviation
σ_t	m^2	Scattering Cross-Section
τ	$\mathrm{W\,m}^{-1}\,\mathrm{K}^{-1}$	Thermal Conductivity
ϕ	m	Diameter
χ	-	Total Normalised Scattering Cross-Section
ψ	-	Near-Field Correction Factor
ω	$\mathrm{rad\,s}^{-1}$	Angular Frequency

Roman Symbols

a	m	Particle Radius

a_t	m	Transducer Active Element Diameter
c	$\mathrm{m\,s^{-1}}$	Speed of Sound
Ca_c	-	Capillary Number (Continuous Phase)
C_p	$\mathrm{J\,kg^{-1}\,°C^{-1}}$	Specific Heat Capacity
C_μ	%	Coefficient of Variation
D	m	Pore Diameter
$\mathrm{D_t}$	m	Transducer Active Element Diameter
$\mathrm{D_{[50]}}$ or $\mathrm{d_{50}}$	µm	Mean Particle Diameter
f	-	Form Function
f_r	MHz	Frequency
G		G Function Defined as $\ln(\mathrm{Vr}\psi)$
k	$\mathrm{m^{-1}}$	Wavenumber
$\mathrm{K_s}$	$\mathrm{m\,kg^{-1/2}}$	Backscattering Constant
$\mathrm{K_t}$	$\mathrm{V\,m^{3/2}}$	Transducer Constant
M	$\mathrm{kg\,m^{-3}}$	Concentration
N	m	Focus Point
P	Pa	Pressure
r	m	Transducer Range
T	°C	Temperature
$\mathrm{V_{RMS}}$	V	Root-Mean-Square Voltage
We_d	-	Weber Number (Dispersed Phase)
x	-	Defined as $x = ka$

Acronyms

ABS	Acoustic Backscatter System
FTR	Four Tenths Scale Rig
HAST	Highly Active Storage Tank
ME	Membrane Emulsification
MMA	Methyl Methacrylate
PMMA	Poly Methyl Methacrylate
PVA	Poly Vinyl Alcohol
SDS	Sodium Dodecyl Sulfate
SNF	Spent Nuclear Fuel
XME	Cross-Flow Membrane Emulsification

Contents

List of Figures

Chapter 1

Introduction, Literature Review & Theory

Chapter 1 is presented in four parts. First an introduction explaining the drive behind this research project is given. A literature review of the current status of suspension characterisation techniques is then provided. Subsequently the principles of acoustic backscatter and the associated theory are discussed in detail. The discussion incorporates aspects related to rigid, soft and flocculated particle dispersions. The chapter then closes with an outline of the research objectives and an outlook of the research progression in subsequent chapters to achieve these.

1.1 Introduction

This project stems from the ubiquitous desire of numerous industries to characterise particle dispersions online and *in situ*. Emulsions, colloidal dispersions, larger particulate suspensions and slurries are encountered in a vast range of industries, from pharmaceutical, personal care, cosmetics, pigments and food manufacture (Hazlehurst *et al.*, 2014), to large scale multiphase separation processes in fuels, lubricants, water, sewage and nuclear waste treatment (Challis *et al.*, 2005). Having knowledge of dispersion properties such as concentration, settling kinetics, particulate segregation and thickening is often critical from operational perspectives and optimisation purposes. Such information is not easily acquired

in situ, and is often determined via labour intensive *ex situ* approaches which require sampling (De Clercq *et al.*, 2008; Iritani *et al.*, 2009), and from theoretical models of the processes (Betancourt *et al.*, 2014). Some *in situ* monitoring devices are commercially available (see section 1.2.1), however their employment in industry is typically limited by dilute concentration thresholds, application complexity and high associated costs (Shukla *et al.*, 2007). Similarly, suitable *in situ* devices which enable vertical depth profiling on a smaller laboratory scale are also lacking (Cheung *et al.*, 1996). For example, sedimentation studies for multiphase sedimentation model development, are usually conducted with instruments which acquire cross-sectional data with separate transmitter and receiver probes, rather than depth-wise profiles (Deboeuf *et al.*, 2011; Hernando *et al.*, 2015; Hoyos *et al.*, 1994). There is a gap in the market with respect to convenient instrumentation and techniques which enable online *in situ* monitoring and characterisation capabilities, for concentrated dispersions comprising arbitrary particles (discussed later in section 1.2).

Acoustic waves can propagate in opaque suspensions and thus provide a route to characterising concentrated dispersion systems (Temkin, 1998).Various groups have demonstrated the use of diagnostic ultrasonic devices for dispersion characterisation (Dukhin & Goetz, 2001; Hunter *et al.*, 2011; McClements, 1991; Norisuye, 2016; Weser *et al.*, 2014; Zou *et al.*, 2014). There has been increasing interest in their application for particle size measurement in opaque dispersions in pharmaceuticals, food and chemical manufacture (Hazlehurst *et al.*, 2014), and also suspended sediment concentration in marine applications (Thorne & Hanes, 2002). Although various *ex situ* instrumentation has been developed for characterisation of dispersions from low to high volume fractions (up to 40 vol% (Dukhin & Goetz, 2001)), the potential has not been exploited for *in situ* instrument development in the same way, mainly because the theoretical backing for current *in situ* devices breaks down in concentration regimes $>2\,\mathrm{g\,l^{-1}}$ (Hunter *et al.*, 2012a). Acoustic Backscatter Systems (ABS) are one such type of device. They are commercially available and utilised for the characterisation of dilute sandy sediments in estuarine sediment transport studies (Thorne & Hanes, 2002). The aim of this project is to expand knowledge and understanding in the underlying theoretical basis of the ABS and develop a methodology for its application as an *in*

situ online monitoring and characterisation device for concentrated dispersions of arbitrary particle types.

There is currently significant interest from the UK nuclear energy industry for *in situ* instrumentation of this kind, in particular for the monitoring and characterisation of legacy waste sludges and suspensions (Hastings *et al.*, 2007). Current policy obligates the nuclear industry to deal with legacy nuclear waste issues promptly (of Trade & Industy, 2002). A brief description and relevant history of the situation is subsequently provided for context.

Sellafield Ltd (Cumbria) is the UKs primary high and intermediate level waste facility. The majority of Spent Nuclear Fuel (SNF), originating from the early MAGNOX and Advanced Gas Reactors is stored here. SNF was, and currently is stored in cooling ponds at Sellafield. This method of storage is advantageous in that large volumes of water remove radioactive decay heat from SNF, as well as acting as a suitable radiation barrier. The SNF treatment process involves several years of interim storage, throughout which radioactivity levels continuously decline. Subsequently SNF is removed from the ponds and stripped of metal cladding (protective outer layer). The cladding is deemed intermediate level waste and SNF is reprocessed in the UK. These processes require SNF and its constituents to undergo transport and occupation in various containments, e.g. tanks, pipes, ponds and silos (Gregson *et al.*, 2011). In the first few decades of the nuclear energy business, the need to deal with wastes was generally low on the agenda, thus working practices led to SNF and its constituent wastes being stored in wet conditions for extended durations. Inevitably partial and full erosion of materials, including fuel cladding, resulted. An example of such a case is the Pile Fuel Storage Pond at the Sellafield main site. This is an open air containment constructed in the 1950's which acted as a temporary storage facility for SNF prior to reprocessing. An overhaul of reprocessing in the 70's caused a storage backlog of fuel rods which consequently began corroding and forming a complex radioactive system, comprising stored solid material, sludge from corroded materials and pond-water. Since the pond has been exposed to the elements for over 60 years, its contents are further complicated by the addition of bio-disperse organic materials. Consequently this is a complex, toxic, intermediate level, radioactive waste sludge and suspension which is difficult to

characterise and handle (Jackson *et al.*, 2014). Many of the containments comprising legacy wastes were built several decades ago and are nearing their end of life. Hence it has become an ever increasing priority for the wastes to be characterised, to enable eventual retrieval, processing and storage, so that these facilities may be decommissioned (Hastings *et al.*, 2007). The desire for *in situ* devices arises directly from the radio-toxicology aspect. Current methods involve extensive sampling and sample processing which is hazardous, labour intensive and hence costly. Characterisation of such facilities is highly complex (Gregson *et al.*, 2011). However the ability to perform even rudimentary *in situ* qualitative characterisation of the sludges and suspensions would certainly be beneficial for the monitoring and eventual decommissioning of such a facilities. Therefore the development of novel techniques is essential to enable characterisation, and aid legacy waste clean-up.

In order to establish a research plan going forward, the current status of *in situ* ultrasonic measurement is examined in a literature review in section 1.2, and the underlying acoustic backscatter theory including recent developments is presented in section 1.3. The research objectives are outlined and a research outlook for proceeding chapters is provided in section 1.7.

1.2 Literature Review

The range of options available for dispersion characterisation are reviewed here, with an emphasis placed on acoustic methods.

1.2.1 Non-Acoustic Techniques for Dispersion Characterisation

The typical non-acoustic methods available for dispersion characterisation can be denoted into four categories; optical, electrical, radiation emission and physical sampling methods (Shukla *et al.*, 2007; Williams *et al.*, 1990). The latter approach is a traditional and still a very widely adopted approach for determining concentration and settling kinetics. Samples are extracted from the system and

are typically subjected to gravimetric analysis, sedimentation tests and sedimentation balance measurements for example (De Clercq *et al.*, 2008; Iritani *et al.*, 2009). Although sampling provides physical evidence of constituents and the direct observation of settling kinetics for inference of behaviour, the approach encompasses numerous drawbacks. Primarily, sampling is invasive so a true representation of conditions within an unperturbed system is not possible. Furthermore, the settling kinetics observed in the *ex situ* measurement scenario may not be comparable with kinetics in the system in question. Various real time system related parameters which influence behaviour cannot be accounted for. In addition sampling is labour intensive and thus costly especially in the case of hazardous and inaccessible dispersions. Rapid online monitoring is not an option. And spatial and temporal profiles are not attained with ease (Meral, 2008).

Optical instrumentation incorporating laser transmission or scattering measurements via detectors or cameras are widely utilised. There are various *ex situ* techniques; dynamic light scattering (Goldburg, 1999), optical microscopy (Balastre *et al.*, 2002), particle-image velocimetry techniques (Hardy *et al.*, 2011; Meinhart *et al.*, 1999) and CCD-camera techniques (Hernando *et al.*, 2015; Hubner *et al.*, 2001), as well as *in situ* options; turbidity meters (Finlayson, 1985; Lawler & Brown, 1992), optical backscatter systems (Fugate & Friedrichs, 2002; Lynch *et al.*, 1994) and laser *in situ* scattering tomography (Gartner *et al.*, 2001; Meral, 2008), for characterising parameters such as particle size, concentration, settling and sediment transport in flows. However all optical methods are limited to application in transparent dispersions due to significant light attenuation in concentrated media. Recently *ex situ* dynamic light scattering has been coupled with additional instrumentation and models to enable characterisation of sub-micron dispersions with intermediate concentrations (Xia *et al.*, 2005) and aggregated dispersions (Tanguchi *et al.*, 2010).

There are several variations of electrical impendance tomographic techniques; capacitance (Jaworski & Bolton, 2000), conductivity (Richardson & Holdich, 2001), and resistance (Hosseini *et al.*, 2010) measurement techniques for example, for the characterisation of concentration, velocity distributions and extent of solid-liquid mixing in two-phase flowing suspensions in tanks and pipes. These

employ a multitude of excitation and detection electrodes which measure electrical properties such as capacitance, conductivity and resistance. Such methods offer high resolution temporal and spatial profiles of suspension characteristics (Wang *et al.*, 2005). However their application is limited for a variety of reasons; they operate on a separate transmitter and detector basis so alignment needs to ensured, since they capture data as cross-sections of the dispersion, then it is necessary to insert a number of probes into the dispersion so that a depth profile may be measured, this makes it a rather intrusive and complex technique and limits its employability and increases cost. High level of noise in the measurements leading to misleading images (Bolton *et al.*, 2007).

Radiation emission techniques propagate external radiation sources such as x-rays (Chu *et al.*, 2002) or γ-rays (Kaushal & Tomita, 2007), through a dispersion and measure the attenuated transmitted radiation. The measurements give an indication of concentration densification and can enable monitoring of sedimentation. Although these methods works well in *ex situ* monitoring scenarios, it can be impractical for large scale *in situ* application. Reasons include the introduction of general radiation safety issues, limitations of transmitter and detectors positioning, and Compton scattering and photoelectric absorption issues owing to chemical composition (Chu *et al.*, 2002; Kaushal & Tomita, 2007; Wheeler & Chatterji, 1972).

The common options available for dispersion characterisation encompass various caveats rendering them inapplicable for large scale industrial applications or for vats with restricted accessibility. The primary caveats are associated with concentration limitations and intrusive, complex and costly application. Acoustics however, can potentially surmount such caveats to a practicable extent (Williams *et al.*, 1990). Not only can acoustic waves penetrate further and characterise more concentrated and opaque suspensions than optical scattering techniques (Challis *et al.*, 2005; Temkin, 1998), they also provide a remote non-intrusive method for obtaining high temporal and spatial resolution profiles of suspended concentration and particle size (Downing *et al.*, 1995).

1.2.2 Acoustic Techniques for Dispersion Characterisation

Acoustic techniques involve the emission of an acoustic pulse and measurement of the scattered or transmitted wave. The level of scatter and attenuation of the wave are characteristic of the features of the suspended particles, therefore providing a route to characterise particle size, concentration and settling velocities. Low power diagnostic ultrasound (1-10 MHz) is utilised for this purpose. *Ex situ* devices measuring transmission and reflection have been developed by food science (Challis *et al.*, 2005; Dukhin & Goetz, 2001; McClements, 1991) and colloid groups interesting in characterising concentrated dispersions. The development of *in situ* pulse echo methods have been driven by sedimentologists for sediment transport studies in rivers and coastal zones (Thorne & Hanes, 2002). Diagnostic ultrasonic methods are easy to operate, are non-invasive, non-destructive, are not particularly sensitive to opacity unlike light methods, so dilution is not required. They also provide rapid precise measurement such that non-stationary systems may be studied (Holmes *et al.*, 1993; McClements, 1991). Acoustic mass concentration results have also been found to be superior to counterpart light scattering techniques (Fugate & Friedrichs, 2002; Meral, 2008).

Ex situ instrumentation is based on sound attenuation and velocity measurements via a broadband of frequencies (1-150 MHz). There is only a small gap of a few millimetres between the transmitter and detector in case of highly attenuating dispersions. The measured frequency dependent attenuation coefficient is applied to a scattering model to calculate particle size or concentration, and also monitor phase inversion, particle interaction, and disperse phase adiabatic compressibility in emulsions(Challis *et al.*, 2005; Dukhin & Goetz, 2001; Holmes *et al.*, 1993; McClements, 1991). The so called ultrasonic attenuation spectroscopy has been utilised in a vast range of dispersions, as listed in table 1.1.

There is a range of *in situ* transceiver devices developed for the monitoring of sediment transport. The Acoustic Doppler Current Profiler utilises a single frequency transducer to obtain depth-wise or horizontal sediment velocity profiles (Best *et al.*, 2005; Gartner, 2004). The Acoustic Doppler Velocimeter (ADV)

Table 1.1: List of existing applications for particle sizing via ultrasonic attenuation spectroscopy, from Dukhin & Goetz (2001).

Aggregative stability	Food products
Cement slurries	Latex
Ceramics	Microemulsions
Chemical - mechanical polishing	Mixed disperse systems
Coal slurries	Nanosize particles
Coatings	Non-aqeous systems
Cosmetics	Paints
Environment protection	Photo materials
Floatation, ore enrichment	

measures three-point velocity components at a specific location enabling accurate velocity measurement (Fugate & Friedrichs, 2002; Ha *et al.*, 2009). There are profiling ADV's available. The Ultrasonic Velocity Profiler utilises a small probe and a single frequency to characterise flows, and is well suited to small scale applications (Hunter *et al.*, 2011; Rice *et al.*, 2014). All three devices measure the Doppler shift from reflected waves in flowing suspensions. Alternatively there are Acoustic Backscatter Systems (ABS) which measure backscattered wave amplitude, rather than the frequency Doppler shift. These enable the employment of a multitude of frequencies to obtain large suspension depth profile, and has been demonstrated to exhibit superior resolution to light scattering techniques, with respect to spatial and temporal profiling (Moore *et al.*, 2013a). Due to rapid measurement, they are also suited to monitoring dynamic suspensions, such as settling dispersions. They offer flexibility to be deployed in small scale laboratory studies alongside typical larger scale field applications (Bux *et al.*, 2015). A commercially available ABS comprises transceiving transducers which insonify a dispersion with ultrasonic pulses of monochromatic frequencies in the 0.5-5 MHz range. Usually more than one frequency is used in sequence for profiling. The emitted pulse interacts with mediums such as suspended particles, sludge-supernatant interfaces or walls in its path, and returns characteristic echo responses to the transceiver in the form of backscattered pressure waves. The mechanical impact of the pressure wave excites the piezoelectric crystal in the transducer, and a corresponding

measurement is recorded as root mean square amplitude in volts. Measurements are discretised into distance bins from the transducer since there is a delay in the echo receipt at increasing distances. Due to these features ABS can provide an illustration in some respects of suspension characteristics and process including concentration gradients, sludge and sediment bed positions and depths, and can therefore be used to monitor sedimentation processes (Bux *et al.*, 2015).

Thus far, the ABS has well established application for suspended sediment concentration or particle size measurement, in large (>tens of microns) dilute ($<1\,\mathrm{g\,l^{-1}}$) suspensions of sandy particles in coastal zones and rivers (Rose & Thorne, 2001; Thorne & Hanes, 2002). Since the backscatter intensity and attenuation exhibit a linear relationship with concentration in the corresponding dilute environments (Moore *et al.*, 2013a), it is possible to directly determine concentration from a backscatter measurement profile. The ability to obtain spatial and temporal profiles of dynamic bed-load and suspended load in field applications has been repeatedly demonstrated (Moore *et al.*, 2013a; Rose & Thorne, 2001). Suspension profiling depths of up to 10 m in dilute regimes has also been demonstrated (Moore *et al.*, 2013a). However, as with any single frequency probe, any single transducer it cannot differentiate between changes in concentration and changes in particle size distribution thus the backscatter signal becomes convoluted, since both influence signal attenuation (Libicki *et al.*, 1989; Temkin, 2005). If independent information about particle size distribution is already known, the error in measurement can be reduced (Meral, 2008). Recently, an advance has been made in determining particle size (in a monodisperse size distribution) by undertaking a multiple frequency approach (Moore *et al.*, 2013a).

The standard present ABS characterisation method (Thorne & Hanes, 2002), is not applicable in concentrated dispersions $>2.5\,\mathrm{g\,l^{-1}}$ (Hunter *et al.*, 2012a), or for highly attenuating particles in the colloidal size range (Weser *et al.*, 2014). This is primarily because the models for sound propagation do not take into account multiple scattering in high concentration scenarios. Furthermore, particle specific backscattering and attenuation properties are a prerequisite. However, Hunter *et al.* (2012a) proposed a phenomenological analysis approach to backscatter analysis in order to characterise suspended sediment concentration in regimes $>2.5\,\mathrm{g\,l^{-1}}$. Also Rice *et al.* (2014) derived a method for quantifying particle

specific acoustic properties for arbitrary particles. Likewise, the potential for developing convenient acoustic methods for characterising non-dilute dispersions has taken the interest of a number of research groups (Norisuye, 2016; Weser *et al.*, 2014; Zou *et al.*, 2014).

There are number of techniques for facilitating dispersion analysis and there are some options which enable *in situ*, on-line, remote dispersion process monitoring. The common non-acoustic approaches encompass numerous drawbacks; concentration limits, their intrusive nature, complexity of application, and high associated costs. Therefore, the ability to derive key information on settling via measurement of concentration changes with time, is not easily obtained *in situ* (De Clercq *et al.*, 2008; Iritani *et al.*, 2009). However acoustic techniques overcome many limitations to a practicable extent. Hence there exists a research opportunity to develop practicable instrumentation for online *in situ* characterisation in numerous industrial (small & large scale) suspensions, where operations are conducted in continuous as well as batch processes.

1.3 Acoustic Principles & Models of Waves Propagating in Suspension

1.3.1 Mechanisms

This section outlines the interactions of an acoustic wave propagating in a fluid comprising suspended particles. The contribution of each mechanism towards the extinction of incident wave energy is described.

An acoustic wave is a sinusoidal pressure wave which spreads spherically. It propagates through a medium by causing a series of compressions and expansions which correspond with the wavelength of the emitted frequency. When a compression wave insonifies a suspended particle, the particle scatters and absorbs the sound. Scattering is essentially the redirection of the wave via reflection and refraction. The amplitude of the scattered wave is attenuated relative to the incident wave due to six absorption mechanisms; visco-inertial, thermal, scattering, intrinsic, structural and electrokinetic (Challis *et al.*, 2005; Dukhin & Goetz, 1996; Temkin, 2005).

1. **Visco-inertial:** When insonified, both the particle and fluid move with an acceleration. Since the inertia of the particle is greater, this causes the liquid layers surrounding the particle to slide relative to each other, thus generating a shear wave. The friction of the sliding layers causes acoustic energy losses, which are enhanced with increasing density contrast between the media. The magnitude of shear waves (scattered as a dipole), given by the viscous skin-depth δ_υ equation 1.1(Dukhin & Goetz, 1996), are small scale (few hundred nanometres), so visco-inertial losses are more pronounced for dense colloidal particles <3 µm (Challis *et al.*, 2005).

$$\delta_\upsilon = \sqrt{\frac{2\mu_\upsilon}{\rho\omega}}, \tag{1.1}$$

where μ_υ, ρ and ω are; viscosity, density and angular frequency respectively.

2. **Thermal:** Particles pulsate relative to the surrounding fluid when insonified by a compression wave due to differences in compressibility of the media. Pressure-temperature coupling causes cyclic heating and cooling of the two phases. If the thermal properties of the media are different then they will heat and cool at different rates, thus mediating heat flow between them. Heat-flow is enhanced in less dense, more compressible particles. A monopole thermal wave is scattered, when the heat flow is not in phase with the incident compression wave. The magnitude of thermal waves, given by the thermal skin-depth δ_T equation 1.2 (Dukhin & Goetz, 1996), are small scale (few hundred nanometres), so are more pronounced for colloidal particles with low density contrast with respect to the dispersing medium. Thermal skin-depth is smaller than viscous skin-depth (Challis *et al.*, 2005; Dukhin & Goetz, 2001; Hazlehurst *et al.*, 2014).

$$\delta_T = \sqrt{\frac{2\tau}{\rho C_p \omega}}, \tag{1.2}$$

where τ and C_p are thermal conductivity and specific heat capacity respectively.

3. **Scattering:** Figure 1.1 illustrates how a portion of the incident compression wave is redirected at angles other than 180°, thus attenuating the amplitude of the reflected wave. Compression waves are long in comparison to thermal and viscous waves, therefore scattering related losses are dominant in larger particles, which have a larger scattering cross-section (Carlson & Martinsson, 2002; Challis *et al.*, 2005; Moore *et al.*, 2013a).

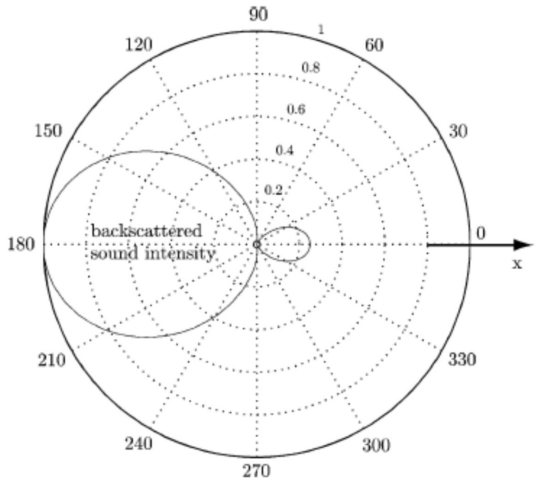

Figure 1.1: Dipole scatter from a rigid sphere when a place wave is incident from the left, from Carlson & Martinsson (2002)

Figure 1.2 from Moore *et al.* (2013a) depicts the attenuation spectra of a monodisperse sediment. The figure illustrates the contribution of viscous and scattering mechanisms towards overall attenuation, with respect to grain size.

4. **Intrinsic:** Acoustic energy also interacts with the particle on a molecular level, as the propagating wave spends some time inside the particles as well as the suspending phase. The associated energy losses are low, but become more significant when overall attenuation is low in dispersions of small particles in low volume fractions (Challis *et al.*, 2005).

5. **Structural:** The ultrasonic wave applies a stress over half a wavelength, which corresponds with tenths of microns on the megahertz scale. This scale

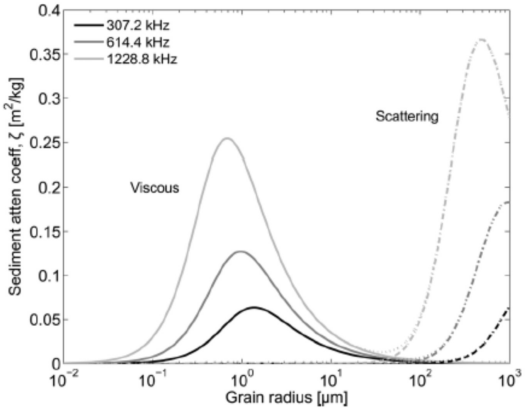

Figure 1.2: Viscous and scattering attenuation coefficients of monodisperse sediments as a function of grain size at three frequencies, from Moore *et al.* (2013a)

corresponds with the structural length scale when particles are networked in some sort of structure, for example in flocs. In this case, the rheological aspects of the dispersion start to influence acoustic wave propagation, causing additional energy losses (Challis *et al.*, 2005).

6. **Electrokinetic:** The relative motion of the particle and fluid causes displacement of the particle's electric double layer. The oscillation of charged particles generates an alternating electric field. So the electrokinetic mechanism is directly linked to the shear waves associated with the viscous mechanism. However the overall contribution to attenuation is negligible (Challis *et al.*, 2005; Dukhin & Goetz, 1996).

Clearly the influence of each of the mechanisms depends mainly on particle size and also density. The scattering behaviour can be characterised with respect to the particle size range, where a is the particle radius, and the insonifying frequency, where k is the wavenumber, as follows;

$$ka = \frac{\omega a}{c} = \frac{2\pi f_r a}{c} = \frac{2\pi a}{\lambda}, \tag{1.3}$$

where f_r is the frequency, ω is the angular frequency, c is the speed of sound in the dispersion, and λ is the unltrasonic wavelength (Shukla *et al.*, 2010). The

Table 1.2: Summary of scattering regimes and corresponding attenuation mechanisms

Rayleigh Scattering	Mie Scattering	Geometric Scattering
$ka<1$	$ka\sim1$	$ka>1$
$\lambda>a$	$\lambda\sim a$	$\lambda<a$
long wavelength limit	intermediate wavelength limit	short wavelength limit
viscous attenuation	scattering attenuation	scattering attenuation

product of the insonifying wavenumber and particle size, enables characterisation of scattering behaviour as depicted in table 1.2.

The most significant absorption mechanisms contributing to the sediment attenuation α_s are visco-inertial α_{vi}, thermal α_{th} and scattering α_{sc}, as pictured in figure 1.3. Overall attenuation is a combination of the attenuation due to the sediment and from the intrinsic absorption in water α_w (the fluid phase); $\alpha = \alpha_s + \alpha_w$. The relationship between attenuation and backscattered wave amplitude A is given by $A = A_0 e^{-\alpha r}$, where A_0 is the amplitude of the incident wave and r is the transducer range. Hence the amplitude of the wave decays exponentially with increasing distance from the transducer. Attenuation also depends linearly on insonifying frequency, hence increases with increasing frequency due to more rapid energy dissipation associated with shorter wavelengths (Shukla *et al.*, 2010). Numerous groups (Hay, 1991; Sung *et al.*, 2008; Thorne *et al.*, 1993; Urick,

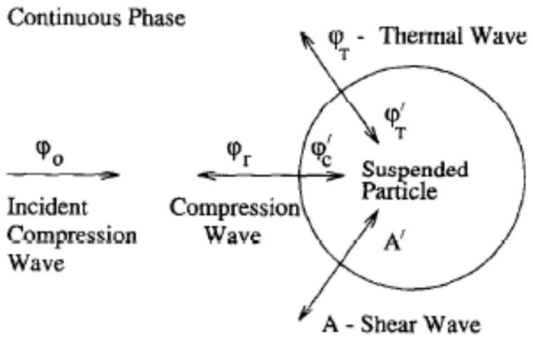

Figure 1.3: Three wave types scattered into and away from a particle, from Tebbutt & Challis (1996)

1948) and (Hunter *et al.*, 2012a) for example, have investigated the dependency of attenuation, on dispersion concentration, in a range of sediments. A linear relationship has been observed between the two parameters over a wide range of concentrations, but it depends very much on the insonifying frequency and the insonified particle size. For example Hay (1991) found that linearity was observed in concentrations up to $5\,\mathrm{g\,l^{-1}}$ via 5 MHz, and up to $25\,\mathrm{g\,l^{-1}}$ via 1 MHz in large sand sediments. Thus linearity held for a much greater range of concentrations in the relatively lower ka region. Shukla *et al.* (2010) also observed this trend in glass bead suspensions. Likewise, various studies conducted at higher ka values report linearity in dilute regimes (Sheng & Hay, 1988; Thorne *et al.*, 1993). Whereas linearity is reported within the Rayleigh scattering limit ($ka<1$) by Greenwood *et al.* (1993); Sung *et al.* (2008); Urick (1948). In a linear case, it is possible to infer dispersion concentration directly from the magnitude of attenuation (Hunter *et al.*, 2012a). Hay (1991) also reported the independence of backscatter intensity from concentration at high volume fractions, where attenuating influences become dominant.

1.3.2 History of Acoustic Scattering Models

A number of models for ultrasonic propagation in suspensions have been developed over the years, to relate sound propagation properties such as velocity and attenuation, with the physical properties of the dispersions such as particle size and concentration (Dukhin & Goetz, 2002). Dukhin & Goetz (2001) state that a model should be valid for a wide range sizes, account for all interaction mechanisms (as in section 1.3.1), and account for multiple scatterers and inter-particle interactions in a range of concentrations. A detailed history of the development of ultrasonic propagation in dispersions is provided by Dukhin & Goetz (2002), and a brief summary of some key developments is provided here.

Brief history from Dukhin & Goetz (2002); the first development dates as far back as Newton (1687) however it was not until much later that Stokes (1845-51) accounted for the contribution of viscous losses and, Kirchoff (1868) accounted for thermal losses with respect to attenuation. The first ultrasonic application to colloids was by Henry, Tyndall and Reynolds (1870-80) (Dukhin

& Goetz, 2002). Rayleigh (1897) and Sewell (1910) provided a theory for viscous attenuation losses in colloids in heterogeneous dispersions. Pulse technique instrumentation was first developed by Pellam & Galt (1946). Subsequently Urick & Ament (1949) presented a model which accounted for viscous losses only and Isakovich (1948) developed a theory for thermal attenuation in colloids. Hence the models thus far only accounted for viscous losses or thermal. Therefore Epstein & Carhart (1953) developed a more comprehensive model which accounted for both attenuating mechanisms in water fog in air, and was later improved by Allegra & Hawley (1972) for attenuation in sound in suspensions and emulsions. The so called combined ECAH theory (1953-72) is a general theory for sound attenuation in dilute colloids and is the most commonly used model. Notably, although it accounts for the two principal attenuating mechanisms, it does not account for all mechanisms. It is only applicable in dilute dispersions and in the long wavelength limit, hence it does not satisfy all requirements of a complete model.

A number of models based on ECAH theory have subsequently been developed in order to account for multiple scatterers in concentrated dispersions; for example, Waterman & Truell (1961), Lloyd & Berry (1967) which does not account for thermal contributions and (Harker & Temple, 1988) coupled phase model for acoustics of concentrates (Hazlehurst *et al.*, 2014). Application of ECAH theory is fairly complex. Essentially attenuation measurements are made via *ex situ* instrumentation utilising a broad band of frequencies to extract an attenuation coefficient. This value alongside numerous particle and fluid physical parameters listed below (from Tebbutt & Challis (1996)), are required to fit the data to the model to extract particle size. Gaunaurd *et al.* (1995) formulated an analytical solution to ECAH.

- Compression wave speed,
- density,
- particle radius,
- shear viscosity of fluid phase,

- shear modulus of solid phase,
- thermal conductivity,
- specific heat capacity,
- attenuation of sound,
- thermal dilatability.

Tebbutt & Challis (1996) compared four models for velocity and attenuation calculation in colloidal suspensions and emulsions; Urick (1948), Urick & Ament (1949), Harker & Temple (1988) and Allegra & Hawley (1972) for varying particle types. It was found that different models fit best with different particles. All models gave a good fit for Titania which has a high density contrast. The Allegra and Hawley model gave better fit for polystyrene (low density and thermal properties contrast), and aqueous iron (large thermal and density contrast) than other models. Although this model is most versatile, it is also the most complex to implement and requires pre-requisite knowledge of numerous parameters. Temkin (1998) also presented a comprehensive theory for particles at dilute concentrations.

Clearly a comprehensive model that takes account of all mechanisms does not exist despite many years of effort. (Dukhin & Goetz, 1996) stated that multiple scatterer theory is far from done. Even to date as seen in recent publications, multiple scatterer theory based on the ECAH theory is very much in development (Hazlehurst *et al.*, 2014). Indeed multiple scattering from aggregated and flocculated particles is certainly not accounted for.

Since the 1990s there has been increasing interest from sedimentologists interested in sediment transport studies via *in situ* pulse echo instrumentation. Thus a model was developed by Thorne & Hanes (2002) and Thorne *et al.* (2011) based on Hay (1991), Atkinson & Kytömaa (1992) and Richards *et al.* (1996) for the characterisation of dilute sandy sediment dispersions. This model has since been applied by Moore *et al.* (2013a), as well as other groups; Admiraal & Garcia (2000), Hunter *et al.* (2012a) and others Rice *et al.* (2014). The model is typically applied for dense and large particles, but because it is valid for dilute

suspensions, it does not satisfy Dukhin & Goetz (2001) third specification; for a model to be valid at at all concentrations. However, this model is of interest for the purposes of this research because it considers an *in situ* pulse echo for characterisation unlike the previously discussed models which have typically been utilised with *ex situ* instrumentation. Similar models have also been developed by Carlson & Martinsson (2002); Furlan *et al.* (2012), which incorporate numerous particle parameters. More recently published approaches include; Weser *et al.* (2014) whom correlate the statistical features of the backscattered amplitude via a transceiving transducer, with concentration, Zou *et al.* (2014) whom utilise an ultrasound scanner for image measurement of concentration distributions, and Norisuye (2016) whom utilise a dynamic ultrasound scattering principle in a co-axial geometry to detect the velocity flux of nanometre sized particles in Brownian motion. The Thorne & Hanes (2002) model is utilised going forward, since it incorporates minimal particle parameters and is simpler in application than other models (Carlson & Martinsson, 2002; Furlan *et al.*, 2012).

1.4 Acoustic Backscatter Theory

The components of a transducer are illustrated in figure 1.4A. The active element which is a piezoelectric crystal is the key feature. Essentially an electric potential is applied for a duration of 10 µs, causing mechanical vibration of the crystal and resulting in the emission of a monochromatic ultrasonic pressure wave, which insonifies a volume of dispersion as illustrated in figure 1.4B. The pressure wave undergoes a series of maxima and minima until it converges to a focus point N close to the transducer and subsequently diverges at constant angle γ_0, spreading spherically whilst receding in pressure amplitude at a constant rate. The near-field and far-field are the corresponding regions either side of the focus point. The described beam characteristics are illustrated in figure 1.4C. A portion of the pressure wave incident on a suspended particle, reflects in the direction of the transducer. The pressure backscattered to the transceiving transducer excites the active element generating a voltage. The root-mean-square voltage (V_{RMS}) is recorded. Since the amplitude of the backscattered pressure wave is highly

dependent on the scattering medium, this provides a means of characterising a particulate dispersion.

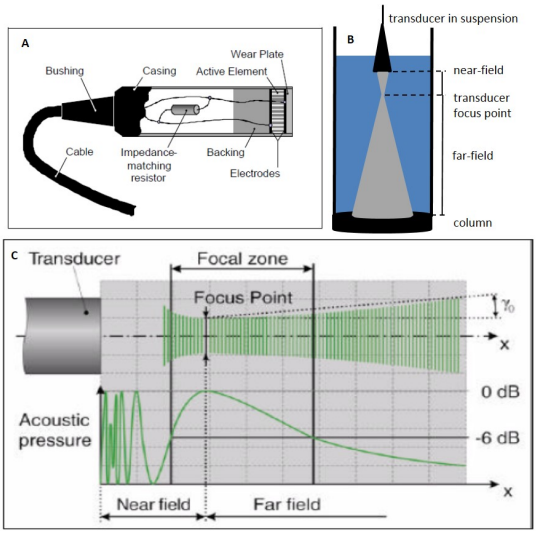

Figure 1.4: (a) transducer components, (b) region of insonification and (c) acoustic wave, from MET-FLOW (2002)

1.4.1 Thorne Model

The acoustic backscattering model for particles in suspension, as described by Thorne & Hanes (2002) and (Thorne *et al.*, 2011), was developed with a view to enable characterisation of particle size or concentration in dilute sandy sediment dispersions. Its application has been verified in field sedimentology studies by various researchers (Meral, 2008; Moore *et al.*, 2013b; Topping *et al.*, 2007). It is also simpler in application than other models (Carlson & Martinsson, 2002; Furlan *et al.*, 2012), because the measured backscatter response is only a function of particle size, concentration and the quantified backscattering and overall attenuation properties of the particle. The attenuation is not split into its various components, e.g. visco-inertial, thermal and scattering for example. Particle shape is not accounted for, and neither is multiple scattering for concentrated dispersions. Therefore the corresponding equations are relatively simple, compared with other models which incorporate many other particle parameters. Hence, the

Thorne & Hanes (2002) model was selected for research purposes going forward, with respect to extending ABS application to engineering scenarios which typically incorporate small grain sizes and a broad range of dispersion concentration regimes.

The measured V_{RMS} varies with distance r from the transducer as follows;

$$V_{RMS} = \frac{K_t K_s M^{\frac{1}{2}}}{r\psi} e^{-2r\alpha}, \tag{1.4}$$

where K_t is an independent system constant, K_s is the sediment specific backscattering constant, M is the particle mass concentration, $\alpha = \alpha w + \alpha s$ is the total attenuation contribution from water and the sediment respectively, and ψ is a correction factor to account for non-linearity of the signal in the near-field region. Each component can be determined through the following equations;

$$\psi = \frac{1 + 1.35z + (2.5z)^{3.2}}{1.35z + (2.5z)^{3.2}}, \tag{1.5}$$

from Downing *et al.* (1995) where $z = \frac{r}{r_n}$ and $r_n = \frac{\pi a_t^2}{\lambda}$, where a_t is the transducer active element radius and λ is the ultrasonic wavelength. ψ tends to unity in the far-field. The particle's scattering properties are determined by K_s as follows;

$$K_s = \frac{\langle f \rangle}{\sqrt{\langle a \rangle \rho}}, \tag{1.6}$$

where f is the form function and ρ is the particle density. The form function f quantifies the backscattering characteristics of the particle. It is solved via Bessel and Hankel functions, however empirical heuristic equations have been developed for relative analytical ease. Although these heuristic fits were developed through exhaustive experimentation. Figure 1.5A illustrates the complex form of the heuristic high order polynomial expression with respect to ka, otherwise referred to as x here. The form function is described in more detail in chapter 2 section 2.1. Heuristic expressions for f have been defined for spherical glass particles and irregularly shaped sandy sediment dispersions. For the latter it is expressed as;

$$f = \frac{x^2(1 - 0.35e^{-((x-1.5)/0.7)^2)})(1 + 0.5e^{-((x-1.8)/2.2)^2)})}{1 + 0.9x^2}, \tag{1.7}$$

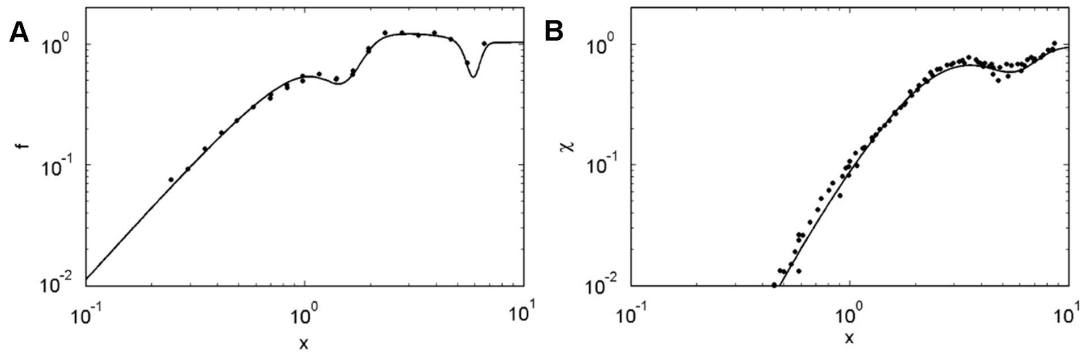

Figure 1.5: (a) Form function, and (b) total normalised scattering cross-section with respect to $x = ka$, for irregularly shaped sandy sediments, from Betteridge *et al.* (2008).

$$\langle f \rangle = \left(\frac{\langle a \rangle \langle a^2 f^2 \rangle}{\langle a^3 \rangle} \right)^{\frac{1}{2}}, \tag{1.8}$$

where $x = ka$, described earlier section 1.3.1, from Betteridge *et al.* (2008). f is proportional to $(ka)^2$ in the long wavelength limit (Rayleigh scattering regime) and tends to a constant value in the short wavelength limit (at large ka). $\langle\rangle$ represents the average value over the particle size distribution. Going forward, in the case of a narrow monodisperse distribution, the median size of the particle size distribution is selected. Hence the particle radius a is determined from the median diameter d_{50} where $a = \frac{d_{50}}{2}$.

The attenuation contribution of water at zero salinity from Ainslie & McColm (1998) at temperature T in °Cfor a given ultrasonic frequency f_{r} is given by;

$$\alpha_w = 0.05641 f_r^2 e^{-(\frac{T}{27})}. \tag{1.9}$$

The attenuation due to the sediment is quantified by;

$$\alpha_s = \frac{1}{r} \int_0^r \xi(r) M(r) dr, \tag{1.10}$$

where the sediment attenuation coefficient ξ is given by;

$$\xi = \frac{3\langle \chi \rangle}{4\langle a \rangle \rho}. \tag{1.11}$$

The total normalised scattering cross-section χ quantifies the particles attenuating properties due to scattering and absorption losses. This parameter is also derived by a high order polynomial heuristic expression, for relative analytical ease. The form of the expression for χ is illustrated in figure 1.5, an its derivation is discussed in detail in chapter 2 section 2.1 for spherical glass and sandy sediment dispersions. For the latter it is expressed as;

$$\chi = \frac{0.29x^4}{0.95 + 1.28x^2 + 0.25x^4}, \tag{1.12}$$

$$\langle \chi \rangle = \frac{\langle a \rangle \langle a^2 \chi \rangle}{\langle a^3 \rangle}, \tag{1.13}$$

χ is proportional to $(ka)^4$ in the long wavelength limit and tends to a constant value in the short wavelength limit. The series of equations highlight the particle size dependency of K_s and α_s. The Thorne model assumes that particle size is uniform throughout the dispersion because size differences manifest in the backscattered intensity. In the case of a distribution, it is accounted for in equations 1.8 and 1.13. As long as K_s, α and K_t are known, equation 1.4 can be inverted to yield concentration from measured voltage;

$$M = \left\{ \frac{V_{RMS}\psi r}{K_t K_s} \right\}^2 \mathrm{e}^{4r\alpha}. \tag{1.14}$$

Prior knowledge of M and $\langle a \rangle$ is required in order to determine K_s and α, however M and $\langle a \rangle$ are the parameters which require characterisation. Therefore in the case where voltage data from a single frequency are available, an implicit iterative approach can be taken. If α_s is assumed to negligible, approximately zero as in a dilute dispersion scenario $\xi M \ll 1$, then $\alpha = \alpha_w + 0$. If $\langle a \rangle$ can assumed to be constant throughout the transducer range, then K_s can be calculated. Thus a value of M_0 can be determined for the dilute case. However if it is not reasonable to assume that $\alpha_s \sim 0$, then an iterative approach can be taken where $M_1 = M_0 e^{4r\alpha}$ and the process is repeated until the values of M_n and M_{n+1} converge (Thorne & Hanes, 2002).

The implicit iterative inversion model is only valid in very dilute dispersions $<0.1\,\mathrm{g\,l^{-1}}$ where acoustic attenuation is negligible (Rose & Thorne, 2001). When

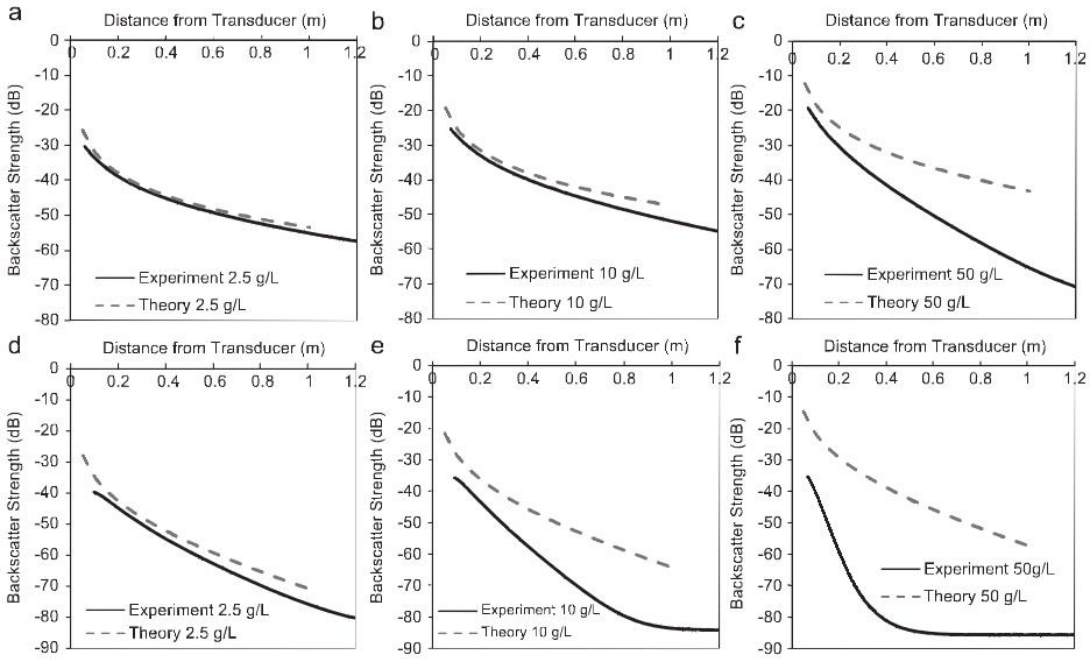

Figure 1.6: Comparison between experimental acoustic echo responses and threshold predictions for spherical glass dispersions at 2.5, 10 and $50\,\mathrm{g\,l^{-1}}$, via 2 MHz A-C, and 5 MHz D-F, from Hunter *et al.* (2012a).

concentration is increased the Thorne inversion model breaks down because it does not take into account enhanced attenuation due to increased inter-particle scattering interactions. Hunter *et al.* (2012a) found the model to overestimate concentration above $2.5\,\mathrm{g\,l^{-1}}$ in comparable glass particle dispersions, depicted in figure 1.6. Furthermore even in the dilute case, the iterative implicit inversion requires pre-existing knowledge or estimations of sediment specific properties. Any errors in these parameters manifest in the concentration estimations. From an iterative perspective, errors in concentration estimates become increasingly erroneous over the range of propagation (Rice *et al.*, 2014; Thorne & Hanes, 2002; Thorne *et al.*, 2011).

1.4.2 Phenomenological Characterisation Approach

All inversion methods can only be applied for the characterisation of concentration or particle size in sandy sediment or spherical glass particle dispersions, since the form function and total scattering cross-section equations have only been defined for these particular sediments (refer to chapter 2 section 2.1 for further details). This leads onto a discussion of a phenomenological approach proposed by (Hunter *et al.*, 2012a), as a means of providing an alternative route for the characterisation of concentration without *a priori* knowledge of sediment specific properties, and in the high concentration regimes where the inversion approach is invalid.

The measured voltage is typically expressed as backscattered intensity in decibels as follows; $20 \log V_{RMS}$. Equation 1.4 expressed in decibels gives;

$$V_{RMS}[dB] = 20 \log \frac{K_t K_s M^{\frac{1}{2}}}{r} - 40 \log (e) r \alpha. \tag{1.15}$$

Equation 1.15 indicates that the dispersions scattering properties incorporate a logarithmic decay in backscatter intensity with respect to r, and the attenuating contribution incorporates a linear decay. The influences of these components are more prominent in backscatter profiles at larger values of r. This result is key because it indicates that when the attenuating contribution in the signal is high, i.e. when the decay in the decibel backscatter profile is linear with respect to range, then the scattering component in equation 1.15 can be ignored. In which case the attenuation of the profile can be directly quantified by the linear profile gradient. Hunter *et al.* (2012a) found that in high concentration regimes, attenuation varied linearly with concentration (Hunter *et al.*, 2012a). This observation is significant because it provides a route for characterising concentrated dispersions where the Thorne implicit inversion model is invalid, as seen in figure 1.6. Since attenuation is proportional to a and backscatter intensity is proportional to the volume of the particle a^3, concentration estimations based on measured attenuation are less sensitive to grain size and are therefore more robust in small particle dispersions, compared with estimates from backscatter intensity (Moore *et al.*, 2013a).

Since knowledge of sediment specific acoustic properties is not required for characterisation via the phenomenological approach, Bux *et al.* (2015) exploited

this method to characterise an arbitrary mineral dispersion. Interestingly a measurable backscatter intensity was observed in the case of colloidal Titania particles. Since the sediment is highly attenuating due to visco-inertial influences, the corresponding decay gradient of the backscatter profiles depicted in figure 1.7A, were highly linear with respect to transducer range, inferring linear attenuation and indicating dominance over the scattering component in equation 1.15. Resultantly a direct linear relationship between concentration and attenuation was extracted, as seen in figure 1.7B for each frequency. Due to the high linearity,

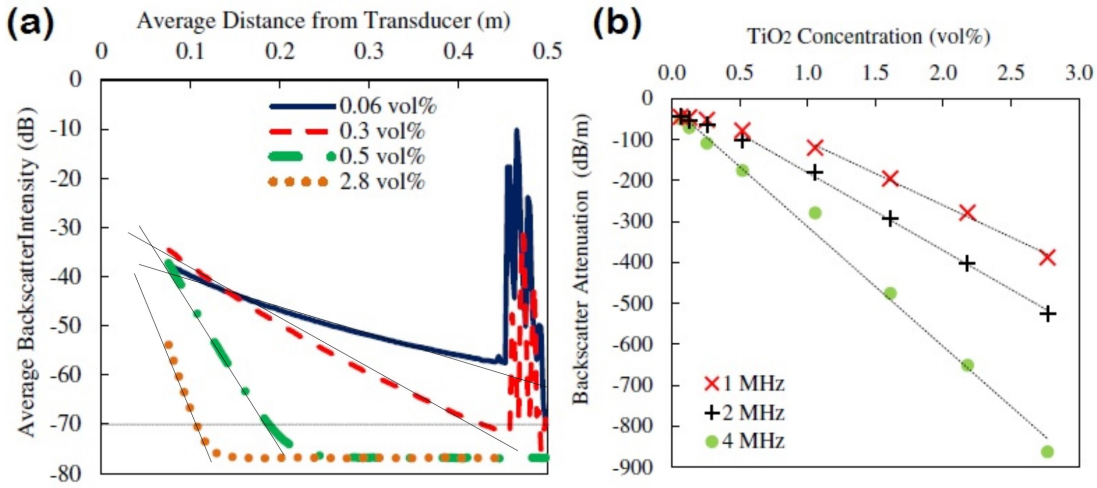

Figure 1.7: (a) 2 MHz backscatter profiles for Titania dispersions at four concentrations, and (b) attenuation-concentration relationship for Titania at three frequencies, from (Bux *et al.*, 2015).

this relationship was directly utilised to characterise concentration changes from attenuation of measured backscatter profiles in a settling Titania dispersion. The ABS tracked the delineation of a hindered settling front down the column, the formation of a sediment bed at the column base, as well as characterising the evolution of a concentration gradient within the settling dispersion due to particle size segregation in the polydisperse system. The ABS coupled with the phenomenological technique proved to be a very powerful characterisation tool for the understanding of intricate settling kinetics, which are not easily obtained *in*

situ (De Clercq *et al.*, 2008; Iritani *et al.*, 2009). It also proved to be superior to an *ex situ* light scattering counterpart instrument. Hence this technique not only provides a route to characterise sediments other than sands or spherical glass, but also dispersions in high concentration regimes $>2.5\,\mathrm{g\,l^{-1}}$ (Bux *et al.*, 2015; Hunter *et al.*, 2012a,b), which is key to exploiting ABS application further afield.

1.4.3 The Rice Method

Hunter's (Hunter *et al.*, 2012a) phenomenological technique is most suited for the characterisation of highly attenuating dispersion systems in which the attenuation-concentration relationship is highly linear (Bux *et al.*, 2015; Hunter *et al.*, 2012b). When the scattering component in equation 1.15 becomes significant, the backscatter profiles in decibels become less linear with respect to range. Therefore quantification of attenuation via direct linear or tangential measurement of the gradient becomes more erroneous. This leads to a discussion of the Rice method which is a recent novel approach for quantifying both the attenuating and backscattering properties of arbitrary sediments.

Dividing equation 1.4 by $r\psi$ and taking the natural logarithm yields;

$$\ln Vr\psi = \ln K_t K_s + \frac{1}{2}\ln M - 2r(\alpha_w + \alpha_s).$$

Substituting;

$$G = \ln(Vr\psi), \tag{1.16}$$

$\alpha_s = \xi M$ for a homogeneously dispersed sediment with respect to concentration and particle size, and taking the derivative with respect to r yields;

$$\frac{dG}{dr} = -2(\alpha_w + \xi M). \tag{1.17}$$

Equation 1.17 indicates that G varies linearly with respect to M. Therefore taking the derivative with respect to M and rearranging yields an equation for determining the sediment attenuation constant;

$$\xi = -\frac{1}{2}\frac{\frac{dG}{dr}}{dM}. \tag{1.18}$$

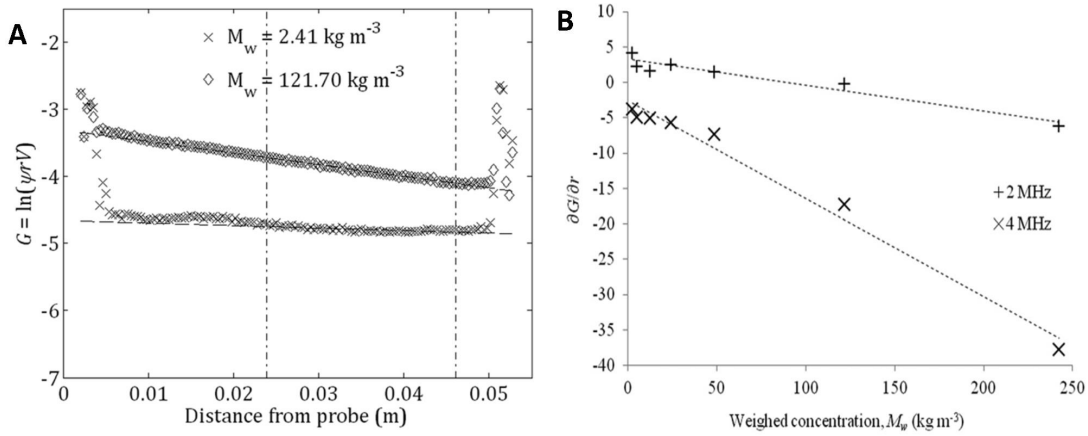

Figure 1.8: (a) G function with respect to transducer range for x 2 concentrations of 44 µm glass bead dispersions via 4 MHz, and (b) corresponding relationship between $\frac{dG}{dr}$ and concentration, from Rice *et al.* (2014).

This linear relationship is depicted in figure 1.8 from Rice *et al.* (2014), where A depicts the G function profiles of glass bead dispersions at two concentrations, with respect to range, and B, the corresponding $\frac{dG}{dr}$ relationship with respect to concentration. Importantly, due to this linear correlation, the problem of non-linearity between direct attenuation of the backscatter profiles and concentration in less attenuating particle dispersions, is overcome. Therefore, the Rice G function approach, provides a relatively robust relationship from which concentration may be qualitatively characterised, compared with that demonstrated by Hunter *et al.* (2012a) and Bux *et al.* (2015). Note, there are unexpected positive values of $\frac{dG}{dr}$ in the latter figure at low concentrations. The dimensions of the corresponding experimental pipe are small (10 cm), and the data range within the far-field region was limited. Since attenuation becomes negligible in dilute concentrations, it is possible that the positive values arise from increases in backscatter intensity from side reflections in the scattering dominant concentration regimes.

Equation 1.18 provides a novel and direct route to determining ξ experimentally, which does not rely on *a priori* knowledge of the sediment's total normalised scattering cross-section χ, which has only been derived for spherical glass and sandy sediments. The extent of data and intensive analysis required to estab-

lish χ for a sediment is highlighted later in chapter 2 section 2.1. Hence Rice's (Rice *et al.*, 2014) derivation is an important break through, because it is now possible to determine the sediment attenuation constant for any arbitrary particulate dispersion without the need for exhaustive experimentation, as long as the dispersions satisfy the condition of homogeneity.

Furthermore once ξ has been determined, equation 1.4 can be rearranged to yield the backscattering constant for any arbitrary particle without *a priori* knowledge of the sediment specific form function f, as follows;

$$K_s = \frac{Vr\psi}{K_t} M^{\frac{1}{2}} e^{-2r(\alpha_w + \xi M)}. \tag{1.19}$$

This is a powerful approach in going forward with developing ABS capability in arbitrary particle suspensions because it is a more robust than (Bux *et al.*, 2015; Hunter *et al.*, 2012a) empirical methods especially in the case where attenuation is not linear. It also enables the quantification of both the backscattering and attenuating properties of arbitrary sediments with relative ease. Thus far the Rice method has only been demonstrated in dispersions comprising large spherical glass particles (40-80 µm diameter) and large jagged plastic particles (460-700 µm diameter). This work was conducted in multiphase pipe flows in which only 5 cm depth profiling was possible (Rice *et al.*, 2014, 2015a,b). Thus much further work is still required for validation of the method, mainly verification in a range of arbitrary dispersion types and on much larger depth scales than pipe-flows.

1.5 Emulsion & Latex Acoustics

The Thorne model has previously been applied in dispersions and suspensions comprising dense particles. Since the governing mechanisms of soft (low density) particle scatter differ, acoustic backscatter of such systems would also be influenced as such. Therefore some attention is given to soft particle scatter here.

The scattering of low density soft particles has been investigated by various groups, mainly McClements (1991) in food science, and (Holmes *et al.*, 1993) and (Tebbutt & Challis, 1996) in engineering. Organic emulsions and Latex particles are common soft particles which have been characterised via small scale *ex*

situ instrumentation discussed in section 1.3.1. Excess attenuation via thermal losses is the primary mechanism in soft particles (refer to section 1.3.1). The basis of ECAH theory assumes that the distance between particles is greater than the insonifying wavelength so there are no thermal interactions between particles. But as concentration is increased, the inter-particle distance is reduced and becomes comparable with the thermal wavelength (refer back to equation 1.2), so thermal layers can overlap and mediate heat flux between particles. This reduces the temperature gradient around any given particle in which case overall heat flux and the corresponding thermal attenuation is lowered. This effect is enhanced for lower insonifying frequencies which have correspondingly longer wavelengths which improve overlapping (Challis *et al.*, 2005; McClements, 1991). Furthermore, this overlapping effect is also prominently observed for small particle radii, the size range for which thermoacoustic scattering is primarily observed. Hazlehurst *et al.* (2014) reports that thermal overlapping fields are larger when particles are in close proximity and non-touching, rather than touching due to particle resonances, see figure 1.9. Another point to consider is that when characterising emulsion droplets, their shape may deviate from sphericity in highly concentrated systems where they are closely packed (McClements, 1991). Shape would certainly implicate the backscattering intensity of a dispersion (Moore *et al.*, 2013a).

1.6 Flocculated Suspension Acoustics

Flocculated suspensions are abundant in nature and industry, thus there is increasing interest in understanding their backscattering properties such that dispersions comprising such particulate structures may be characterisedAustin & Challis (1998); Hazlehurst *et al.* (2014). The scattering of such structures is a complex problem since considerations for the types of particles generating the flocs, as well as the floc structure itself, are required. The size of a floc depends on droplet size, concentration, strength of colloidal interactions and aggregation kinetics, and it is possible that not all droplets/particles will be flocculated (McClements *et al.*, 1998). A number of groups have and presently continue to investigate this problem. Initially the earlier scattering research conducted on soft

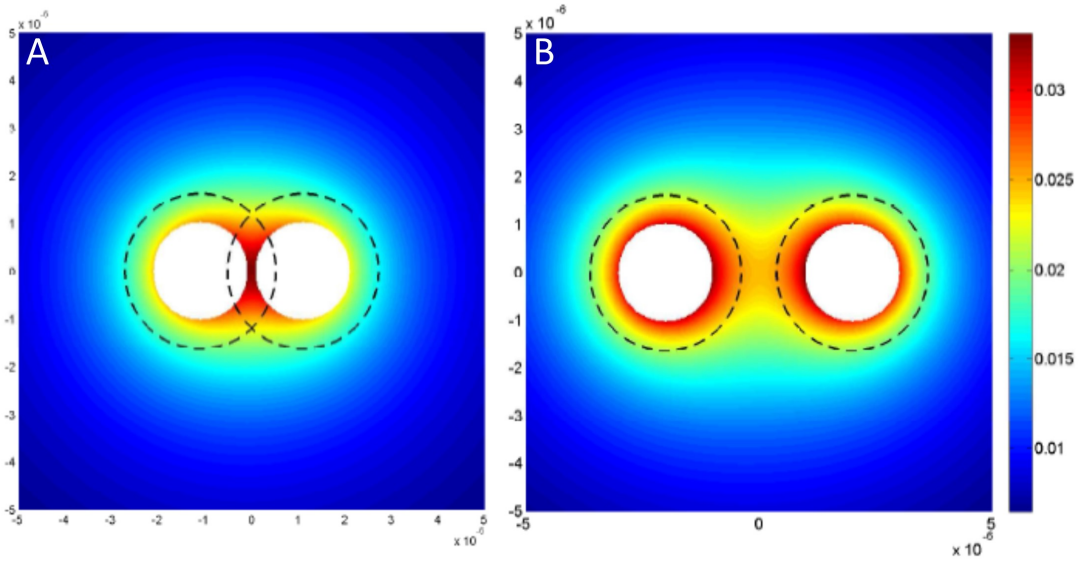

Figure 1.9: Thermal fields of 1 µm particles when (a) touching (distance=2.2a), and (b) in close proximity (distance=6a), from Hazlehurst *et al.* (2014)

flocs in ultrasonic spectroscopy is discussed, followed by the recent investigations by the Thorne group and Hunter *et al.* (2012b) with respect to flocs comprising rigid particles.

Austin & Challis (1998) investigated the effects of flocs on ultrasound in dilute kaolin slurries via *ex situ* ultrasonic spectroscopy. They reported that attenuation and velocity are dependent on the density and size distribution of the floc. An increase in attenuation and velocity were observed in volume fractions above 0.05 vol%, and a reduction below this concentration. McClements *et al.* (1998); McClements (1994) investigated the scattering properties of flocculated emulsion droplets via *ex situ* ultrasonic spectroscopy also, and reported that attenuation depends on the individual droplets as well as the characteristics of the flocs. At low frequency, a reduction in the attenuation coefficient ($\mathrm{dB\,m^{-1}\,MHz^{-1}}$) was observed with increasing floc size due to a reduction in thermal losses associated with enhanced overlapping of thermal layers between droplets within the flocs. Thus the packing of the droplets was key. As packing becomes more open with droplets further apart, attenuation was enhanced due to a reduction in thermal

layer overlap. McClements *et al.* (1998) developed a theory to relate ultrasonic properties of the floc emulsions to the flocs themselves. It is based on ECAH theory and assumes the flocs act as a medium comprising effective properties determined by the size and volume fraction of the individual droplets within the flocs. The theory predicts that the attenuation spectra of emulsions depends on the size of the droplets, the size of the flocs, the packing of the droplets within the flocs and the fraction of droplets which are flocculated. So it may be a useful tool for monitoring flocculation process. However it does not take into account internal packing of flocs, polydispersity of the droplets making up the flocs, polydispersity of the floc size, non-specificity, uniformity of droplets distributed in flocs (flocs usually have fractal structures), the influence of droplet-droplet interactions, and of the visco-inertial losses in flocs.

The Thorne group have also been recently investigating the backscattering of flocs comprising dense particles for incorporation into the Thorne model for backscattering. MacDonald *et al.* (2013); Thorne *et al.* (2014); Vincent & MacDonald (2015) studied large flocs (size) of aggregated kaolin particles. Initially, MacDonald *et al.* (2013) and Thorne *et al.* (2014) proposed that scattering would transition from an elastic sphere model to a fluid sphere model as flocs become more porous filling the interstices with fluid. Vincent & MacDonald (2015) characterised a floc size of a suspension of known concentration. Interestingly the resulting size was much smaller than the actual floc size and corresponded with the size of the aggregated particles making up the floc, therefore they propose that the backscattered signal was dominated by the scattering of the individual aggregates rather than the flocs. If this is the case, the Thorne model would require incorporation of viscous-attenuation losses which is currently ignored because it deals with dilute regimes. Vincent & MacDonald (2015) also state that it is not known how well the heuristic expressions describe the form function and total normalised scattering cross-section of sediments in the low ka region, since measurements in the Rayleigh regime are lacking in the literature. Thorne *et al.* (2014); Vincent & MacDonald (2015) proceeded to categorise flocs into $\frac{1}{4}\phi$ sieve fractions for the Thorne inversion method. However this did not take into account the changes in floc porosities and associated fractal dimensions.

Hunter *et al.* (2012b) proceeded to investigate a flocculated dispersion of glass beads via the empirical method (Hunter *et al.*, 2012a). The general backscatter profiles were highly attenuated and directly linear in comparison to comparable non-flocculated dispersions, due to enhanced inter-particle scattering (Hunter *et al.*, 2012a). Thus it was possible to apply the phenomenological technique in order to characterise suspension concentration.

In summary, in the soft particle case, the structure of the flocs is a major contributor to the overall scattering along with the particle characteristics. However in the dense particle case, it is thought that the visco-inertial effects of the aggregated particles making up flocs is significant. There are a number of overall structural and particle specific characteristics which influence the backscatter of flocculated suspensions. This is clearly a complex problem, the understanding of which is far from complete with respect to incorporation in theoretical models.

1.7 Research Outlook

It is clear that there is great potential for suspended sediment concentration measurement via ultrasonic techniques, in non-dilute dispersions for arbitrary particles. *Ex situ* instrumentation has already been developed for this purpose, but it is very complex in its application because the associated theory requires *a priori* knowledge of an extensive range of parameters. *In situ* techniques have not been developed for this purpose either, due to the complexity of incorporating multiple scatterers in the theoretical models (Rice *et al.*, 2015a). Hunter *et al.* (2012a) provides a phenomenological analysis approach for scenarios where the theoretical inversion models are invalid. Importantly, the Rice method provides a robust semi-empirical method for direct calculation of sediment specific attenuation and backscattering properties for arbitrary particles (Rice *et al.*, 2014). This provides an alternative route for determining concentration phenomenologically because it overcomes any non-linearity between attenuation and concentration. Initial work on the development of this technique was conducted in large particle (>100 µm) glass beads and jagged plastic particle slurries in very small scale (<10 cm) pipe-flows. This method has not yet been verified in larger scale sus-

pension systems, smaller sediment sizes, soft organic sediments, or flocculated sediments. Therein lie numerous research opportunities.

The Rice method (Rice *et al.*, 2014) only quantifies the system constant $K_s K_t$. It does not specify a calibration method in order to determine the transducer constant K_t independently, such that it may be decoupled to provide a sediment specific backscattering constant K_s for arbitrary particles. Hence a robust calibration technique is required.

The influences of flocs on ultrasonic propagation are not yet well understood. For soft particles it is thought that the overall floc structure is significantly influential, as well as the properties of the constituent particles. For dense particles it is proposed that the contribution from constituent particles is predominant. This area is of great interest and requires further investigation.

It is not yet known how well the heuristic equations describe the form function and total normalised scattering cross-section in the low ka Rayleigh scattering regime. There is a lack of data in the literature in that region, since small highly attenuating particles are not characterised via the Thorne inversion model (Thorne & Hanes, 2002). However, there is currently great interest in this scattering regime, specifically for developing the capability to characterise small and colloidal attenuating particles, often encountered in industry.

Evidently, there are numerous knowledge gaps which currently prevent evolution of ABS deployment, beyond traditional dilute sedimentology applications, to a wider range of dispersion systems. Therefore, the proceeding research outlook, is geared towards developing online *in situ* monitoring and characterisation capabilities, for concentrated dispersions comprising arbitrary particle types.

- **Chapter2** outlines a calibration procedure which requires spherical glass bead dispersions. These particle systems are used to verify the Rice method (Rice *et al.*, 2014) for quantifying attenuation constants, and also the backscattering constants for the first time, in relatively larger scale laboratory suspensions.

- **Chapter3** investigates routes to characterise suspensions in a very large scale industrial setting. Specifically the Rice method (Rice *et al.*, 2014)

is used to quantify the attenuation constants, and the backscattering constants for the first time, for inorganic mineral dispersions. It is also utilised in a laboratory calibration of the mineral to establish its reference relationship between measured $\frac{dG}{dr}$ and concentration (see section 1.4.3). The relationship is then exploited for the phenomenological characterisation of concentration in a dynamic dispersion, within an industrial tank which utilises impinging jet ballasts to mobilise settled sediment. Here, this characterisation approach is verified in a large scale industrial setting, and key information on the dynamics of the investigated dispersion are elucidated, such that it enables modelling and optimisation of a complex tank dispersion operation.

- **Chapter4** describes the novel manufacture of soft monodisperse Latex particle dispersions on a litre scale. The influences of aggregation are investigated with respect to ultrasound propagation. The differences in insonified emulsions, corresponding Latex dispersions and aggregated Latex dispersions are directly compared. The Rice method (Rice *et al.*, 2014) is also utilised to quantify sediment and attenuation properties of soft particles.

- **Chapter5** directly compares the acoustic properties of each of the studied particles in the preceding chapters, with respect to density contrast. Information on the nature of the form function and total normalised scattering cross-section is provided in the very low ka scattering regime. A brief concluding summary with a view to further research is also provided.

Chapter 2

Methodology, Calibration & Determining Acoustic Constants

Chapter 2 initially introduces the general methodical approach taken towards experimentation and data analysis throughout this report. Subsequently, novel protocols for transducer calibration, and the derivation of sediment acoustic constants are described. The recently published Rice method (Rice *et al.*, 2014) was validated in a large scale suspension system. This yielded the sediment attenuation constants ξ, for spherical glass particle dispersions. Importantly, the Rice method facilitated quantification of ξ via a direct measurement approach, rather than relying on the fitting of data with a high order heuristic polynomial equation, as in the Thorne model (Thorne & Hanes, 2002). Then, a simple robust calibration protocol for any acoustic backscattering system was established, to determine the transducer constants K_t for all probes. The principles of the calibration were analogous to those published by Thorne & Hanes (2002) and Betteridge *et al.* (2008), however some important variations were made in the execution, which significantly improved data quality, and also markedly reduced the calibration timescale. Primarily, this enabled decoupling of K_t, from the system constant $K_t K_s$, which was not previously possible via the Rice method (Rice *et al.*, 2014). Thus, facilitating the novel assessment of K_s, the sediment backscattering constants.

2.1 Introduction

This discussion commences with an account of the underlying principles for calibrating ABS transducers. The root-mean-square voltage response introduced in equation 1.4, can be rearranged in terms of the transducer constant as follows,

$$\mathrm{K}_t = \frac{V_{RMS}\psi r}{K_s M^{1/2}} \mathrm{e}^{2r\alpha}. \tag{2.1}$$

The backscattering constant K_s, and sediment attenuation coefficient α_s, can be determined according to the Thorne model (Thorne & Hanes, 2002)from previously introduced equations; 1.6 and 1.10, as discussed in chapter 1 section 1.4. The remaining parameter K_t is extracted from a system calibration. K_t is an independent, transducer specific component which accounts for the acoustic beam and electronic response properties of the transducer within an ABS system. One approach to determine K_t is to measure the acoustic and electronic properties of the transducer directly. These include the acoustic beam patterns, receiving sensitivity and source level pressure. Also the electronic signal transmission and receiving levels, the form of time varying signal gain if any is applied and digitisation of the measured signal (Thorne & Hanes, 2002; Thorne & Hardcastle, 1997; Thorne *et al.*, 1993). This is a complex time-consuming approach which requires specialist equipment. A simpler and more accessible method involves backscatter measurement of dispersions of known scatterers, which are homogeneous with respect to particle size and concentration. Since the backscatter measurement inherently incorporates both the acoustic and electronic components of the signal, K_t can be extracted via the rearrangement of equation 1.4. See rearranged equation 2.1 (Betteridge *et al.*, 2008; Thorne & Hanes, 2002);

It is essential that the interaction of sound is well understood and established for the particle type that is selected for calibration purposes, otherwise K_s cannot be accurately determined and thus decoupled from the measurement. In that case, at best, one can determine $K_t K_s$, the system constant (Rice *et al.*, 2014; Thorne & Hanes, 2002). The scattering properties of spheres are well investigated and documented, therefore their scattering properties can be decoupled from the system constant to extract K_t. Both the backscattering and attenuating properties of the particle on the acoustic beam must be taken into account.

The form function f describes the backscattering component. In the case of a sphere it is defined as (Thorne & Meral, 2008);

$$f = \frac{2rP_s}{aP_i}, \tag{2.2}$$

where P_s is the scattered pressure at distance r, P_i is the pressure incident on the particle, a accounts for particle size and the factor of 2 gives f a value of unity for rigid spheres when ka>1 (the geometric scattering regime). The exact analytical expression for the form function of a glass sphere is given by Gaunaurd & Überall (1983);

$$f = \frac{2}{ix}\sum_{n=0}^{\infty}(-1)^n(2n+1)b_n, \tag{2.3}$$

where x = ka and coefficient b_n is a spherical Bessel function of the first order and a Hankel function which solves the scattering pattern of an acoustic beam incident on an elastic sphere. Coefficient b_n is provided in appendix A.4. In a real measurement scenario, scattering actually occurs from a cloud of particles, therefore f must be integrated over the particle size distribution *p(a)* of the insonified volume. The average form function over the size distribution <f>is given by (Thorne & Meral, 2008);

$$\langle f \rangle = \left\{ \frac{\int_0^\infty a_s p(a_s) da_s \int_0^\infty a_s^2 f^2 p(a_s) da_s}{\int_0^\infty a_s^3 p(a_s) da_s} \right\}^{\frac{1}{2}}. \tag{2.4}$$

Thorne *et al.* (1993) demonstrated that there is greater variation in the form function data when a size distribution $\frac{\sigma(a_s)}{a_s} \geq 0.1$ is present and has not been taken account of by integrating over the size distribution <f>.

Similarly the attenuating properties of a particle on an acoustic beam is quantified by the sediment attenuation coefficient α_s (Thorne *et al.*, 1993), introduced in chapter 1 equation 1.10;

$$\alpha_s = \frac{1}{r}\int_0^r \xi(r)M(r)dr.$$

α_s can also defined in terms of the particle's total scattering cross-section σ_t as;

$$\alpha_s = \frac{N\sigma_t}{2}, \tag{2.5}$$

where N corresponds with the number of suspended particles. σ_t is typically normalised by the particle's geometric cross-section πa^2 (Thorne *et al.*, 1993). The corresponding total normalised scattering cross-section is given by;

$$\chi = \frac{\sigma}{2\pi a^2}. \tag{2.6}$$

Substituting χ and N in terms of mass concentration per unit volume ($N = \frac{M}{\frac{4}{3}\pi a^3 \rho}$) into equation 2.6, yields equation 2.7;

$$\alpha_s = \frac{3M}{4 < a_s > \rho_s} < \chi > . \tag{2.7}$$

This can be written with respect to the sediment attenuation constant as equation 1.11;

$$\xi = \frac{3}{4 < a_s > \rho_s} < \chi > .$$

Therefore in order to quantify a particle's attenuation properties, i.e. ξ, the total normalised scattering cross-section χ must be known. The exact analytical solution for determining χ is given by Gaunaurd & Überall (1983);

$$\chi = \frac{2}{x^2} \sum_{n=0}^{\infty} (2n+1) b_n^2. \tag{2.8}$$

χ must be integrated over the particle size distribution of the insonified volume, hence the average χ over the particle size distribution, $\langle \chi \rangle$, is defined as (Thorne & Meral, 2008; Thorne *et al.*, 1993);

$$< \chi >= \frac{\int_0^\infty a_s p(a_s) da_s \int_0^\infty a_s^2 \chi p(a_s) da_s}{\int_0^\infty a_s^3 p(a_s) da_s}. \tag{2.9}$$

Equations 2.3 and 2.8 are a somewhat complex method of determining f and χ. Sheng & Hay (1988) demonstrated a heuristic approach of fitting measured data with the models stated in equations 2.3 and 2.8, and thus developed somewhat simpler semi-empirical equations for the calculation of f and χ. The heuristic approach utilised a rational fraction to fit the data to the model in equations 2.3 and 2.8. Crawford & Hay (1993) took a similar approach and presented a purely

empirical equation for the evaluation of f and χ, thus removing the requirement of analysing complex Bessel and Henkel functions. Consequently several authors progressively presented equations with increasingly improved fit of measured data with prediction Schaafsma & Hay (1997); Thorne & Buckingham (2004). Notably, each author utilised the data of their predecessors alongside their own data. Measurements were taken in $\frac{1}{4}\phi$ sieved size fractions which lead to improved data fitting. The heuristic method yielded a two order polynomial equation for the calculation of f, and a four order polynomial for χ. Betteridge *et al.* (2008) documents the most current versions specifically for evaluating f and χ of spherical particles;

$$f = \frac{\zeta x^2}{1.17 + 0.95x^2}, \tag{2.10}$$

$$\zeta = (1-0.5e^{-}((x-1.5)/0.5)^2)(1+0.4e^{-}((x-1.5)/3.0)^2)(1-0.5e^{-}((x-5.9)/0.7)^2), \tag{2.11}$$

$$\chi = \frac{0.24\varphi x^4}{0.7 + 0.3x + 2.1x^2 - 0.7x^3 + 0.3x^4}, \tag{2.12}$$

$$\varphi = 1 - 0.4e^{-}((x - 5.5)/2.5)^2. \tag{2.13}$$

These heuristic equations resulted from the fitting of two sets of previously published data alongside their own data. Similarly Thorne & Meral (2008) collated four sets of published function form data and six sets of published attenuation data on irregularly shaped sandy sediments to develop empirical equations for calculating f and χ, for coastal scientists. The corresponding heuristic equations, previously introduced in section 1.4 take into account the ratio of elasticity and density of sand grains with respect to water;

$$f = \frac{x^2(1 - 0.35e^{-}((x - 1.5)/0.7)^2)(1 - 0.5e^{-}((x - 1.8)/2.2)^2)}{1 + 0.9x^2},$$

$$\chi = \frac{0.29x^4}{0.95 + 1.28x^2 + 0.25x^4}.$$

The data relating to the determination of χ were collected using direct measurement of attenuation with a hydrophone similar to backscatter measurement and

then processed via the Bessel and Hankel function equation 2.8 (Thorne *et al.*, 1993). This enabled the subsequent determination of sediment attenuation constant ξ. Recently Rice *et al.* (2014) presented a simpler empirical method to measure ξ directly and subsequently evaluate the system constant $K_t K_s$, previously discussed in section 1.4. Upon combining this technique with the simple system calibration approach with known scatterers to determine K_t, it is possible to decouple K_t from the system constant to obtain K_s.

Essentially, the aim of this chapter is to establish a simpler protocol to evaluate K_t and ξ independently, such that K_s may be extracted. The process undertaken to achieve this, is illustrated in a flowchart in figure 2.1. Unfortunately to determine K_t, K_s must be known in the first place. To begin with, K_s is calculated via the Thorne model (Thorne & Hanes, 2002) using equation 1.6, which requires the form function calculated from the heuristic equations for spherical particles in equation 2.3. Then the sediment attenuation coefficient α_s is determined via two routes; the Thorne equations 1.6 and 1.10, and the Rice method. Values for K_t are subsequently derived via equation 2.1, from knowledge of these two quantities. Note that via the Thorne model route, an integration was not conducted over the particle size distribution as in equations 2.3 and 2.8, rather the $D_{[50]}$ values were utilised assuming a narrow and monodisperse size distribution.

The process ends here in the case of the Thorne model, where K_t is derived from estimated values of K_s and α_s. An additional step is taken in the Rice method route, where the measured values of α_s and K_t are used to determine K_s. Indeed this method of obtaining a measured value of K_s is undoubtedly cyclic. However this approach is taken to enable comparison of f and χ obtained via both routes.

Coastal scientists are typically concerned with large particles at dilute concentrations (Rose & Thorne, 2001), thus ABS calibration has typically been conducted with large particle radii ranging 50-400 µm to ensure measurable backscatter signal at dilute concentrations. This combination is also to ensure that the echo does not undergo viscous attenuation. Particles are sieved into $\frac{1}{4}\phi$ size fractions which range $\pm 0.09 a_s$. Contrarily engineering scenarios often involve smaller and colloidal particle sizes. There is little data published on small radii and correspondingly small ka in the Rayleigh scattering regime. However, since the

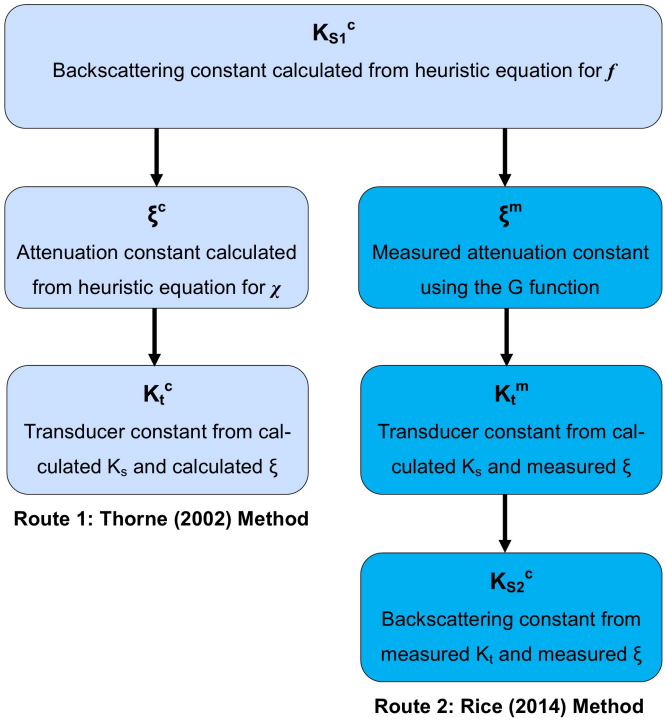

Figure 2.1: Process flowchart outlining the Thorne and Rice method routes.

focus of this research and interest lies in extending the application of the ABS to non-marine suspension systems, it is important to investigate what happens to the form function and total normalised scattering cross-section at low ka values. Therefore in this chapter, calibration was trialled with correspondingly smaller size fractions a_s<50 µm. In this case, all investigated particles were within the Rayleigh scattering regime where ka<1. Because the wavelength is much larger than the particle diameter, scattering is considered independent of shape, so one can assume that an irregularly shaped particle would scatter similar to a sphere (Thorne & Meral, 2008). For this reason f and χ was evaluated and compared via the heuristic equations for both spherical (Betteridge *et al.*, 2008) and irregularly shaped particles (Thorne & Meral, 2008). Note there is currently very little published data on the form function and total normalised scattering cross-section in the Rayleigh scattering regime, which is the region of interest for further application.

2.2 General Methodology

The commercial ABS system utilised in all experiments in this report is the AQUAscat 1000 (Aquatec Group Ltd, Hampshire UK). A illustration of the general experimental set-up in the laboratory is given in figure 2.2. The ABS comprises a processing box which enables up to four transducers to be deployed in sequence and in parallel, operated via a software program. In a simple operating regime, one transducer is submerged within a suspension such that its face is below the waterline, to ensure that the speed of sound is not altered in the case where the acoustic beam travels between different media, e.g. from water to air. Likewise it is important to sufficiently degas the dispersion prior to measurement and remove any air bubbles accumulated on the transducer face, to negate resonant scattering contributions to the measured signal (McClements, 1991; Meral, 2008). Bubble resonance frequency is proportional to the reciprocal of the bubble diameter. Dukhin & Goetz (2001) states that a 10 µm bubble has a resonance frequency of approximately 0.6 MHz. So bubbles need to be smaller than 10 µm to have any significant influence. This should not be a problem because small bubbles are unstable and tend to dissolve anyway.

It is important during instrument set-up to ensure that any possibilities of interference with the backscatter measurement from suspended particles are negated, for example from sidewall reflections or any other apparatus present in the experimental tank. Any possible interferences can be predetermined by estimating the width of the insonified region from the spreading half-angle γ_0 with respect to distance r from the transducer (MET-FLOW, 2002);

$$\gamma_0 = \sin^{-1}(\frac{0.51\lambda}{D_t}), \tag{2.14}$$

where λ and D_t correspond with the wavelength and active element diameter respectively. The location of the natural focus point N can be found by (MET-FLOW, 2002);

$$N = \frac{D_t^2 f_r}{4c}, \tag{2.15}$$

where f_r and c denote the frequency in MHz and the speed of sound in water respectively. Measured data within the near-field zone requires correction (see

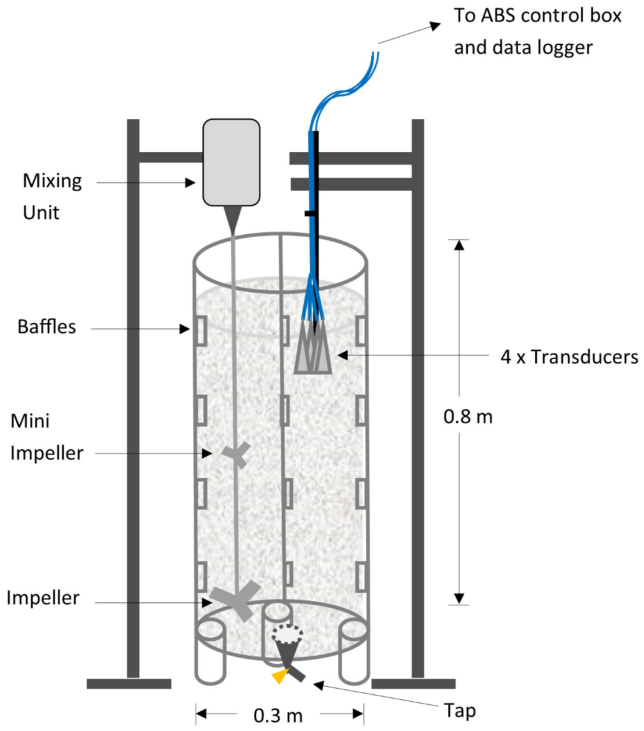

Figure 2.2: General set-up schematic

equation 1.5 for ψ), due to departure from spherical spreading, (refer to chapter 1 figure 1.4C. Examples of spreading width and focus point locations are tabulated in table 2.1 at distances r for reference. These data depict that the angle of spreading is enhanced for lower frequencies and smaller crystal diameters. Note that these values were calculated taking a nominal speed of sound in water value of $1485\,\mathrm{m\,s^{-1}}$, corresponding with average temperature 20-21 °C. Notably, temperature of the water influences the speed at which the sound wave propagates, whereby the speed increases by approximately $3\,\mathrm{m\,s^{-1}}$ with a 1 °C increase in temperature (Rossing, 2007). Therefore taking suspension temperature measurements alongside ABS profiling is a good practice to maintain accuracy in subsequent calculations of parameters which include the wavelength and speed (Chanamai *et al.*, 1998). The presence of suspended particles also influences the wave speed (Temkin, 2005) however it is thought that the resulting variations would be minor for small profiling depths (Hunter *et al.*, 2012a).

Table 2.1: Insonification diameter at transducer range; 0.5 m and 1 m

f (MHz)	λ (cm)	D (cm)	N (cm)	γ_0	Spread (cm) at r 0.5 m	Spread (cm) at r 1 m
1	0.148	2.0	6.73	2.17	3.78	7.55
1	0.148	1.9	6.08	2.28	3.99	7.98
2	0.074	1.0	3.37	2.17	3.78	7.55
4	0.037	1.0	6.73	1.08	1.89	3.77
5	0.003	1.0	8.42	0.86	1.51	3.02

The AQUAscat 1000 enables operation of a maximum of four transducers in sequence. It is possible to select a pulse repetition rate ranging 4-64 Hz. A simple calculation of $t = \frac{d}{c}$ can be conducted to enable selection of an appropriate pulse rate, which incorporates enough time for the pulse to propagate through the entire suspension depth and echo back to the transducer prior to the emission of the next sequential pulse. The number of transducers operating in sequence also requires consideration.

The measured backscatter response data typically follow a Rayleigh probability distribution (Thorne & Hanes, 2002). Random fluctuations arising from self-noise and ambient noise from the fluid (Rehman & Vincent, 1990) are prevalent, and are a primary source of error. Therefore an ensemble average of backscatter measurement is required (Libicki *et al.*, 1989) to negate fluctuations. Measurement accuracy can be improved via the sampling rate and vertical resolution selections. For this reason it is ideal to select as high as practicable pulse emission rate, so that as much data is collected to provide an ensemble average per measured profile which reduces these variations somewhat. Consequently a reduction in measurement time required to achieve data with reasonably reduced inherent variations is also achieved. Although complete negation is not possible, and some data smoothing is still required post measurement. Thorne & Hanes (2002) suggests that around 100 measurements corresponds with 5% precision in Vrms measurement, and 10% precision in concentration estimate using the inversion method. In all experiments conducted in this report, a pulse emission rate of either 32 or 64 Hz was selected. The higher rate was selected in the case of settling suspension experiments to ensure timely capture of suspension profiles

in dynamically changing systems. The profiling rates corresponds with a total of 19,200 or 38,400 measurements taken respectively, in a ten minute profiling duration for example, markedly improving VRMS accuracy.

The AQUAscat software also enables selection of profile storage rate. For all experiments, one average profile was stored per second. Each profile is segregated into distance bins such that it is possible to discern the echoed pulse intensity at any specified range r from the transducer. In all experiments, distance bin sizes of 2.5 or 5 mm were selected. The larger bin size was chosen in the case where a longer profiling depth was required, albeit at the expense of vertical resolution. On a final note with respect to general methodical considerations, the measurement threshold of the AQUAscat 1000 requires mention. The manufacturer states that -72 dB is the threshold beyond which there is no longer a linear correlation between measured echo pressure and the resulting electronic voltage that is recorded, therefore any measured intensity beyond -72 dB should be disregarded. In previous work reported by the author with respect to ABS profiling of titanium dioxide dispersions (Bux *et al.*, 2015), it was found that the backscatter intensity profile began tailing off in a non-linear manner slightly prior to the -72 dB threshold. Therefore in all corresponding analysis the threshold level was raised to account for a safety margin; -65 dB was selected.

All considerations discussed thus far were applied to the general methodical approach towards all experimental work. The proceeding discussion prescribes the specific method and materials employed in the calibration of the ABS and determination of the particle specific acoustic constants; K_s and ξ for spherical glass beads. Note the approach taken here is generally applicable for all experiments in this report. Any deviations in procedure, apparatus and particle specificities are noted in the corresponding chapters.

2.3 Experimental Procedure & Materials

2.3.1 Materials and their Characterisation

Betteridge *et al.* (2008) outline a procedure for ABS calibration. In the proceeding experiments, this general methodology is adapted with some important

variations, mainly to improve measurement accuracy, and reduce experiment duration. Particle size was the first significant variable. Smaller particles were utilised since these are of interest with respect to a multitude of engineering suspension applications, where products either exist in or pass through a colloidal state during processing (Challis *et al.*, 2005). Spherical glass particles were selected for the experiments to determine K_t, ξ and K_s, for reasons discussed in section 2.1. This material is also cheap and readily available. In the calibration procedure prescribed by (Betteridge *et al.*, 2008; Thorne & Hanes, 2002), particle radii $>100\,\mu m$ are typically utilised in very dilute concentrations ranging 0.2-0.8 $kg\,cm^{-3}$. The use of dilute concentrations is to ensure that the echoed pulse is not highly attenuated. However in dilute cases, large particles within the scattering regime (refer to figure 1.2), are required to ensure measurable scattering. Hence for calibration, dilute concentrations and large particles are prescribed (Betteridge *et al.*, 2008; Thorne & Hanes, 2002). They also utilise very low pulse emission rates, typically around 4 Hz to ensure that any interfering reflected waves have dissipated prior to the emission of the subsequent pulse. This approach is very time consuming as lengthy measurement durations are required to achieve a meaningful signal, where the influences of inherent noise fluctuations are reasonably negated. Variations are more prevalent from the ambient fluid in very dilute cases where there are few scatterers.

Honite 16 and Honite 22 spherical glass beads (Guyson International Ltd, Skipton UK) were used in the proceeding experiments. Size distributions of the particles were obtained via the Malvern Mastersizer 2000 (Malvern Instruments, Worcestershire UK). This instrument uses a dynamic light scattering method for obtaining particle size. Essentially, a laser is passed through a dispersion and scatters when incident with suspended particles. The angle of diffraction is dependent on the size of the scatter. Hence the instrument measures the angle and intensity of the diffracted laser beam, and equates this to a volume equivalent diameter of a sphere using the Mie theory for light scattering. Optical properties of the scatter must be known. In the case of Honite, a refractive index of 1.52 for standard spherical glass beads was used. The measurement protocol is a follows; the Honite sample was dispersed in water until a sufficient lens obscuration was achieved in the measurement cell, three samples were measured

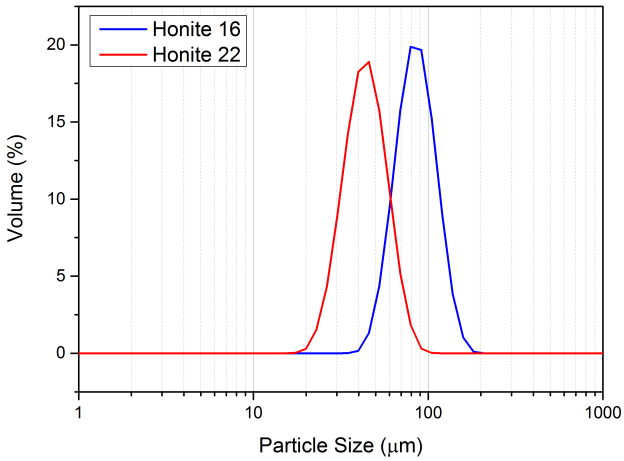

Figure 2.3: Size distributions of Honite 16 and 22

per particle type, three measurement runs were conducted per sample and ten measurements were performed per run. The resulting average size distributions of Honite 16 and Honite 22 are presented in figure 2.3. Other relating parameters are also quantified in table 2.2. The measured particle sizes are quoted as D-values; $D_{[10]}$, $D_{[50]}$ and $D_{[90]}$. $D_{[50]}$ is the median size, so 50% of the sample mass has a size above this value and 50% below this value. 10% of the sample mass has a size below the $D_{[10]}$ value and 90% of the particles have a size below the $D_{[90]}$ value. The *Span* of the size distribution is given by;

$$\text{Span} = \frac{D_{90} - D_{10}}{D_{50}}. \tag{2.16}$$

This is a useful way of quantifying the narrowness of the distribution, thus inferred monodispersity. Alternatively the coefficient of variation quantifies the variation as the ratio of the standard deviation (θ) to the mean size (μ), where increasing C_ν corresponds with increasing variability;

$$C\nu = \frac{\theta}{\mu} \tag{2.17}$$

The particle size distribution follows a Gaussian distribution curve. The $D_{[50]}$ for Honite 16 and Honite 22 are 78.9 µm and 40.5 µm respectively, corresponding

Table 2.2: Size distribution and density data for Honite 16 and 22, where σ is the standard deviation in size measurements.

Particle	D_{50} (µm)	σ	$C\nu$ (%)	*Span*	ρ (kg m^{-3})
Honite 22	40.49	0.04	0.1	0.73	2453.1
Honite 16	78.85	0.43	0.55	0.68	2469.6

with radius of 35.9 µm and 20.3 µm. Values for the *Span* ($\pm$ 0.7a_s) and $C\nu$ (0.1%) are low indicating narrow distributions. Although the *Span* of the $\frac{1}{4}\phi$ sieve fractions (Betteridge *et al.*, 2008) ranges $\pm$ 0.09 a_s, the smallest available sieve size is in the region of 40 µm diameter, therefore the smallest size fraction cannot be sieved for greater accuracy, thus the variability in the lowest size fraction should be comparable.

The density of Honite 16 and 22 was measured via the Micrometrics Accu-Pyc 1330 helium pycnometer (Micrometric Instrument Corporation, USA). A known mass of dry powder sample was placed into the instrument, which purges the cell with helium gas. The volume of the sample is determined by the difference in gas with and without sample, thus inferring density. The instrument repeats the procedure until ten consecutive measurements yield density values within 0.001 standard deviations. Density measurements of three samples per particle type were conducted. The average densities for Honite 16 and 22 are given in table 2.2. The two particle types are very close in density.

Particle size and shape were also characterised via scanning electron microscopy (EVO MA15 SEM, Carl Zeiss Ltd., UK). Each sample stub was prepared by sticking powdered sample onto a carbon sticker and excess powder was removed. The stubs were coated with palladium of 10 nm thickness to prevent charging during imaging. SEM images of Honite 16 and 22 at two magnifications are depicted in figure 2.4. The images corroborate the particle size measurements conducted via the Mastersizer. Furthermore they show that the particles have a nominally spherical shape although some beads do have odd nodules. The particles used by Betteridge *et al.* (2008) also shared similar characteristics, however a good fit with the scattering model for spheres was still demonstrated.

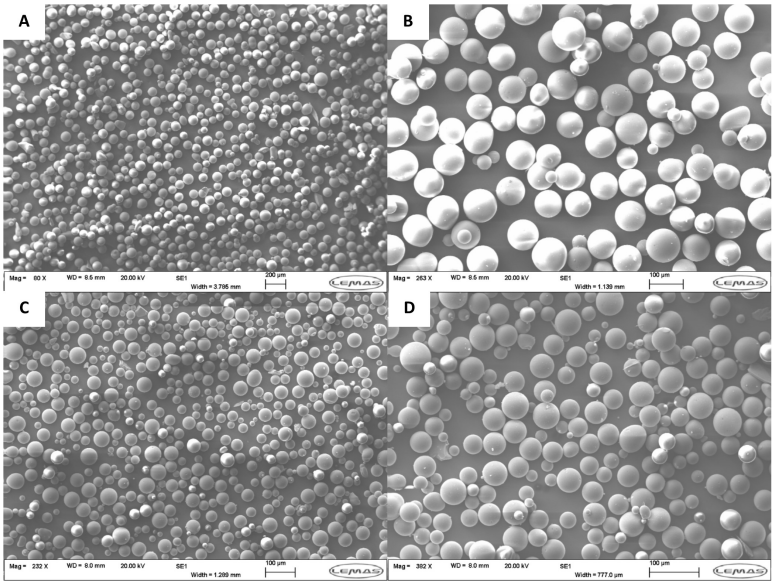

Figure 2.4: SEM images; Honite 16 at magnification (a) x 80,000, (b) x 263,000 and Honite 22 at magnification (c) x 232,000, (d) x 382,000

2.3.2 ABS Method

The tank set-up utilised in this report is previously seen in figure 2.2. Specifically it is a Perspex column with 30 cm diameter x 80 cm height, comprising four 2 cm thick baffles. The waterline was set at 60 cm. A mixing impeller running at 1640 rpm was positioned off-centre 10 cm from the base. Since the impeller shaft is positioned off-centre and there are no additional internal structures, as long as the transducers are positioned such that the insonified volume determined from the beam spreading half angle is clear of any obstruction, it is unlikely that additional unwanted reflections would be incurred. The time taken for an emitted pulse to propagate to the column base located at range 55 cm and echo back to the transducer is 0.0007 s for a suspension at 20 °C. Therefore even opting for the highest possible pulse emission rate of 64 Hz is acceptable, since there is a 0.0156 s duration between successive emissions. Each stored profile is an ensemble average of the measured data so selecting a higher rate enables more data capture per average stored profile. Thus reducing variation in the Rayleigh distributed data, as well as reducing the time required to capture good average data profiles in which inherent noise levels are reduced.

The smaller particles were profiled at dilute concentrations 0.2-0.7 kg cm^{-3} as prescribed by Betteridge *et al.* (2008), in order to obtain data which is not dominated by viscous attenuation effects. Furthermore intermediate concentrations (1-10 kg cm^{-3}) were also investigated to determine the highest possible concentration scenario for calibration before attenuating influences become dominant due to inter-particle scattering (Hunter *et al.*, 2012a). K_t is independent of concentration, thus it is beneficial to obtain as much data as possible, up to the point where attenuation effects start to be experienced. A pulse emission rate of 32 Hz was applied to reduce measurement time and variability in the average backscatter profiles.

A homogeneity check was conducted prior to acoustic experimentation since uniform particulate dispersion is integral to drawing an accurate relationship between backscatter attenuation and concentration (Moore *et al.*, 2013a). Specifically Honite 22 dispersions with nominal bulk concentration of approximately 25, 50 and 75 kg m^{-3} (1.0, 1.7 and 2.5 vol%), were prepared to a 70 cm waterline and continuously mixed at 1640 rpm. 3 x 20 ml samples were extracted via a peristaltic pump at each depth; 12.5, 25 and 50 cm. The samples were weighed wet, dried in an oven at 55 °C for 24 hours and weighed dry. The dry/wet ratios enabled calculation of suspension concentration at each depth. The results of the homogeneity test are depicted in figure 2.5. These data demonstrate that the samples taken at each depth are within the region of the bulk concentrations (depicted as the dashed line), indicating that the off-centred impeller was successful at suspending the Honite homogeneously throughout. Since dispersion homogeneity is essential in the proceeding experiments, additional homogeneity checks were conducted in between concentration runs.

For the calibration experiments the following concentrations were profiled, Honite 16; 0.25, 0.5, 1, 10 kg m^{-3} and Honite 22; 0.25, 0.5, 1, 2.5, 5, 10 kg m^{-3}. In order to obtain the sediment attenuation constant and the backscattering constant as per the Rice method (Rice *et al.*, 2014), additional concentrations were profiled in both cases; 25, 50, 75 kg m^{-3}. The ABS system comprises three sets of transducers, set 1; 1, 2, 4 MHz, set 2; 1, 2, 4, 5 MHz and set 3; 1, 2 MHz. The ABS profiled each concentration for each transducer set for 3 x 10 min durations. A minimum of 10 minutes was allowed between sediment addition and

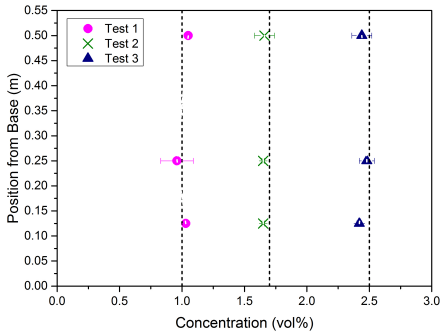

Figure 2.5: Concentration with respect to depth in three homogeneity tests in Honite 22 dispersions; Test 1 (1.0 vol%), Test 2 (1.7 vol%) and Test 3 (2.5 vol%).

ABS measurement to enable thorough mixing and degassing (i.e. no visible bubbles). Average backscatter intensity profiles were ascertained per concentration. Dispersion temperature measurements were made manually with a thermometer in between each probe set measurement per concentration.

2.4 Results & Discussion; Calibration & Acoustic Constants

Initially this section reports on the measured sediment attenuation constant ξ obtained for the two particles via the Rice Method (Rice *et al.*, 2014). The calibration constants K_t are then reported for each transducer and compared for the Rice method and the Thorne model (Thorne & Hanes, 2002). The measured backscattering constant K_s is then derived from measured values of ξ and K_t from the Rice method (refer back to process flowchart in figure 2.1. Furthermore, this section outlines the general approach taken to analyse the ABS data. This method is generally utilised throughout successive chapters.

2.4.1 Backscatter Profiles

Backscatter profiles are typically represented as changes in measured intensity with respect to transducer range. Thus in the first step of the analysis process

the measured voltage was converted into decibels; $20\log_{10}(V_{RMS})$. The backscatter profiles are presented in figure 2.6 in decibels. The average backscatter intensity over three runs is presented with respect to transducer range. The profiles for a range of four concentrations are shown at each frequency; 1, 2, 4 and 5 MHz, A-D respectively for Honite 22, and E-H respectively for larger Honite 16 particles. The dashed line at -65 dB represents the threshold selected for data analysis cut-off.

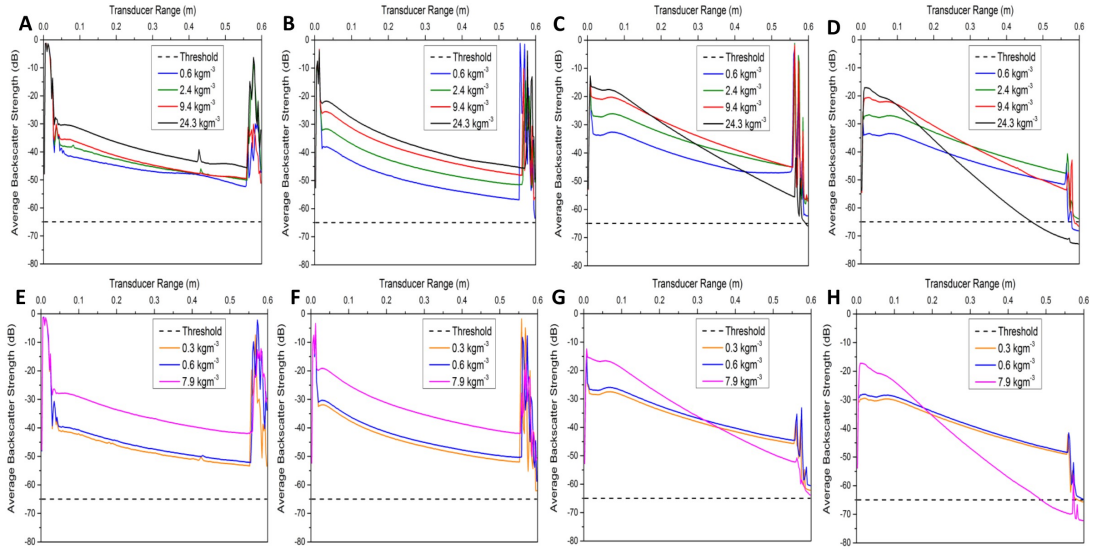

Figure 2.6: Average backscatter intensity with respect to transducer range for, Honite 22 via (a) 1 MHz, (b) 2 MHz, (c) 4 MHz, (d) 5 MHz, and Honite 16 via (e) 1 MHz, (f) 2 MHz, (g) 4 MHz, (h) 5 MHz. Note dashed line at -65 dB, indicates the signal cut-off threshold.

All profiles A through to D, and E through to H, display characteristics which are typical of attenuating dispersions for the respective particles. Initially there is the region closest to the transducer exhibiting near-field interferences; corresponding with the regions up to to approximately; 6.7, 3.4, 6.7 and 8.4 cm for 1, 2, 4 and 5 MHz respectively. Subsequently from the focus point, the intensity of the profiles recede in the far-field range owing to natural absorption, dissipation and thermal losses, akin to figure 1.4C. The propagating intensity is also

augmented via scattering and absorption losses from interaction with suspended particles (Temkin, 2005).

Any regions which are relatively dense in particles such as a sludge interface, tank walls or internal structures, behave as strong scattering surfaces and thus peak in backscatter intensity. In this case, the peak at 55 cm denotes the position of the column base from the transducer location. The strength of the base peak diminishes with increasing concentration and frequency until it is no longer visible in the highest concentration scenario at 5 MHz. These observations align with the typical reduction in penetration depth with increasing frequency. Augmentation from increasing concentration is due to the enhancement of inter-particle scattering events, whereby the echoed waves are more likely to deviate from their path to the transducer (Hunter *et al.*, 2012a). Although overall penetration depth is reduced, the initial intensity is enhanced since the higher particle concentration behaves as a stronger scattering plane at the initial focus point. Additionally some 1 MHz profiles in figure 2.6 also display a small peak at approximately 0.4 m depth. This is likely an interference peak resulting from a focus of reflective waves scattering from the sidewall or the off-centred mixing shaft and impeller, due to the positioning of the 1 MHz transducer. The active element diameter of the 1 MHz is double that of the other transducers. It is likely that the specific transducer may not have been positioned in an optimal location to avoid unwanted interference. Since there is a high level of noise variation associated with this frequency, the interference did not manifest in an obvious manner in the real-time measurement software.

It is possible to directly compare the 0.6 $\mathrm{kg\,m^{-3}}$concentration profiles of Honite 22 (A-D), with those of Honite 16 (E-H). The intensity of the echoed wave is markedly stronger in the case of Honite 16, the larger particle species. This is because the particles move out of the viscous attenuation range (refer to figure 1.2). The gradient of the profiles, which corresponds with the rate of signal decay, or otherwise the attenuation, is slightly steeper in the case of Honite 22, the smaller particle species. Honite 22 has a radius of 20 µm which is well within the viscous attenuating region (Moore *et al.*, 2013a). Interestingly, the attenuation is enhanced in the Honite 16 profile at 7.9 $\mathrm{kg\,m^{-3}}$, compared with the Honite 22

profile at $9.4\,\mathrm{kg\,m^{-3}}$, a higher concentration. The Honite 16 dispersion experiences enhanced inter-particle scattering at this intermediate concentration, due to the increased scattering attenuation, i.e. scattering at angles other than 180° due to the larger particle size, (refer back to figure 1.1).

2.4.2 Attenuation Constant

In order to determine the sediment attenuation constant via the Rice method (Rice *et al.*, 2014), it is necessary to plot the voltage normalised by distance and near-field correction factor, $G = \ln \psi V r$ with respect to transducer range, such that the change in $\frac{dG}{dr}$ with respect to concentration change can be derived. In doing so it is possible to calculate the sediment attenuation constant $\xi = -\frac{1}{2}\frac{d[\frac{G}{dr}]}{dM}$ (introduced in section 1.4). Therefore in the second stage of the analysis process, the measured voltage was normalised to plot G against r. The G profiles corresponding with the decibel backscatter profiles of Honite 22 and 16 previously seen in figure 2.6, are displayed in figure 2.7A-D. The solid and dashes lines correspond with Honite 22 and Honite 16 profiles respectively, where A-D correspond with 1, 2, 4 and 5 MHz. With the exception of the interference in the 1 MHz profiles, G is found to vary linearly with r, in accordance with the G function. Referring back to chapter 1 figure 1.8, Rice *et al.* (2014) observed this to be the case within a very small transducer range, in turbulent dispersions in a pipe-flow of few centimetres depth. Importantly, figure 2.7 highlights that G actually varies linearly over a much greater range.

The average linear slope of each G profile was then determined for the range 0.1-0.4 m, and plotted against the corresponding concentration. Any G profile with an r-squared fit <0.9 was excluded from the analysis. Figure 2.8 exhibits the plot of $\frac{dG}{dM}$ versus M for Honite 22 all frequencies; 1, 2, 4 and 5 MHz A-D respectively, for all transducer sets. The figure depicts a linear reduction in $\frac{dG}{dr}$ with respect to increasing concentration. The gradient steepens with increasing frequency, inferring typical enhancement of signal attenuation (Hunter *et al.*, 2012a). The absolute values and associated gradient between transducer sets of the same frequency are close. $\frac{dG}{dr}$ essentially depicts the particle specific relationship between attenuation and concentration.

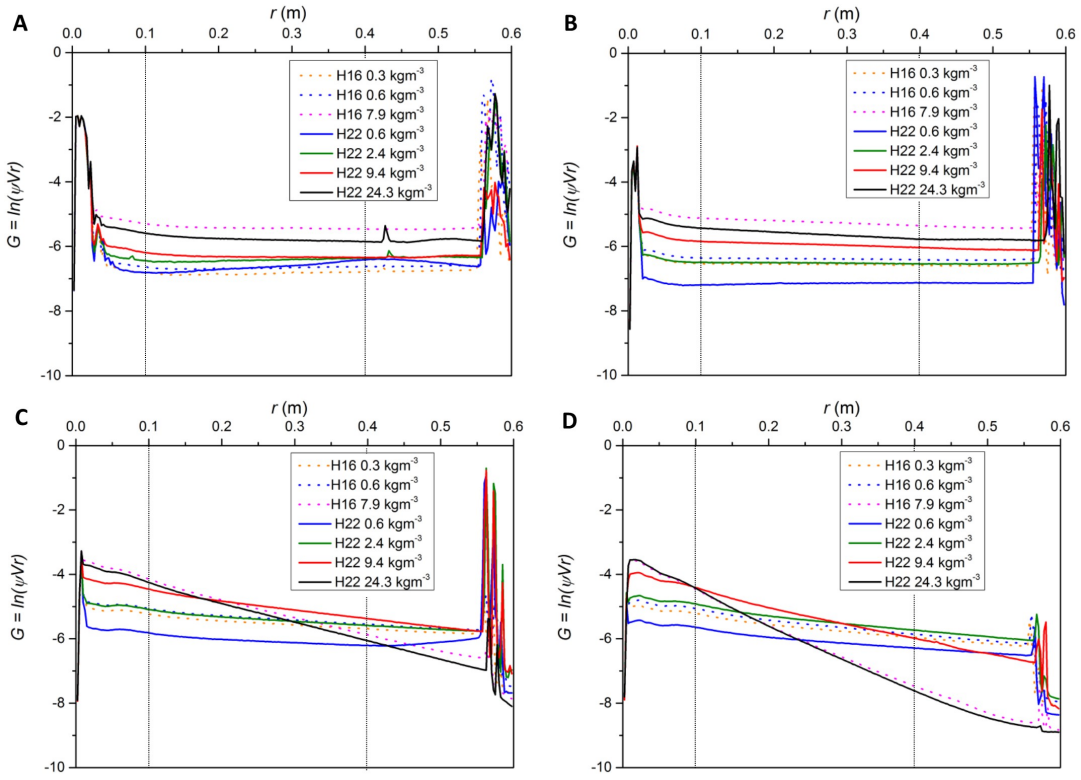

Figure 2.7: G function with respect to range for, Honite 22 (solid lines) and Honite 16(dashed lines), via (a) 1 MHz, (b) 2 MHz, (c) 4 MHz, and (d) 5 MHz. Note vertical lines indicate the analysed data regions.

The sediment attenuation constant was subsequently determined from the slopes; $\xi = -\frac{1}{2}\frac{d[\frac{G}{dr}]}{dM}$. The corresponding constant for both particle types with each corresponding frequency are listed in table 2.3. Specifically the values for each frequency are an accumulated average between transducer sets. In general, the magnitude of ξ increases with increasing frequency as expected. ξ measured via the Rice method is compared with values calculated via the empirical equations for the total normalised scattering cross-section; equation 1.12 and 2.12. The measured values align well with the predicted values from the two models. The greatest difference is observed in 1 MHz for which the measured data variation was greater anyway, due to inherently less sensitivity of this lower frequency (Hunter *et al.*, 2012a). Also the 1 MHz data correspond with very low ka, in the region

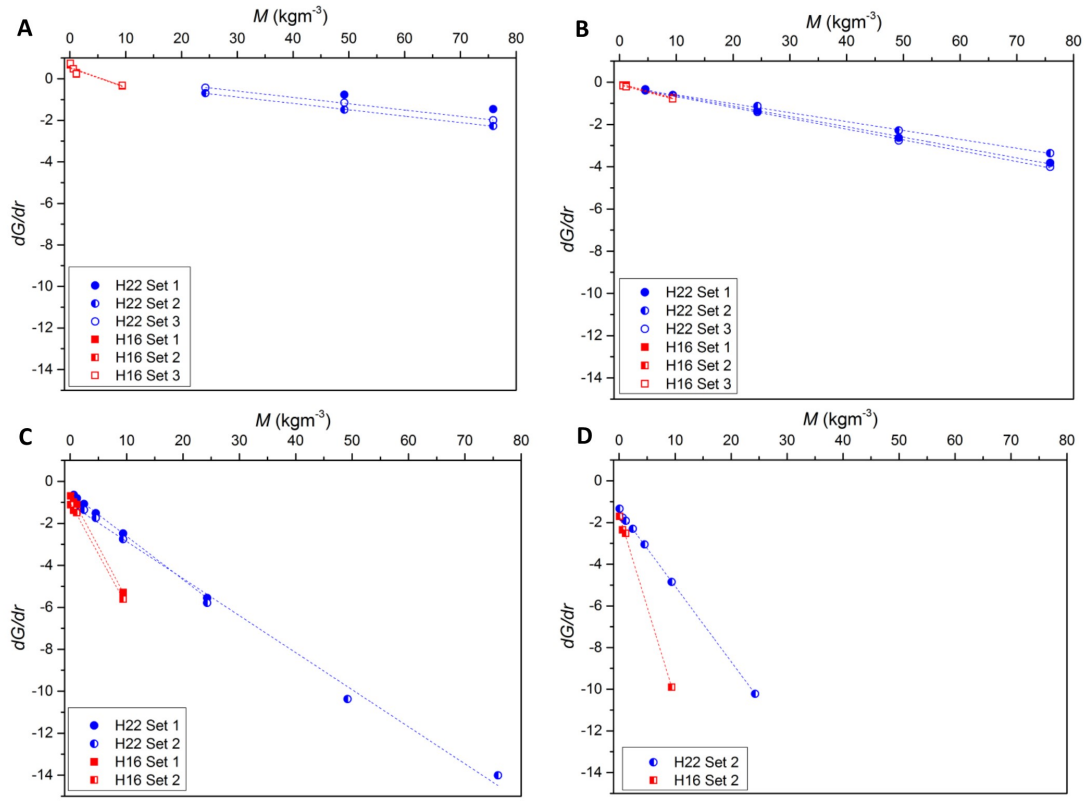

Figure 2.8: $\frac{dG}{dr}$ versus concentration for Honite 16 and 22; all transducer sets via (a) 1 MHz, (b) 2 MHz, (c) 4 MHz, and (d) 5 MHz.

where the fit of χ is not established with data (Vincent & MacDonald, 2015).

The measured values of ξ obtained via the Rice method were then used to calculate the associated dimensionless parameter, the total normalised scattering cross-section equation 1.11. The results were then plotted against dimensionless parameter ka to observe the trend in χ at low ka values. Measured χ is compared to predicted χ from both models in figure 2.9. Measured values of χ for Honite 16 and 22 align with both predicted models at ka >0.4. However there is a strong deviation at low ka <0.4. Notably, the models did not take into account any data within this very low ka region, and a linear extrapolation was assumed. Hence, the measured data presented here is significant in providing information on the behaviour of χ in the very low ka region.

Table 2.3: Comparison of measured ξ ($\mathrm{kg^{-1}\,m^{-2}}$) with calculated and literature values. Where σ corresponds with the standard deviation of the measured values.

Particle	f_r (MHz)	Measured ξ^m	σ^m	Calculated ξ^b	Calculated ξ^t	ξ^l
H16	1	0.047	0.001	0.002	0.002	-
	2	0.036	0.001	0.022	0.025	0.021
	4	0.247	0.003	0.213	0.279	0.135
	5	0.441	-	0.407	0.546	-
H22	1	0.014	0.001	0.0003	0.0002	-
	2	0.024	0.002	0.004	0.004	0.018
	4	0.096	0.010	0.048	0.054	0.069
	5	0.181	-	0.103	0.123	-

[m] measured from the Rice method (Rice *et al.*, 2014).

[b] calculated using Betteridge *et al.* (2008) equations.

[t] calculated using Thorne & Meral (2008) equations.

[l] measured values from a pipe-flow experiement with a UVP published by Rice *et al.* (2014).

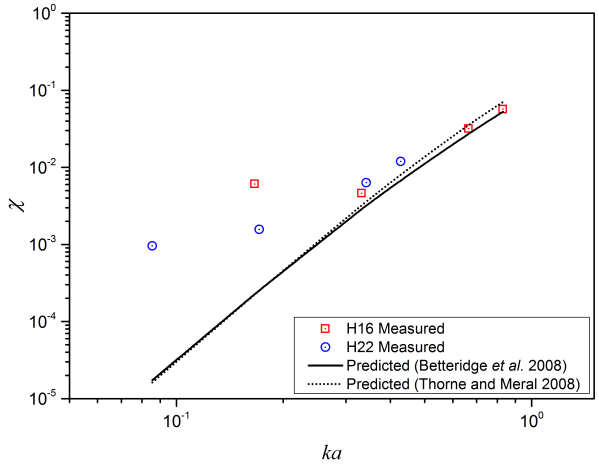

Figure 2.9: Comparison of the calculated and predicted total normalised scattering cross-section versus wavenumber, for Honite 16 and 22.

2.4.3 Transducer Constant

The proceeding section reports on the determination of the transducer constant K_t for all probe frequencies in each transducer set. Calculation of K_t requires prior knowledge of the particle specific sediment attenuation ξ and backscatter constants K_s for the associated frequencies. ξ has been predetermined in the preceding chapter. K_s on the other hand is calculated via equation 1.6. Determination of K_t in this section follows two routes, refer to flowchart in figure 2.1. On the first hand, K_s is calculated using the heuristic form function equations given by both the spherical and irregular shape model, since particle size here correlates with low ka. Subsequently, the sediment attenuation coefficient α_s is determined using the heuristic equations for the total normalised scattering cross-section. Values of K_s and α_s are inserted in equation 1.4 to calculate K_t. Essentially, the values of K_t determined via both models are compared. In the second approach the values of K_s from the models are used in conjunction with α_s calculated from ξ measured via the Rice method (Rice *et al.*, 2014), to enable comparison of the resulting K_t with K_t from the models.

K_t is presented with respect to transducer range in figure 2.10, where A-D correspond with 1, 2, 4 and 5 MHz respectively. K_t profiles for Honite 22 transducer set 2 are shown. Note these graphs correspond with the K_t values obtained using K_s via the heuristic form function equation from the irregular shape model (Thorne & Meral, 2008), and αs from ξ measured via the Rice method (Rice *et al.*, 2014). This is the first time that K_t has been assessed in such a way. Note that the irregular shape model (Thorne & Meral, 2008) was determined from a greater number of data sets than the spherical model (Betteridge *et al.*, 2008).

Figure 2.10 demonstrates that for each frequency A-D, K_t is effectively constant with respect to transducer range. K_t calculated via each concentration also depicts only minor variations and there is no clear trend between K_t and concentration, demonstrating its independence from concentration. It is seen here that the use of higher concentrations than those prescribed by Thorne & Hanes (2002) and Betteridge *et al.* (2008) is applicable for calibration. The variation

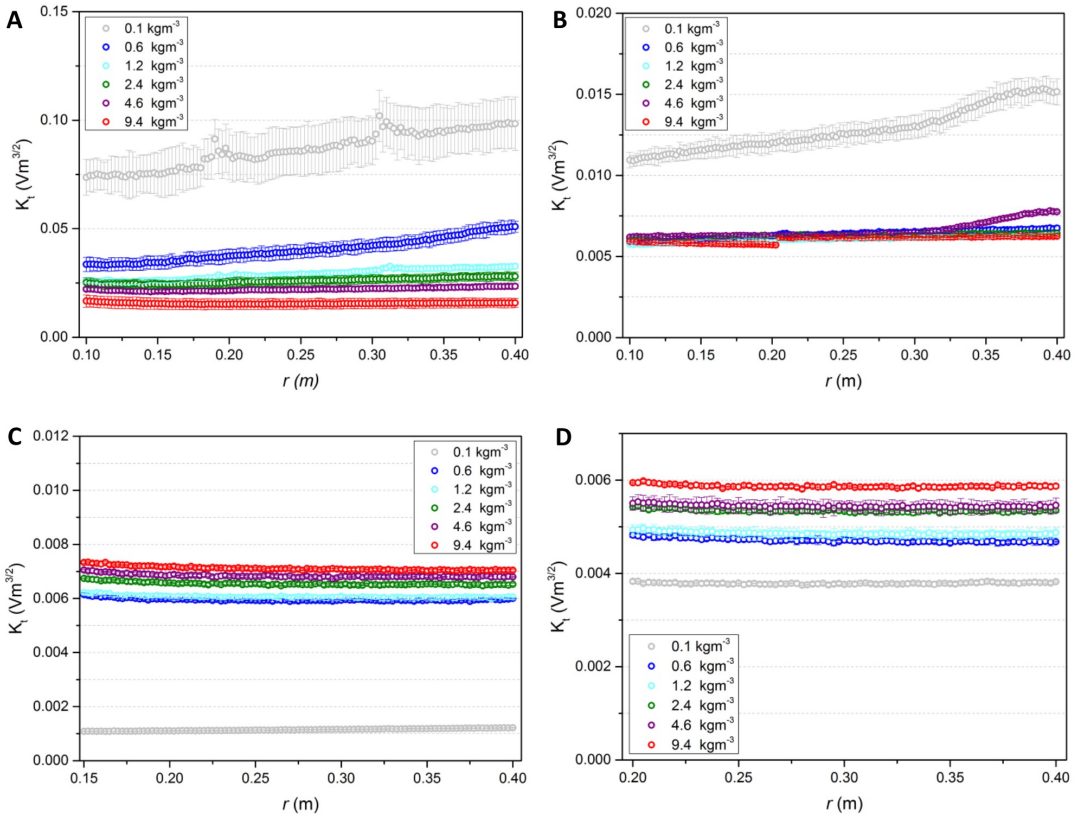

Figure 2.10: Distance averaged transducer constants measured via each concentration of Honite 22 dispersions; (a) 1 MHz, (b) 2 MHz, (c) 4 MHz, and (d) 5 MHz.

in measured data is less at higher concentrations where there are more scatterers present. This is more marked in the case of 1 MHz (figure 2.10). Therefore by utilising intermediate concentrations, lengthy measurement durations are not required and the calibration procedure is more rapid. Interestingly in the case of all frequencies, K_t determined from the lowest concentration $0.1\,\mathrm{kg\,m^{-3}}$ is a large over or under-estimation compared with K_t's determined via the other concentration regimes. It is likely that this concentration is too dilute to provide a meaningful scatter response from the small particles. Indeed this concentration is slightly lower than that prescribed for calibration by Thorne & Hanes (2002) and Betteridge *et al.* (2008). Note there are a few K_t profiles which are not

constant in nature due to variations in the corresponding backscatter profiles, or high concentration related attenuation at the higher frequencies, were negated from further analysis. $0.1\,\mathrm{kg\,m^{-3}}$ profiles from all frequencies, $0.6\,\mathrm{kg\,m^{-3}}$ from 1 MHz, and $4.6\,\mathrm{kg\,m^{-3}}$ from 2 MHz.

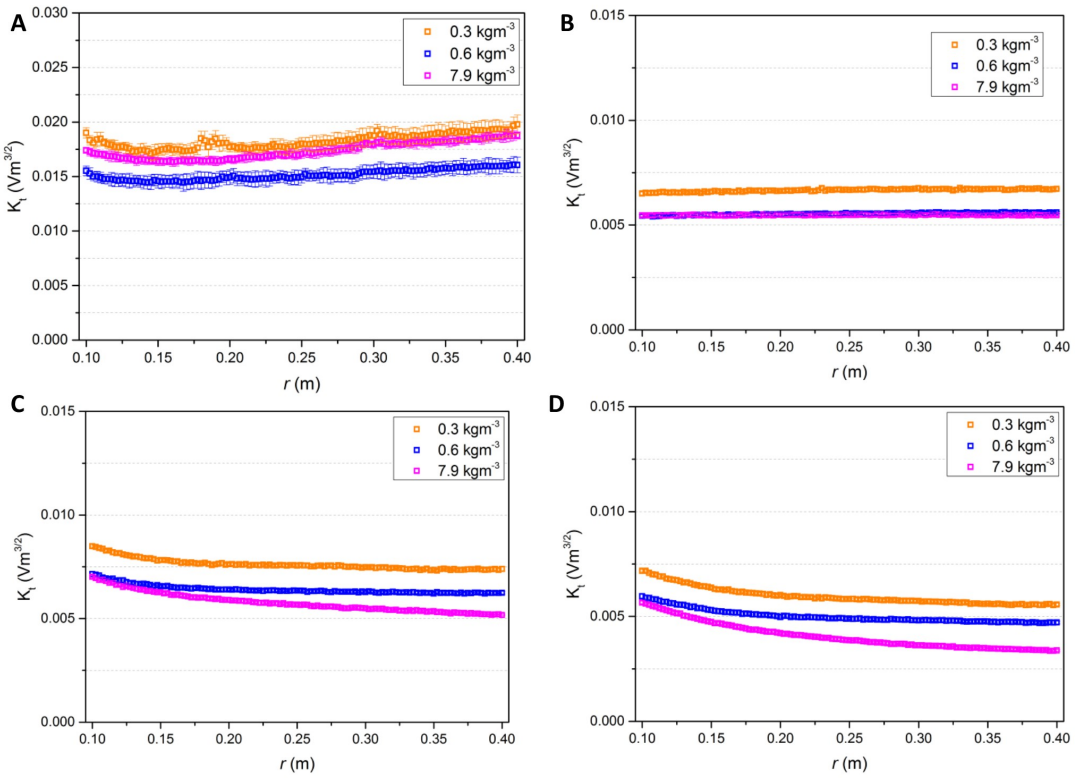

Figure 2.11: Distance averaged transducer constants measured via each concentration of Honite 16 dispersions; (a) 1 MHz, (b) 2 MHz, (c) 4 MHz, and (d) 5 MHz.

The K_t profiles obtained for Honite 16 set 2 probes are also presented in figure 2.11, for comparison. These data also exhibit little variation, such that the error bars are negligible. These profiles are comparable with those of Honite 22 set 2 2 MHz, therefore confirming the independence of the transducer constant to particle size.

Values of K_t for each frequency probe of each transducer set, both measured and predicted via the heuristic form function and total normalised scattering

cross-section of the irregular shape Thorne & Meral (2008) model are compared in table 2.4. Values obtained via both particle size systems are given for reference. Similarly those obtained via the spherical Betteridge *et al.* (2008) model are listed in table 2.5. In general the measured values of K_t align well with predicted values, thus confirming the robustness of the Rice method approach (flowchart route 2) to calibration. Furthermore the utilisation of intermediate concentrations to perform rapid but equally precise calibrations is demonstrated.

Table 2.4: Comparison of measured ${K_t}^m$ with ${K_t}^t$ ($\mathrm{V\,m^{3/2}}$) calculated from Thorne & Meral (2008) equations, where σ denotes corresponding standard deviations.

Set	f_r	H16				H22			
	(MHz)	${K_t}^\mathrm{t}$	σ^t	${K_t}^\mathrm{m}$	σ^m	${K_t}^\mathrm{t}$	σ^t	${K_t}^\mathrm{m}$	σ^m
1	1	0.021	0.005	0.020	0.002	0.038	0.004	0.031	0.011
1	2	0.005	0.001	0.006	0.001	0.006	0.0003	0.006	0.0002
1	4	0.001	0.0001	0.001	0.0001	0.001	0.0001	0.001	0.00004
2	1	0.016	0.002	0.016	0.002	0.023	0.005	0.023	0.006
2	2	0.005	0.001	0.006	0.001	0.006	0.0001	0.006	0.0001
2	4	0.006	0.001	0.006	0.001	0.006	0.0001	0.006	0.0004
2	5	0.004	0.001	0.005	0.001	0.004	0.001	0.005	0.0003
3	1	0.018	0.005	0.017	0.001	0.015	0.0001	0.016	0.0004
3	2	0.006	0.001	0.006	0.001	0.006	0.0003	0.007	0.0001

$^\mathrm{t}$ calculated using (Thorne & Meral, 2008) equations.
$^\mathrm{m}$ measured K_t using K_s from Thorne & Meral (2008) equations and measured ξ from the Rice method (Rice *et al.*, 2014).

For further analysis, measured K_t values determined with both particle sizes are combined. The corresponding average transducer constants are given in table 2.6 with standard deviations. The measured values compare well with those supplied by the manufacturer. The average measured transducer constants listed in this table are hereby utilised in calculations in proceeding experiments.

Table 2.5: Comparison of measured ${K_t}^m$ with ${K_t}^t$ ($\mathrm{V\,m^{3/2}}$) calculated from Betteridge *et al.* (2008) equations, where σ denotes corresponding standard deviations.

Set	f_r	H16				H22			
	(MHz)	${K_t}^\mathrm{b}$	σ^b	${K_t}^\mathrm{m}$	σ^m	${K_t}^\mathrm{b}$	σ^b	${K_t}^\mathrm{m}$	σ^m
1	1	0.028	0.006	0.030	0.003	0.021	0.008	0.034	0.012
1	2	0.008	0.001	0.008	0.001	0.009	0.0002	0.007	0.0002
1	4	0.001	0.0002	0.001	0.0002	0.001	0.00001	0.001	0.00006
2	1	0.022	0.005	0.024	0.002	0.036	0.004	0.028	0.003
2	2	0.008	0.001	0.008	0.001	0.009	0.0004	0.007	0.0002
2	4	0.010	0.002	0.010	0.002	0.009	0.0002	0.007	0.0006
2	5	0.007	0.001	0.008	0.001	0.007	0.0002	0.006	0.0005
3	1	0.023	0.003	0.025	0.001	0.023	0.0001	0.028	0.012
3	2	0.009	0.001	0.009	0.001	0.009	0.0004	0.007	0.0001

[b] calculated using Betteridge *et al.* (2008) equations.
[m] measured K_t using K_s from Betteridge *et al.* (2008) equations and measured ξ from the Rice method (Rice *et al.*, 2014).

2.4.4 Backscattering Constant

The Rice method process outlined in the flowchart in figure 2.1, enables subsequent calculation of the backscattering constant K_s, from measured ξ and K_t. K_s has not previously been quantified in such a way. The backscattering constant obtained via the Rice method (Rice *et al.*, 2014) K_{s2}, is compared with that obtained via the Thorne method (Thorne & Hanes, 2002) K_{s1}, here.

K_{s2} estimated from the Rice sediment attenuation constant, and K_t from the irregular shape Thorne & Meral (2008) model are presented in figure 2.12, for Honite 22 set 2; 1,2,4 and 5 MHz figures A-D respectively. Figure 2.12 depicts the backscattering constant to be independent of transducer range. Profiles for all measured concentrations are shown, including the high concentrations up $76\,\mathrm{kg\,m^{-3}}$. The K_{s2} values are invariant with respect to concentration ranging 0.6-50 $\mathrm{kg\,m^{-3}}$, thus inferring independence from particle concentration. The backscattering constant is no longer linear with respect to transducer range at

Table 2.6: List of average measured K_t ($\mathrm{V\,m^{3/2}}$) values to be utilised going forward.

Set	f_r (MHz)	Average K_t[t]	σ^t	Average K_t[b]	σ^b	Manufacturer K_t
1	1	0.025	0.007	0.032	0.003	0.035
1	2	0.006	0.0005	0.008	0.001	0.010
1	4	0.001	0.000001	0.001	0.0002	0.002
2	1	0.020	0.005	0.026	0.002	
2	2	0.006	0.0004	0.008	0.001	
2	4	0.006	0.00002	0.008	0.002	
2	5	0.005	0.0001	0.007	0.001	
3	1	0.016	0.0004	0.027	0.002	
3	2	0.006	0.0004	0.008	0.001	

[t] average of measured K_t using K_s from Thorne & Meral (2008) equations and measured ξ from the Rice method (Rice *et al.*, 2014).
[b] average of measured K_t using K_s from Betteridge *et al.* (2008) equations and measured ξ from the Rice method (Rice *et al.*, 2014).

the highest concentration $76\,\mathrm{kg\,m^{-3}}$ due to very high attenuation and thus is disregarded from analysis. Furthermore, K_{s2} is highly over or under-estimated via the lowest concentration data at $0.1\,\mathrm{kg\,m^{-3}}$. As discussed previously, this is likely due to the very low scattering signal measured from the dilute concentration of small particles. The K_{s2} values obtained at the highest and lowest concentrations and any deviating profiles were discarded in further analysis. Upon comparison of figure 2.12 A-D, the scattering constant increases with increasing frequency, broadly following the theoretical expectations(Thorne *et al.*, 1993).

K_s estimated from Honite 16 set 2 2 MHz is presented in figure 2.13A-D for comparison. The backscatter constants of Honite 16 are markedly higher than thus, of Honite 22. This is primarily because, Honite 16 are relatively larger particles, therefore their scattering cross-sections are larger (refer to chapter 1 section 1.3.1.

Referring back to the two routes outlined in the flowchart in figure 2.1, both processes were initiated by the calculation of K_{s1} via the (Thorne & Meral, 2008)

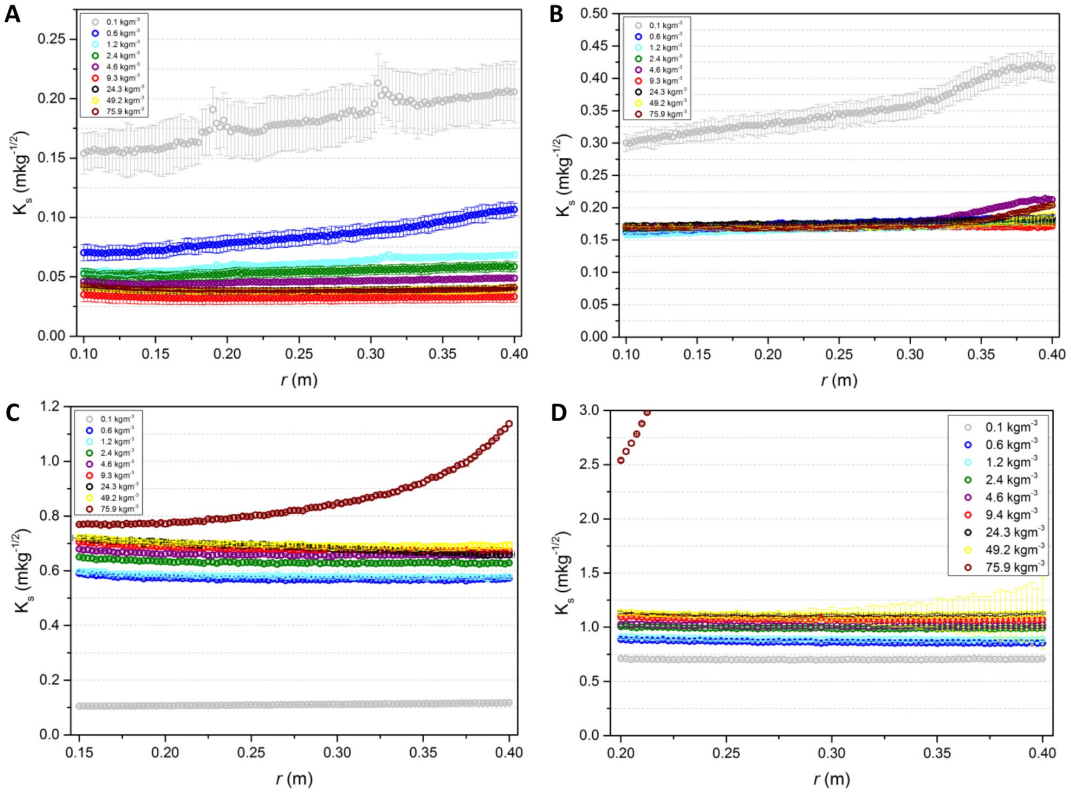

Figure 2.12: Distance averaged backscattering constants measured via each concentration of Honite 22 dispersions; (a) 1 MHz, (b) 2 MHz, (c) 4 MHz, and (d) 5 MHz.

and (Betteridge *et al.*, 2008) models. The final values of K_{s2} are compared with the initially calculated values of K_{s1} in table 2.7. The listed values correspond with the average generated per frequency over all transducer sets. Interestingly the measured K_{s2} values from both models compare well with the predicted K_{s1} from the spherical Betteridge *et al.* (2008) model, but not as well with the irregular shape Thorne & Meral (2008) model. To elaborate on this, the form function was calculated for each tabulated value and is presented as measured data points against predicted solid lines, against *ka* in figure 2.14. Notably, the form function has not previously been assessed in such a manner. The data depict that the measured values of the form function are systematically higher than those calcu-

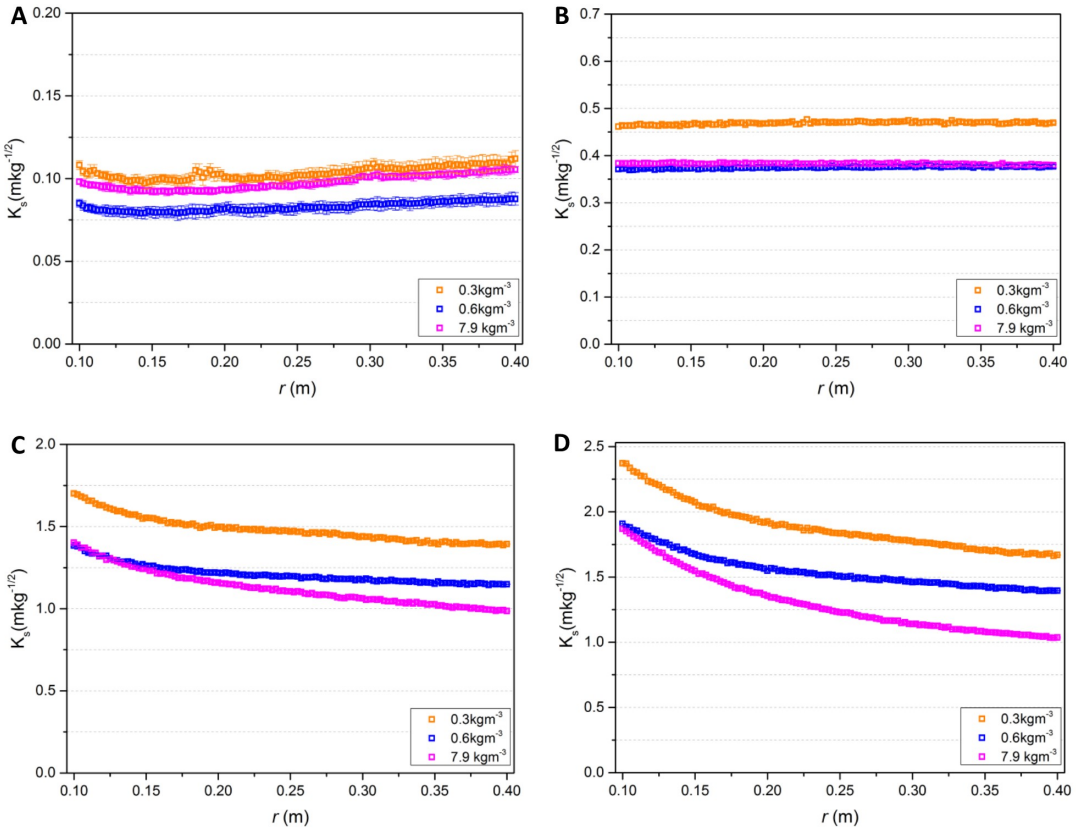

Figure 2.13: Distance averaged backscattering constants measured via each concentration of Honite 16 dispersions; (a) 1 MHz, (b) 2 MHz, (c) 4 MHz, and (d) 5 MHz.

lated via the irregular particle shape Thorne & Meral (2008) model. Hence the K_t values obtained via this model in table 2.6 are systematically lower. Indeed the figure 2.14 depicts that the Betteridge *et al.* (2008) model provides a better fit for the spherical Honite particles.

2.5 Summary

Chapter 2 summarised the general methodological approach taken towards experimentation and data analysis. The recently published Rice method (Rice *et al.*,

Table 2.7: Comparison of calculated K_{s1} and measured K_{s2} via both sets of heuristic equations, ($\mathrm{m\,kg^{-1/2}}$).

Particle	f_r (MHz)	Measured $K_{s2}{}^{b}$	σ	Calculated $K_{s1}{}^{b}$	Measured $K_{s2}{}^{t}$	σ	Calculated $K_{s1}{}^{t}$
H16	1	0.08	0.004	0.10	0.11	0.002	0.06
	2	0.31	0.003	0.38	0.41	0.004	0.22
	4	1.00	0.002	1.19	1.34	0.003	0.58
	5	1.20	-	1.54	1.62	-	0.69
H22	1	0.03	0.004	0.04	0.04	0.002	0.02
	2	0.13	0.001	0.15	0.17	0.002	0.09
	4	0.48	0.005	0.55	0.65	0.007	0.32
	5	0.70	-	0.83	0.99	-	0.45

[b] calculated using Betteridge *et al.* (2008) equations.
[t] calculated using Thorne & Meral (2008) equation.

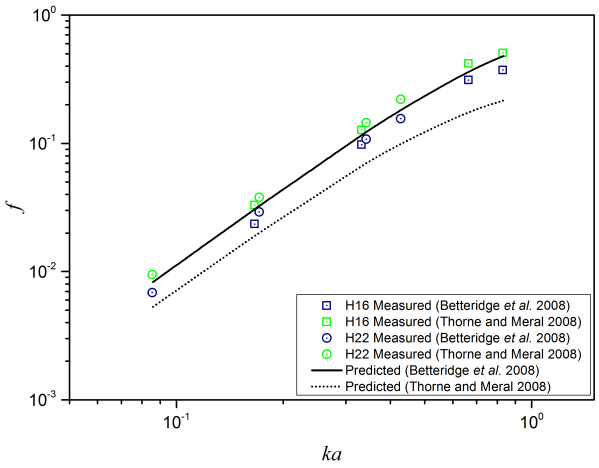

Figure 2.14: Comparison of the calculated and predicted form function versus wavenumber for Honite 16 and 22.

2014) was utilised in a larger scale suspension system (0.5 m rather than 0.05 m scale) to derive the particle specific sediment attenuation constant ξ. Measured values compared well with literature (Rice *et al.*, 2014). The Rice method de-

termines the sediment attenuation coefficient from a measured direct linear fit of $\frac{dG}{dr}$ against M. The values compared well with those determined from the empirical polynomial equation of four orders for χ. Hence the robustness of this simple method was demonstrated with respect to using a complex expression for calculation.

Secondly focus was placed on establishing a simple robust calibration protocol for any acoustic backscattering system which is comparable with prescribed published protocol (Betteridge *et al.*, 2008; Thorne & Hanes, 2002). Each transducer from each set was successfully calibrated, where derived values of K_t compared well with those from the manufacturer. Importantly K_t values derived from ξ measured from the independent Rice method and the empirical Thorne equations compared well, thus demonstrating the robustness of the Rice method. Furthermore, the results were broadly consistent at intermediate concentrations, but data variation was enhanced for low concentrations. The use of higher than typically prescribed concentrations was demonstrated and the duration of calibration was reduced whilst maintaining accuracy. Hence a suitable, rapid, robust calibration protocol was established.

The successful derivation of K_t also enabled its decoupling from the system constant of $K_t K_s$, to extract the particle specific backscattering constant K_s. Values of K_s obtained from the measured ξ and K_t here, compared well with values of K_s calculated from the Thorne & Meral (2008) equations. Now that K_t is known, it is possible to determine K_s for any arbitrary particle. This is key because K_s is typically calculated using the empirical form function equations. These empirical equations have only been developed for spherical glass particles and irregularly shaped sand. However in the case where K_t is predetermined from calibration with spherical glass particles, all that remains to determine K_s for any arbitrary particle is the particle specific ξ. This can be determined for any particle without requirement of an empirical equation for the total normalised scattering cross-section via the Rice method.

The experiments conducted in chapter 2 utilised smaller than typical particle sizes. In doing so, experiments were performed in the low ka range only (ka<1). There is not much data published within this region and hence there was little data contributing to the development of the heuristic equations for χ and

f. Although irregular particles are assumed to scatter like spheres at $ka<1$, it was found that the heuristic model for irregular particles began diverging from the spherical model at around $ka\sim0.4$. Indeed a better understanding of what happens to the form function and total normalised scattering cross-section in the low ka range, since the the particles of interest in this research are generally smaller in size than typical coastal applications, therefore further focus is placed on measurements at $ka<1$.

Chapter 3

Characterisation of a dynamic inorganic dispersion, in an industrial scale impinging jet ballast tank

Chapter 3 is presented in two parts. Initially the laboratory calibration of a barytes (barium sulfate) suspension is reported. The backscatter response of this inorganic mineral is investigated and its acoustic properties are established for the first time here. Specifically the Rice method quantifies the particle specific backscattering and attenuation constants. Importantly, this extracts the relationship between measured backscatter and particle concentration, such that it may be used as a reference to characterise concentration from backscatter measurements. This was proven in an independent investigation of a settling barytes suspension. The second part exploits this new knowledge, to characterise a dynamic barytes dispersion within an industrial scale tank, which utilises impinging jet ballasts to resuspend settled sediment. In this novel application, invaluable information is gained with respect to how sediment erosion, resuspension and resettling dynamics correspond with jet operating regimes. The capability to characterise, large scale complex dispersion systems, for predictive modelling and operational optimisation, is highlighted.

3.1 Introduction

Establishing ABS application in industrial dispersions of any arbitrary particle type is the primary goal of this research. Application in this context is about providing a route to extract very detailed knowledge on collective dispersion dynamics, and linking these with system operations. This includes being able to monitor settling behaviour, concentration fluxes, settled bed depths and locations, as well as the positioning of any internal tank structures, for example, a moving rake within a thickener tank. Therefore it was fitting to trial deployment in a corresponding scenario.

To keep in line with the nuclear waste characterisation theme, the ABS was trialled in a non-active Highly Active Storage Tank (HAST). HASTs, pictured in figure 3.1A-C, are intermediary storage vats for the highly active liquor waste stream which arises from spent nuclear fuel reprocessing at Sellafield Ltd (Cumbria, UK). They comprise of cooling coils to remove heat generated from radioactive decay, impinging jet ballasts to resuspend any sedimented particulates, and air-lifts to mobilise particles and homogenise the suspension (Hunter *et al.*, 2013; Paul *et al.*, 2013). From an operational perspective, it is preferential for the particulates to remain in suspension, to prevent the formation of radioactive sediment beds on the base causing hotspots. HASTs are very complex systems with respect to both the physical structuring and comprising dispersions. Additional monitoring difficulty is encountered due to the highly radioactivity contents. Therefore, it was not possible to deploy the ABS in an actual active HAST at this stage. In any case, non-active trials are usually conducted prior to deployment in radioactive systems. Indeed, this type of approach also enables gathering of information such that the behaviour of more complex, inaccessible systems can be modelled for optimisation and decommissioning purposes, without requirement of any active deployment (Hunter *et al.*, 2013). Such challenges are widely reminiscent of nuclear industries around the world. The Hanford Site (Washington State, USA) for example, is the largest facility in the USA, housing 53 million US gallons of highly radioactive waste in 177 underground storage tanks. A large effort of the clean-up process there, incorporates regular tank monitoring, mobilisation of

wastes in tanks to prevent radioactive hotspots, and the modelling of system dynamics in non-active rigs to aid decommissioning (Powell *et al.*, 1997). Although the focus here is on nuclear application, as mentioned in chapter 1 section 1.1, the possible range of applications where dispersions are processed in complex vat systems, is vast.

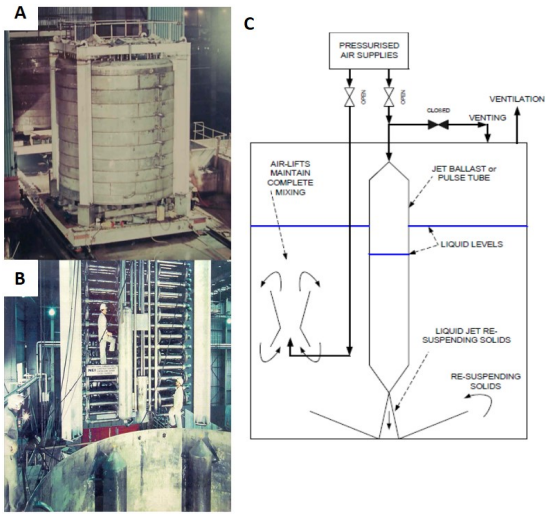

Figure 3.1: (a) HAST, (b) cooling coils close-up prior to insertion into adjacent HAST, and (c) schematic of jet ballast operation (McArthur *et al.*, 2005).

Large scale non-active experiments in the nuclear industry utilise nuclear test materials; cheap inorganic minerals which comprise some physical properties corresponding with nuclear sludges, as opposed to expensive analogue simulants. Barium sulfate (barytes), calcium carbonate (Calcite), titanium dioxide (Titania) and magnesium hydroxide are typically employed (Hunter *et al.*, 2012c, 2013; Paul *et al.*, 2013). Zirconium molybdate and caesium phosphomolybdate are the primary known constituents in HAST dispersions. Both components exhibit high densities (3000-4000 $\mathrm{kg\,m^{-3}}$). Accordingly, barytes, which is also highly dense (>4000 $\mathrm{kg\,m^{-3}}$), was selected to model a worse case settling scenario. barytes is also a common mineral in many manufacturing applications, particularly in pigments (Kresse *et al.*, 2000).

To enable industrial characterisation, a laboratory scale calibration was required to establish the relationship between measured signal and concentration.

This information was extracted via the Rice analysis method, the procedure of which was discussed in chapter 1 section 1.4.3. This approach is thought to be superior to the Hunter *et al.* (2012a) direct attenuation correlation technique, in less attenuating dispersions. As discussed in chapter 1 section 1.4.2, the empirical method was successfully demonstrated for highly attenuating, aggregated colloidal Titania dispersions (Bux *et al.*, 2015), however it was presumed that the larger, non-aggregated, barytes would perhaps be a less attenuating mineral. The Rice method also enabled quantification of the particle specific backscattering and attenuation constants. These have not previously been reported for any inorganic minerals.

The structure of this chapter is such that the laboratory calibration of barytes is initially reported, where the backscatter response, acoustic properties and reference calibration relationship are discussed. Since settling dynamics in the HAST is the key aspect of experimental interest, the settling dynamics of barytes dispersions were first investigated on a laboratory scale for comparative and predictive purposes. This involved classical measuring cylinder sedimentation tests, and settling tests profiled via the ABS. Importantly, the calibration work reported here, utilises the Rice method in dispersions with particles which are an order of magnitude smaller than 100 µm, and in larger depths than pipe-flows of a few centimetres. The second part of the chapter reports on ABS measurement in a non-active industrial tank under varying operational regimes, and subsequent concentration characterisation via the reference calibration relationship. In this novel application, very detailed information was obtained about sediment erosion success with respect to jet operation, levels of sediment redispersion throughout the tank, including the influence of neighbouring jets, and the impact of air-lift operation on the resettling kinetics of the dispersed sediment. This information proved to be invaluable in illustrating the actual behaviour of the dispersion on a large scale, and importantly, with respect to the applied operating cycle. Hence, mediating optimisation and enabling modelling and design of future decommissioning processes. Such information has not previously been extracted in such a way, and is not easily attained *in situ* via other means.

3.2 Laboratory Calibration of barytes

The experimental procedures and results of the calibration and settling tests are reported in this section.

3.2.1 Experimental Methods

Materials Selection

barytes (RBH Ltd, UK) was utilised in both laboratory and industrial experiments. It was selected for experimentation because it is a cheap test material, which simulates the high density properties of caesium phosphomolybdate (CPM) and zirconium molybdate (ZM), the primary radioactive constituents in HAST waste liquors. Cheap test materials are preferable in large scale trials, since analogue simulants; non-radioactive CPM and ZM in this case, are not readily available and are too costly (Paul *et al.*, 2013). The particle size distribution, shape and density of barytes were characterised and are reported here. Size distribution was obtained via a Malvern Mastersizer 2000, a dynamic light scattering technique as described in chapter 2 section 2.3. Three individual sample dispersions were prepared and measured three times each. The resulting average distribution is presented in figure 3.2. The distribution is bimodal with a primary peak around 10 µm and a small fraction of fines around 1 µm. The resulting D_{50} is 7.8 µm and Sauter diameter $D_{4/3}$ is 9.9 µm. Note however there is a very minor fraction of larger particles in the 100 µm region.

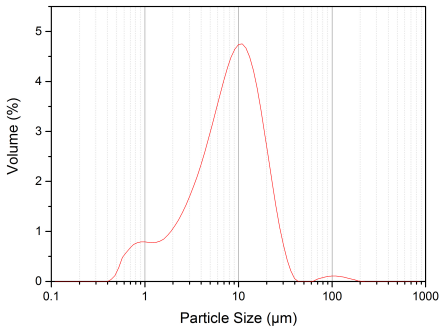

Figure 3.2: barytes size distribution

Particle shape and size were characterised via the FEGSEM SEM (Carl Zeiss Ltd., UK) as described in chapter 2 section 2.3. The dry powder was placed onto carbon coated stubs and coated in platinum. Images collected at x 2,500 and x 10,000 magnifications are presented in figure 3.3. The images depict jagged shaped barytes crystals. This is interesting from an acoustic perspective because shape influences backscatter response. In traditional ABS application, the scattering of natural sediments are modelled assuming spherical shape. Backscattering of non-spherical particles may be influenced by suspended particle orientation and there may be enhanced inter particle scattering events attenuating the backscatter response (Moore *et al.*, 2013a). The images in figure 3.3 also depict a bimodal size distribution with the majority of particles within the 10 µm region alongside a few fines. This aligns with the measured size distribution results in figure 3.2.

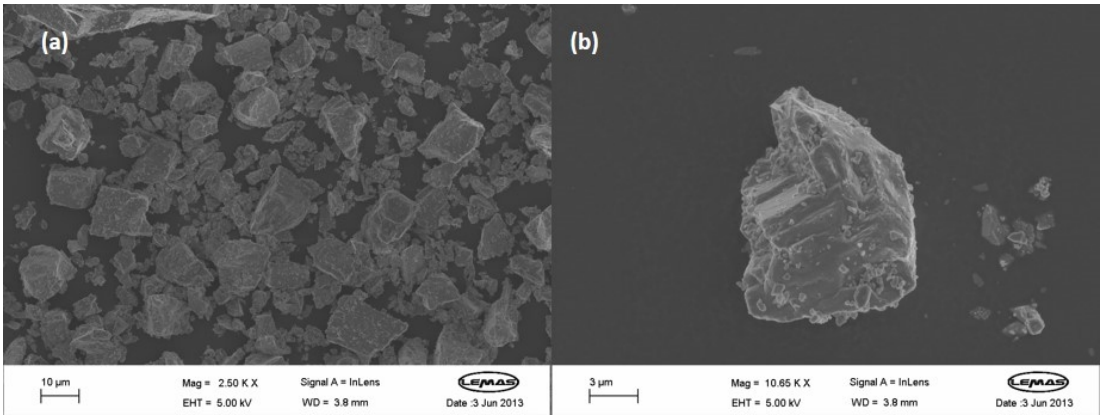

Figure 3.3: SEM micrographs of barytes at (a) x 2,500 and (b) x 10,000 magnification.

Since particle density was a major contributor to the choice of material, barytes density was measured via a Micrometrics Accu-Pyc 1330 helium pycnometer (Micrometrics Instrument Corporation, USA). Here a dry sample of material was weighed and emplaced in the instrument. Particle density was obtained by measuring helium displacement in a sample tube (of known volume), both with the sample present and without. Three individual samples were prepared and

measured three times each. The resulting density was 4418 kg m^{-3}, close to the expected value for barytes 4490 kg m^{-3} (Haynes, 2014).

Table 3.1: Comparison of physical particle properties

Particle	Size D_{50} (μm)	Shape	Density (kg m^{-3})
barytes	7.8	Jagged	4418
Caesium Phosphomolybdate[a]	0.7	Spheroidal	3820
Zirconium Molybdate[a]	2.3	Cuboidal	3410

[a] Data from Paul *et al.* (2013).

The measured physical properties of barytes are presented in table 3.1 alongside those of zirconium molybdate and caesium phosphomolybdate for comparative purposes. Although barytes is somewhat larger in size, its density is comparable, albeit slighter greater, than the primary radioactive particles in the HAST waste liquors. This is important because particle density is a significant influencer with respect to settling dynamics. Therefore, barytes investigations provide information on dispersion behaviour in the tank, in a worst case settling scenario. barytes is also somewhat representative of the non-spherical shape characteristic of zirconium molybdate.

Calibration Methodology

The calibration experiments were conducted in the tank set-up described in the methodology (chapter 2 section 2.2). Specifically, the waterline was set at 60 cm, and a mixing impeller running at 1640 rpm was positioned off-centre at 10 cm from the base. A homogeneity check was conducted prior to acoustic experimentation since uniform particulate dispersion is integral to drawing an accurate relationship between backscatter attenuation and concentration (Moore *et al.*, 2013a). Specifically a barytes dispersion with a bulk concentration of ∼1.2 vol% (5wt%) was prepared and continuously mixed at 1640 rpm. 3 x 50 ml samples were extracted via syringe at four designated column depths from the base. The samples were weighed wet, dried in an oven at 55 °C for 24 hours and weighed dry. The dry/wet ratios enabled calculation of suspension concentration at each depth in terms of wt%. These values were converted to vol% using the measured

density value of 4418 kg m^{-3}. The results of the homogeneity test are depicted in figure 3.4. These data demonstrate that the samples taken at each depth are within the region of the initial concentration (depicted as the dashed line) and vary by ± 0.09 vol%, indicating that the off-centred impeller was successful at suspending the dense barytes particles homogeneously throughout.

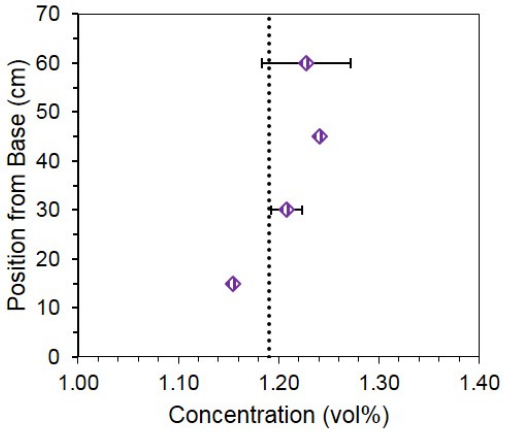

Figure 3.4: Graph depicting suspension homogeneity in mixing tank.

For the acoustic calibration, 2 x 1 MHz and 2 x 2 MHz AQUAscat 1000 ABS transducers (Aquatec Group Ltd, UK) were submerged 5 cm below the waterline. The suspension concentration was increased in increments as follows; 0.06, 0.12, 0.23, 0.46, 0.93 and 1.42 vol% (i.e. ranging from 0.25 to 6 wt%). A minimum of 10 minutes was allowed between sediment addition and ABS measurement to enable thorough mixing and degassing. Air bubbles were brushed from the transducers front face prior to ABS measurement to prevent deviation of the signal via acoustic propagation in air (Richards & Leighton, 2001). The transducers profiled the suspensions for a duration of 5 minutes, pulsing in sequence at a rate of 32 Hz, storing 1 profile per second in 2.5 mm distance bins. The pulse frequency rate was sufficient to enable the acoustic pulse to travel back to the transducer before the emission of the subsequent pulse. Three measurement runs were conducted per concentration and an average backscatter intensity was ascertained per concentration.

Settling Test Methodology

The settling tests were conducted within the tank set-up previously seen in figure 2.2, although with minor alterations; the waterline was set at 40 cm and mixing impeller speed at 1200 rpm. The settling of two dispersion concentrations was investigated; 0.7 vol% (3 wt%) to match the nominal concentration in the industrial experiments and 1.4 vol% (6 wt%). Due to enhanced attenuation at the highest concentration, the transducers were positioned 15 cm below the waterline to enable profiling within the sediment bed region. The suspension temperature was 24.5 °C. The dispersions were mixed for 10 minutes post sediment addition to ensure homogeneity, after which the mixer was turned off and the settling dispersions were profiled via 1 x 1 MHz and 3 x 2 MHz ABS probes for a duration of 10 minutes. Three experimental runs were conducted per concentration with 10 minute intervals allowing for sediment resuspension and re-homogenisation.

In addition a series of *ex situ* sedimentation tests were conducted in 1 L measuring cylinders to validate the settling data obtained via the ABS. Tests were conducted for the following concentrations; 0.46, 0.69, 0.93 and 1.42 vol% (corresponding with 2, 3, 4 and 6 wt% respectively). Suspension temperature was 24.5 °C. It was not possible to visually discern a distinct delineation of a clarified supernatant and settling cloud interface, due to Brownian diffusion of a large concentration of fine particles. Consequently, only the position of the sediment bed interface was recorded with time. Four tests were conducted per concentration and collated to provide an average per concentration. Lower concentrations were not investigated since the sediment bed interface was too diffuse to discern by eye, due to the Brownian motion of the particles .

3.2.2 Results & Discussion

Calibration Results

The calibration results are reported here. The acoustic response of homogeneous barytes suspensions ranging 0.06 - 1.42 vol% is presented in figure 3.5A-B for 1 and 2 MHz respectively. The measured backscatter intensity in decibels is depicted with respect to distance from the transducer. Figure 3.5C-E presents

the backscatter response obtained via the two probes of matching frequencies, at three different concentration levels. These only exhibit minor variations between probes. Therefore, the concentration profiles depicted in A-B, represent the average intensity from two probes.

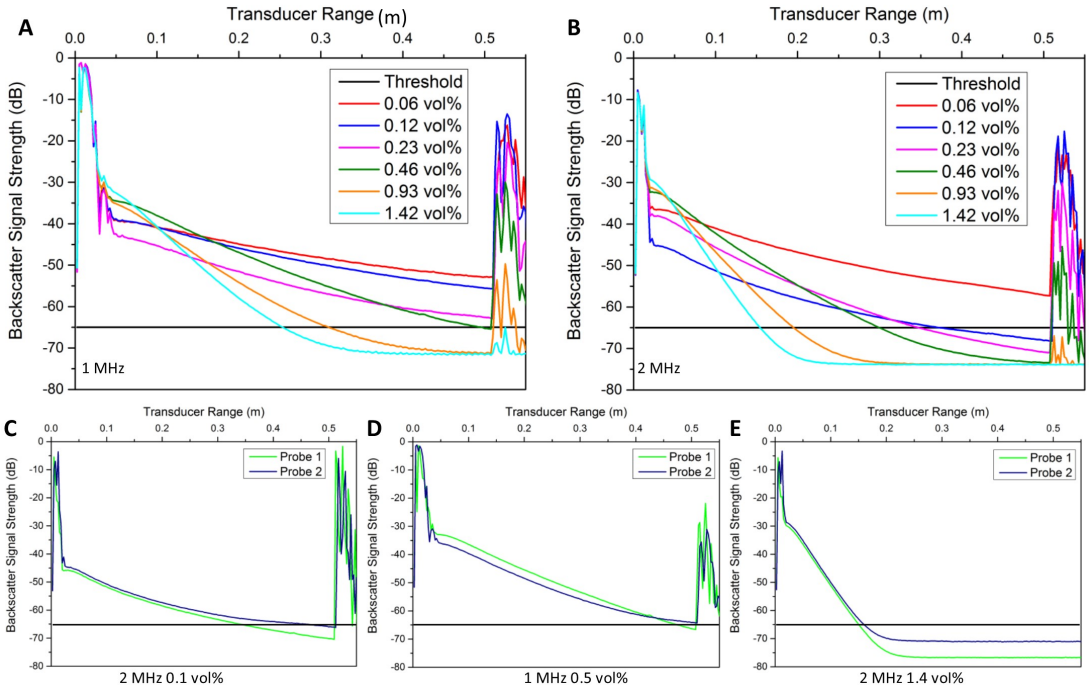

Figure 3.5: Average backscatter profiles at (a) 1 MHz and (b) 2 MHz. Backscatter profiles comparing the signal from two probes with identical frequency at (c) 2 MHz 0.1 vol%, (d) 1 MHz 0.5 vol% and (e) 2 MHz 1.4 vol%.

All backscatter profiles in figure 3.5A-B display the typical near-field, far-field, frequency and concentration related characteristics of attenuating dispersions, as discussed in chapter 2 section 2.4.1. The peak at 50 cm denotes the tank base position relative to the transducers. The progressive steepening of the gradient with increasing concentration is a key profile feature. Since the gradient quantifies the attenuation of backscatter intensity, this can be related directly with concentration when the profiles exhibit a linear extinction. Since the profiles appear to exhibit approximately linear decay, the direct linear gradient of each

concentration was analysed in the first instance (akin to analysis conducted by Bux *et al.* (2015); Hunter *et al.* (2012a)). Note, data in the near-field, and data beyond the instrument's threshold, were discarded from analysis. The resulting relationship between attenuation and concentration is presented in figure 3.6A. Therefore, this relationship can be utilised as a reference to quantify concentration from direct measurement of the attenuation of a backscatter profile. The R-squared fit of the corresponding profiles is also presented, in figure 3.6B. This latter figure indicates that the profiles obtained via both frequencies, are highly linear at concentrations > 0.5 vol%. They are however less linear at the lower concentrations.

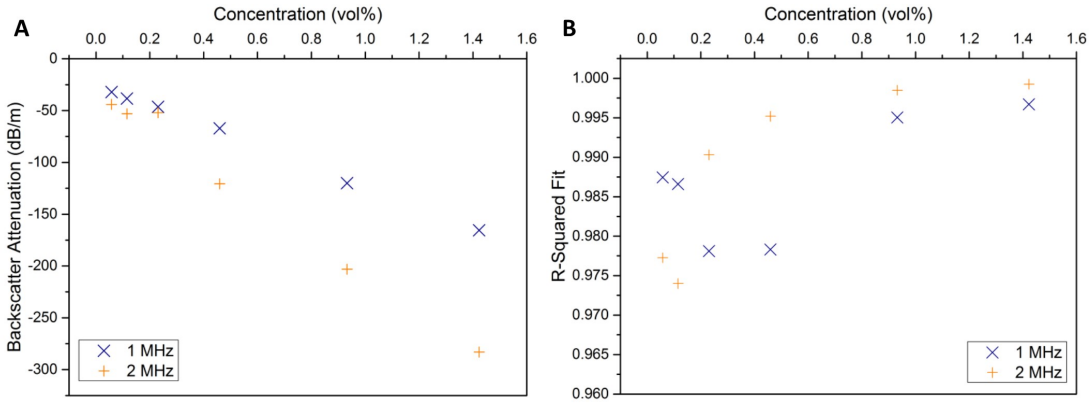

Figure 3.6: (a) Attenuation - concentration relationship from linear analysis and (b) corresponding R-squared linear fit of data.

To investigate further, additional analysis approaches were taken. Firstly a tangential analysis technique is discussed (Hunter *et al.*, 2012a), where the interpolated differential (change in backscatter strength over consecutive distance points) is taken at specific depths, (refer to chapter 1 section 1.4.2). This enabled assessment of the attenuation at several depths rather than assuming a linear attenuation fit over the entire profile. Note that the interpolated differential here was determined over a series of 10 consecutive distance points per selected depth, due to substantial measurement noise. The resulting estimated change of tangential attenuation with concentration is presented in figure 3.7A-B at several

depths for 1 and 2 MHz respectively. Here, both frequencies exhibit an approximately linear trend between tangential attenuation and concentration. Although the absolute attenuation values vary between depths, the respective gradients of attenuation are approximately the same. Gradient changes in concentration are independent of depth. Consequently, the interpolated differential slope can also be used as a reference relationship to determine concentration changes at any depth point within a dispersion.

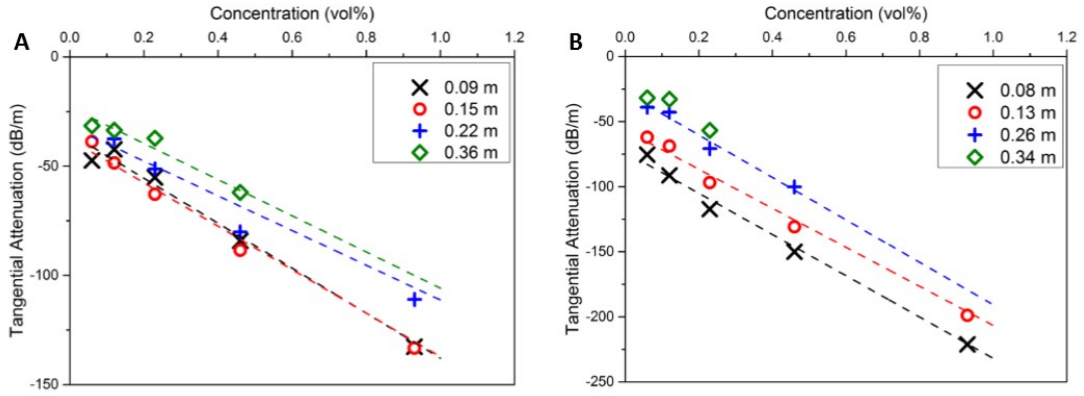

Figure 3.7: Tangential attenuation - concentration relationship from interpolated differential analysis at various depths for (a) 1 MHz and (b) 2 MHz.

Hunter *et al.* (2012a) demonstrated this type of assessment via spherical glass particle suspensions with D_{50} 44 µm. These larger spherical particles are stronger scatterers than barytes and hence the corresponding backscatter profiles attenuate over longer distances, so the acoustic wave penetrates and returns a backscatter signal over further distances. In that case, Hunter *et al.* (2012a) were able to measure data over a metre length scale at similar concentrations to that of barytes. Here only half a metre scale was measurable at high concentrations. So in figure 3.7 it was only possible to determine the tangential attenuation - concentration relationship for depths close to the transducer, due to rapid signal cut-off at shorter depths. Although the differential slope method is preferential to the linear slope method in this case, the tangential method may not yield the most appropriate reference relationship for concentration.

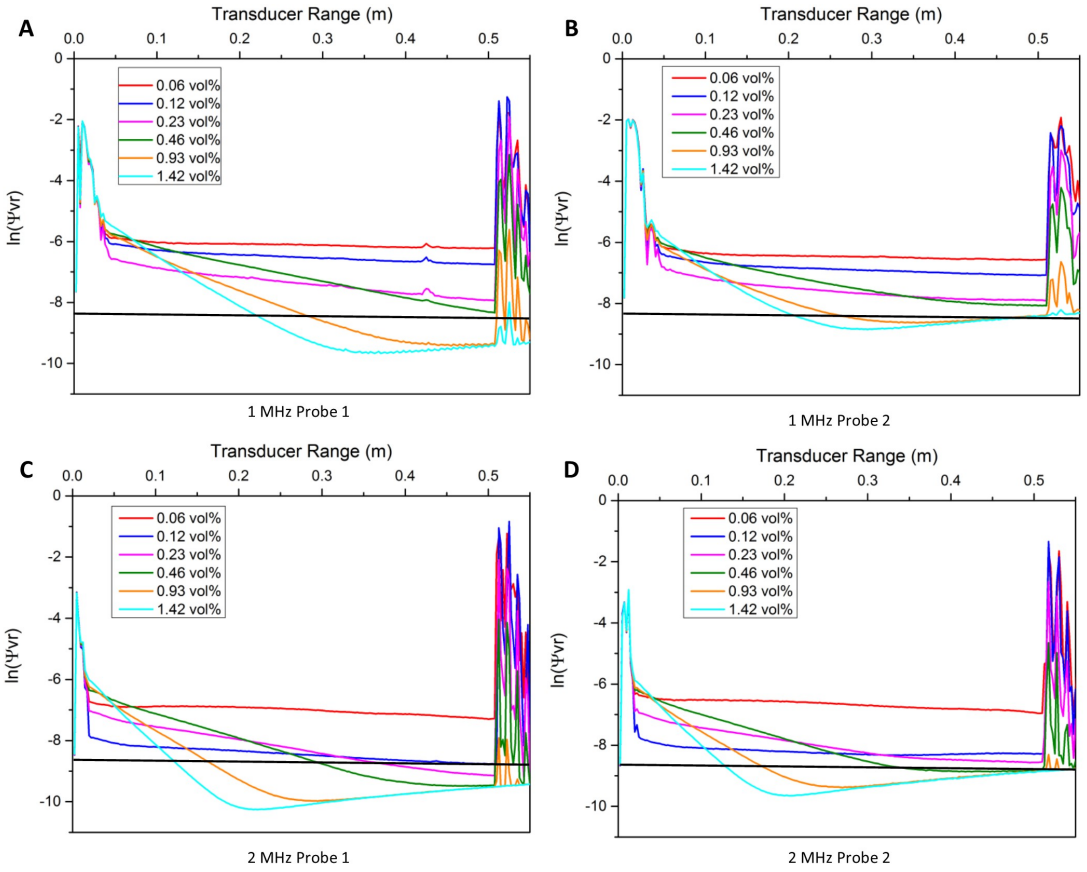

Figure 3.8: Backscatter profiles in terms of ln(ψVr) against r for (a) 1 MHz probe 1, (b) 1 MHz probe 2, (c) 2 MHz probe 1 and (d) 2 MHz probe 2.

The Rice method, which takes into account the logarithmic type backscatter decay exhibited by less attenuating particles (Rice *et al.*, 2014), was then utilised (refer to chapter 1 section 1.4.3). Specifically the measured backscattered voltage was plotted with G=ln(ψVr) with respect to transducer range, for each concentration as presented in figure 3.8. Note that profiles for both sets of probes of each frequency are shown independently, since these data are subsequently used to determine attenuation and backscattering constants for barytes, the calculation of which is probe specific due to the incorporation of the transducer constant (chapter 1 equation 1.4). The solid black line signal threshold lines at -65 dB, correspond with -8.2 G and -8.5 G for 1 and 2 MHz respectively.

The natural log backscatter profiles in figure 3.8 depict a linear backscatter decay in the far-field region and a peak signifying the tank base at 50 cm. Notably at the two highest concentrations, linearity is no longer observed at around -8.2 G - -8.5 G, which corresponds with the signal threshold cut-off region around −65 dB. Also in the case of 2 MHz at the lowest concentrations 0.06 - 0.12 vol%, a slight increase in G with depth is observed rather than a decay, due to the increase in particle scatterers increasing intensity initially. Unfortunately it appears that there is a minor interference around 0.42 cm for 1 MHz probe 1, which is likely due to the positioning of the probes during those particular measurements. Therefore data analysis is only conducted up to this point for the corresponding profiles.

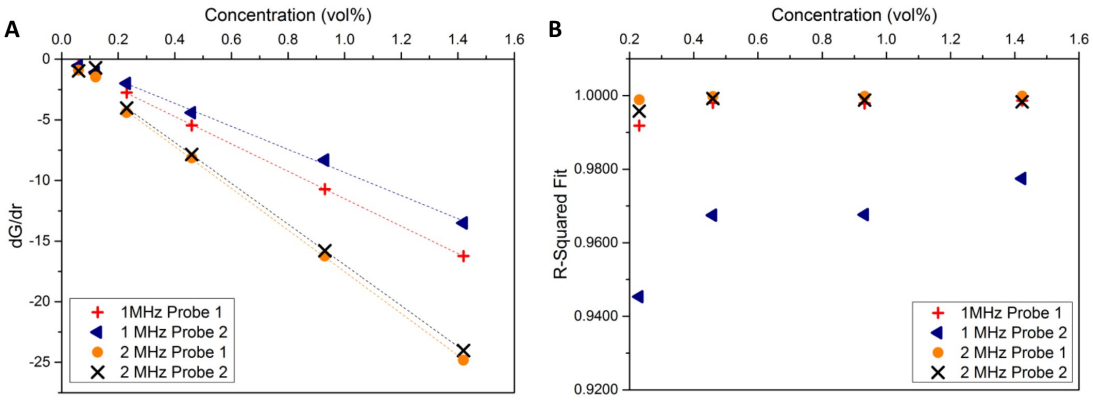

Figure 3.9: Calibration reference relationship (a) $\frac{dG}{dr}$ with respect to concentration and (b) corresponding R-squared linear fit of data.

An important feature of the logarithmic profiles in figure 3.8 is that the gradient of the G function steepens with increasing concentration, akin to those in the decibel profiles in figure 3.5. The resulting gradient of attenuation of each logarithmic concentration profile is presented in figure 3.9A as $\frac{dG}{dr}$ with respect to concentration. These data display a linear trend between the two variables and thus highlight that this relationship can be utilised to determine concentration where the backscatter profiles are transformed to G against transducer range. Interestingly the two 1 MHz probes exhibit a minor variation. Referring back to the corresponding G profiles in figure 3.8A, there is a very minor peak at approximately 45 cm. This is likely due to wall scattering owing to probe placement.

This is the likely cause for data variation in this instance. The R-squared fits of the corresponding gradients are depicted in figure 3.9B. They portray improved R-squared fits compared with the linear and tangential methods in figures 3.6 and 3.7 respectively. Hence the correlation between $\frac{dG}{dr}$ and concentration is utilised as the reference relationship in subsequent experiments.

Table 3.2: Measured sediment attenuation and backscatter constants for barytes

Frequency (MHz)	Probe	ξ ($\mathrm{kg^{-1}\,m^{-2}}$)	K_s ($\mathrm{m\,kg^{-1/2}}$)
1	1	0.1254	0.0250
1	2	0.1055	0.0237
2	1	0.1910	0.0531
2	2	0.1867	0.0606

The calibration data were utilised alongside the probe transducer constants (calculated in chapter 2 section 2.4.3), to determine the backscatter and attenuation constants of barytes via each probe. These values are summarised in table 3.2. Both 2 MHz probes generated attenuation constants approximately $0.189 \pm 0.002 \mathrm{kg^{-1}\,m^{-2}}$. The value generated by the second 1 MHz probe is slightly lower than that of the first probe. However the R-squared analysis of the former probe exhibited less linearity in the latter (refer to figure 3.9B), therefore an attenuation constant ξ of $0.115 \pm 0.010 \mathrm{kg^{-1}\,m^{-2}}$ is perhaps more realistic in the case of 1 MHz. The average backscattering constants K_s from both probes are $0.024 \pm 0.0006 \mathrm{m\,kg^{-1/2}}$ and $0.057 \pm 0.005 \mathrm{m\,kg^{-1/2}}$ for 1 and 2 MHz respectively.

Settling Test Results

The results of the classical settling tests conducted in measuring cylinders are initially discussed. Figure 3.10 portrays sediment bed evolution at four volume fractions; 0.5, 0.7, 0.9 and 1.4 vol%. Note that at these concentration levels, it was not possible to discern a clear demarcation between a clarified supernatant and settling suspension. The dispersions remained fairly turbid with colloidal size particles remaining in suspension, with the exception of the highest concentration where clear zonal hindered settling was observed. All experiments exhibited rapid deposition of sediment at the base however, hence it was possible to measure

sediment bed height as a function of time. All four volume fractions in figure 3.10 depict identical bed formation behaviour, whereby the bed height increases in a linear fashion with time. After bulk particle deposition ceases (within 2 minutes), the bed undergoes compression due to the hydrostatic load of the water. Hence compression is more marked at higher volume fractions as witnessed.

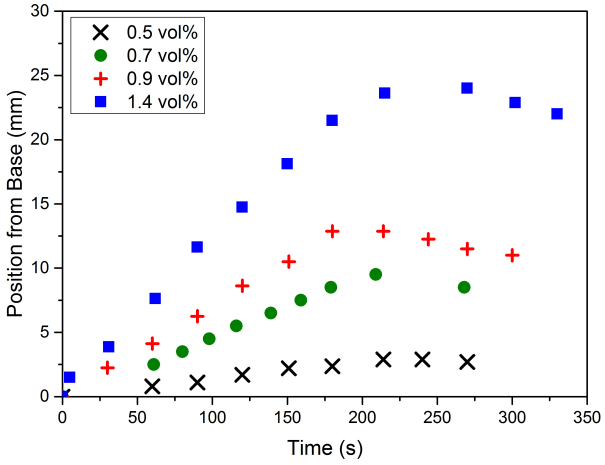

Figure 3.10: Settling bed formation at various concentrations via measuring cylinder settling tests.

The results of the settling dispersions profiled via the ABS are reported here. Figure 3.11A-C displays profiles at selected time intervals in minutes, where a 0.7 vol% dispersion was profiled via 2 MHz. Note the time profiles have been presented in a series of three graphs for ease of observation. To begin with, the intense narrow peak depicted in profile T(0) at 28.25 cm, denotes the column base position relative to the transducer. In subsequent time profiles, the peak recedes in intensity and shifts towards the transducer. This shift is indicative of a peak corresponding with a layer of sediment that has deposited at the base. The bed height reaches a maximum depth of 0.75 cm, i.e. at position 27.50 cm, by T(3.5). Another broad peak is also observed close to the transducer. It forms at a 3 cm transducer range at T(1.5), and shifts towards the column base in successive profiles, up to and including T(4). This feature is indicative of the demarcation of a diffuse scattering plane, corresponding with a moving clarified

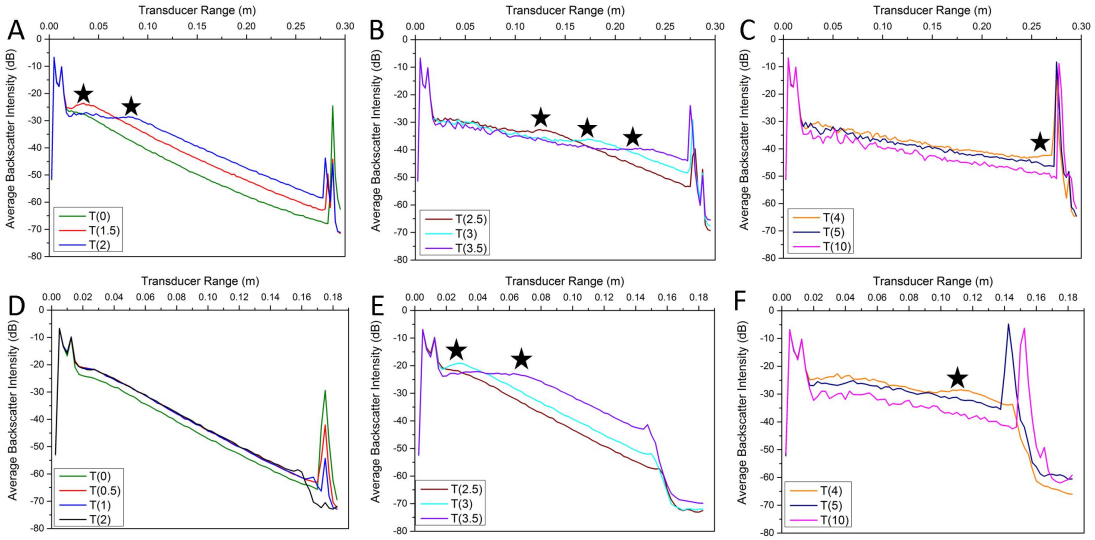

Figure 3.11: Time-averaged only backscatter profiles at selected times during settling for (a-c) 2 MHz 0.7 vol% and (d-f) 2 MHz 1.4 vol%. All legend times given in minutes T(min), and asterisks indicate location of the settling front.

supernatant-settling front interface. Indeed the gradient of the profiles between the settling interface peak and the base peak, is steepened relative to that in the clarified region, indicating regions of higher concentration within the settling zones. Notably, the sediment bed height does not alter after 3.5 minutes (210 s), although settling is not finalised until 5 minutes (300 s). This is an interesting feature which is linked directly to the bidisperse nature of this dense particle system. Essentially, this observation suggests that the large dense particles deposit rapidly, followed by a slower calcification of fine particles. This observation would have marked implications for the modelling of barytes settling behaviour in the industrial non-active tank. In order to clarify the type of settling behaviour, the measured positions of the settling interface and sediment bed interface were extracted from the ABS data and plotted as a function of time, for 0.7 vol% in figure 3.13 A. Specifically, the settling front location measurements were taken at the base of each peak, i.e. the point at which the decreasing backscatter strength starts to increase. The resulting sedimentation curve verify a zonal hindered settling front, which markedly slows down after 210 s. The latter which corre-

sponds with the hindered settling of finer particulates. These observations align with Balastre *et al.* (2002), whom reported that a sharp demarcation between the supernatant and settling particles zone, and thus hindered settling behaviour is typically observed at concentrations from 1 vol%. The ABS was far more sensitive to this demarcation, enabling its measurement, compared with observations by eye. Although, it was difficult to discern the exact locations of the diffuse settling front and sediment bed boundaries at 4.5 minutes due to resolution limitations, hence this data was not incorporated in figure 3.13.

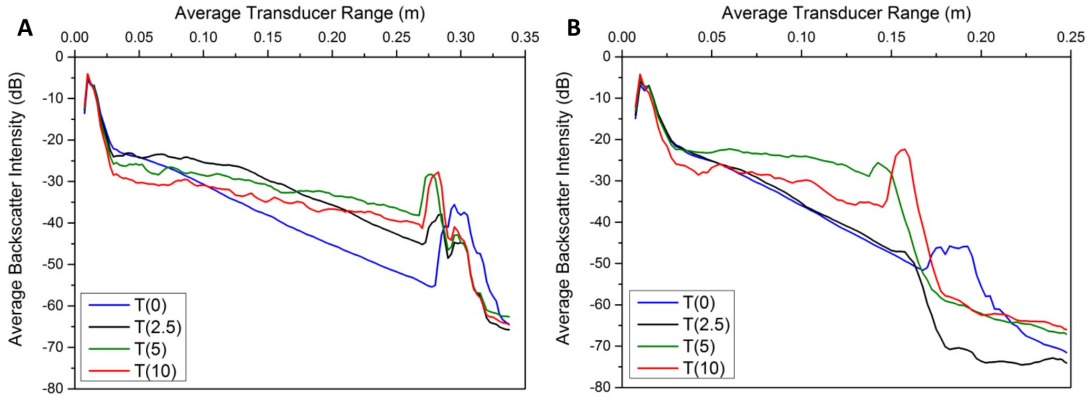

Figure 3.12: Settling backscatter profiles at selected times in minutes, via 1 MHz for; (a) 0.7 vol%, and (b) 1.4 vol% barytes dispersions.

Likewise, the settling profiles obtained via 2 MHz for a 1.4 vol% dispersion have also been presented in the same way, in figure 3.11D-E. Note that due to significantly enhanced signal extinction in this higher concentration scenario, the transducers had to be submerged much further into the suspension. Hence, only a 14 cm depth was profiled, although a 40 cm waterline height was retained akin to the 0.7 vol% case. Naturally this would lead to a relative delay in settling front measurement. The characteristics of the profiles obtained at 1.4 vol% are reminiscent of those at 0.7 vol%, albeit with a few minor differences. Firstly, there is a significant progressive reduction in the column base peak intensity in the profiles directly succeeding T(0), due to sedimentation of more concentrated dispersion. In addition, by T(1), a very small peak is formed in the adjacent position to

the column base peak. By T(2), the intensity of the base peak is negligible, and the adjacent secondary peak has shifted away from the base somewhat and continues to do so in subsequent profiles up to T(5). This essentially corresponds with the positioning of the sediment bed interface, which initially increases in height with time. At T(3), a broad peak is formed close to the transducer and progressively moves closer to the base in successive profiles. Thus inferring the demarcation of a zonal hindered settling front. The settling front peak is more prominent in the higher concentration scenario here. By T(5) in figure 3.11E, the base peak and backscatter intensity is increased but the attenuation gradient of the profile is lowered, suggesting the completion of the sedimentation process. In the final profile at T(10), the sediment bed peak has shifted closer to the base, signifying that the bed has compressed under the hydrostatic load of the water in the final five minutes. The final bed height is 2 cm. The profiles obtained via 1 MHz are depicted in figure 3.12. The corresponding settling front peaks were less prominent in this case due to lowered sensitivity with frequency reduction.

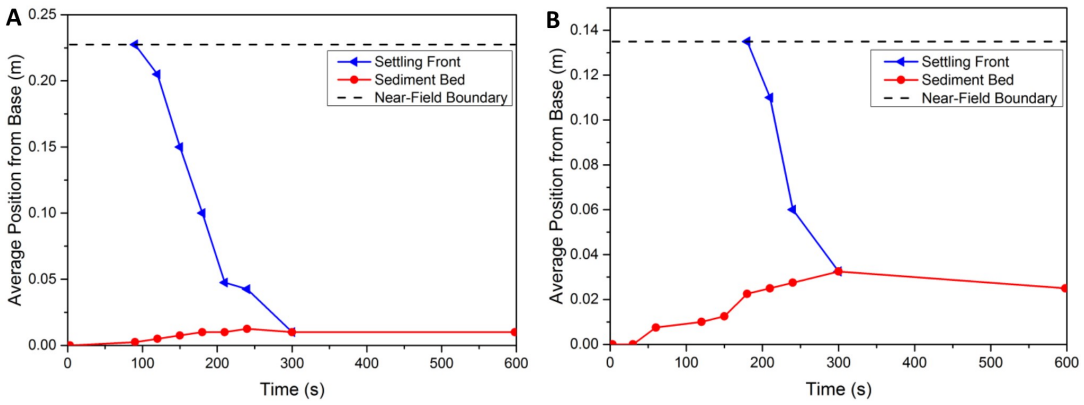

Figure 3.13: Sedimentation curves via 2 MHz at (a) 0.7 vol% and (b) 1.4 vol%.

The data at 1.4 vol% was also extracted to obtain a sedimentation curved, which is presented in figure 3.13B. Once again a zonal hindered settling region is observed, which also slows down after 4 minutes (240 s) following bulk settling. The subsequent slower clarification of fines was not obvious in the 1.4 vol% profiles in figure 3.11D-F. This is likely because the higher concentration yields a more

hindered settling network of particles, hence particle size segregation wouldn't be as enhanced. The sedimentation curves were utilised to calculate sediment bed formation and settling rates. These data are presented in table 3.3 alongside those calculated via the measuring cylinder tests. The settling rates increase with concentration due to enhanced networking which hinders settling. The ABS rate of $0.05\,\mathrm{mm\,s^{-1}}$ for 0.7 vol%, matches that determined via the *ex situ* measuring cylinder technique. Similarly the ABS rate of $0.12\,\mathrm{mm\,s^{-1}}$ at 1.4 vol% is comparable with $0.10\,\mathrm{mm\,s^{-1}}$ determined via the *ex situ* method. The concurring correlation between rates with the classical *ex situ* technique, demonstrates the ability to obtain reliable data via the *in situ* ABS method. Notably, the *in situ* technique provided additional information on the intrinsic dynamics of the bidisperse suspension, which wasn't possible via the *ex situ* method.

Table 3.3: Summary of bed deposition and settling rates

Concentration (vol%)	Measuring Cylinder ($\mathrm{mm\,s^{-1}}$)	ABS Bed[a] ($\mathrm{mm\,s^{-1}}$)	ABS Bulk[b]	ABS Fines[c]
0.5	0.018 ±0.002	-	-	-
0.7	0.047 ±0.003	0.053	1.354	0.417
0.9	0.065 ±0.004	-	-	-
1.4	0.116 ±0.010	0.104	1.292	0.125

[a] Rate calculated from bed height.

[b] Rate calculated for the bulk zonal settling region.

[c] Rate calculated for the slower settling region following bulk settling.

ABS profiling with 2 MHz transducers generated very detailed information on the settling dynamics of the barytes suspensions. An additional point which requires discussion is the successive portrayal of varying levels in profile attenuation in the settling zones in figure 3.11. Since these changes infer concentration changes, the calibration reference was utilised to correlate the attenuation variations with concentration. The relationship was applied to the 5 s and 5 bin distance averaged profiles of $\ln(\psi \mathrm{Vr})$ against r. Concentration was calculated as a moving average between five consecutive distance points. The resulting concentration profiles with respect to depth are presented in figure 3.14 for 0.7 vol%

(A-D) and 1.4 vol% (E-H) at selected times of interest. The vertical line indicates the dispersion's initial bulk volume fraction, the horizontal line marks the settling-supernatant boundary position, and the shaded area represents the sediment bed region.

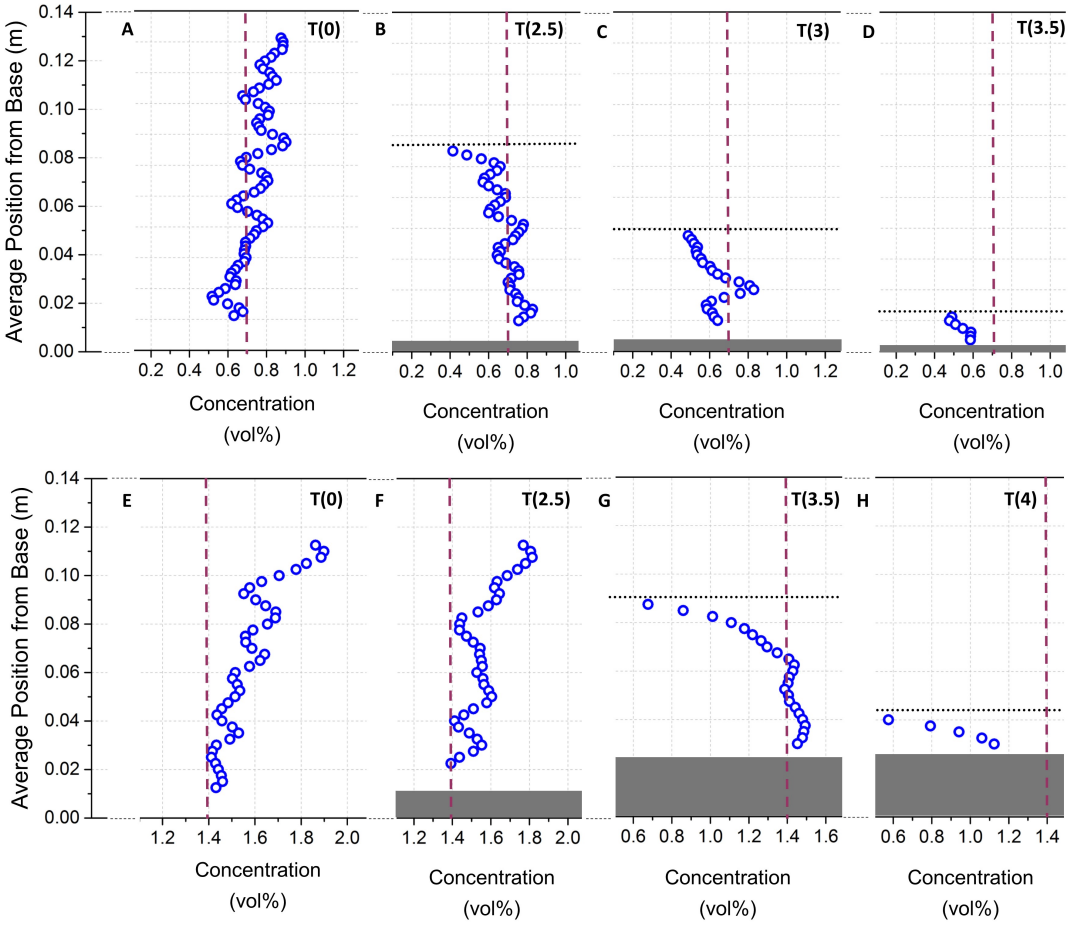

Figure 3.14: Concentration changes with respect to depth at selected time profiles for initial nominal bulk concentration of 0.7 vol% at (a) T(0), (b) T(2.5), (c) T(3), (d) T(3.5), and initial nominal bulk concentration of 1.4 vol% at (e) T(0), (f) T(2.5), (g) T(3.5), (h) T(4). All times given in minutes.

Both concentrations show similar trends within their respective timescales. The dispersions are fairly homogeneous initially, around the expected bulk con-

centration zone, demonstrating good correlation between the reference relationship and actual initial volume fraction set-up within the tank. The earlier profiles A-B and E-F do however depict a greater level in variation than expected. These experiments were conducted within the large perspex column described in section 3.2.1 at a 40 cm fill level. The overhead stirrer was positioned off-centre 10 cm from the base hence in-line with the ABS profiling region. The kick back of particles via the impeller generally suspends them higher in the suspension, which is the likely reason for a slightly less initially homogeneous dispersion in the ABS profiling region. Over time, profiles of both volume fractions depict the development of a concentration gradient from low concentration near the supernatant-settling interface to high concentration in the near-bed region. Generally particles of different sizes settle at different rates in polydisperse barytes suspensions (Balastre *et al.*, 2002). barytes is bidisperse in this case. Therefore size segregation during settling is the likely cause for the concentration segregation that is observed. Interestingly, by the latter profiles in both cases, the variation in concentration is markedly reduced. This indicates that the higher variation in the initial profiles may also be due to the segregation of different sized particles.

3.2.3 Calibration Summary

The backscatter response of barytes suspensions was investigated here for the first time. The dense jagged shaped particles attenuated the backscatter response less than smaller Titania particles and more than larger spherical glass particles(Bux *et al.*, 2015; Hunter *et al.*, 2012a). A calibration of homogeneous barytes dispersions was established from 0.06-1.42 vol%. In addition, application of the Rice method was also extended here to a larger scale set-up where the backscattering and attenuation constants were determined for barytes, which is markedly smaller in size than other particles that have undergone this type of analysis (typically $>100\,\mu m$ (Rice *et al.*, 2014)). The Rice method was also utilised to establish a reference calibration relationship for the first time. Specifically the acoustic attenuation concentration relationship was established for barytes suspensions, such that it can be exploited as a reference to characterise concentration changes

in other barytes suspensions, for examples in the settling tests discussed and the industrial experiments to follow.

The ABS settling tests provided very detailed information on the settling dynamics of barytes. Overall a rapid deposition of dense barytes particles was observed, followed by a delayed deposition in the form of a diffuse settling front. This behaviour was more pronounced at the higher concentration. Since the barytes in these experiments is bidisperse, the larger particles are rapidly deposited in the first instance followed by the slower deposition of the finer size fraction. Different volumes of different size fractions also lead to concentration segregation in the settling region. Interestingly concentration segregation was also revealed via ABS profiling of a 1 vol% polydisperse Titania dispersion (Bux *et al.*, 2015). The ABS settling results reported here compare very well with those via the *ex situ* method and behaviour reported in literature. The ABS data also provides insight on *in situ* concentration changes as settling dynamics evolve. This information should provide insight into predicting settling behaviour in the large scale industrial tank, as well as affirm confidence in the calibration reference to determine concentration.

3.3 Characterisation of a Non-Active Dispersion in an Industrial Impinging Jet Ballast Tank

This section reports the methodology and results of the industrial experimental programme. Specifically, the ABS profiles a large scale tank which utilises impinging jet ballasts to resuspend settled particles. Information is gained on the mobilisation of particles with respect to jet and air-lift operational regimes. The barytes attenuation-concentration reference relationship, and settling tests in the preceding calibration section, mediate characterisation of suspension dynamics in the large scale tank.

3.3.1 Experimental Methods

The Four Tenths Rig (FTR) at the National Nuclear Laboratory (Workington, UK) was utilised for industrial experimental trials. The FTR is a 40% scaled

version of a Highly Active Storage Tank (HAST), at Sellafield Ltd (Cumbria, UK). The HAST is a storage vat which routinely mobilises radioactive liquor waste, to prevent settled particles forming radioactive hotspots. The FTR design comprises three primary features; impinging jet ballasts to resuspend and mobilise settled particles, dummy cooling coils to remove radioactive decay heat, and air-lifts to generate turbulence and enhance particle mixing and mobilisation. The FTR is 2.5 m in height and 2.6 m in diameter and is supported on a platform (refer to figure 3.15 for schematic). At 100% fill, the FTR contains 12.10 m^3 of water generating a waterline height of 2.28 m from the base, or 1.44 m at 50% fill. The overview in figure 3.1D shows the positioning of six equidistant peripheral jets and a central jet with a vertically positioned nozzle. The jet nozzles have a 15.25 mm diameter. The Central Jet nozzle is vertically positioned 375.1 mm above the base and the peripheral jets are angled towards the wall and positioned 234 mm above the base. The jet ballasts essentially withdraw fluid from the FTR and fires it out at a known velocity, creating an impingement which erodes the sediment bed to resuspend settled particles (refer to schematic in figure 3.1C). At 40 Hz pump operating frequency, the Central Jet has a maximum flow rate of 230 l min^{-1} and the peripheral 196 l min^{-1}. During operation, the jets velocity profile increases, reaches a plateau and then eventually decreases. There are also four air-lift pipes which comprise perforated dispersion nozzles. The upper and lower positions of the nozzles are 209 mm and 67 mm respectively, from the base. They inject air into the suspension to promote mobilisation and homogenisation of suspended particles. It is critically important to understand the level of mixing achieved both with and without air-lift operation. The FTR also comprises dummy coils which occupy a large volume of the tank, to replicate the significant obstruction of the cooling coils in the actual HASTs.

The AQUAscat 1000 ABS (Aquatec Group Ltd, UK) was deployed here with 1 x 1 MHz and 1 x 2 MHz transducers. The 1 MHz was positioned approximately 80 cm from the base to monitor large depth scale suspension changes, due to its enhanced depth penetration compared with the higher frequencies. The 2 MHz which is relatively more sensitive, was positioned approximately 30 cm from the base to capture developments within the near-base region. Consequently the probes were not strictly co-located. The 1 MHz transducer was positioned closer

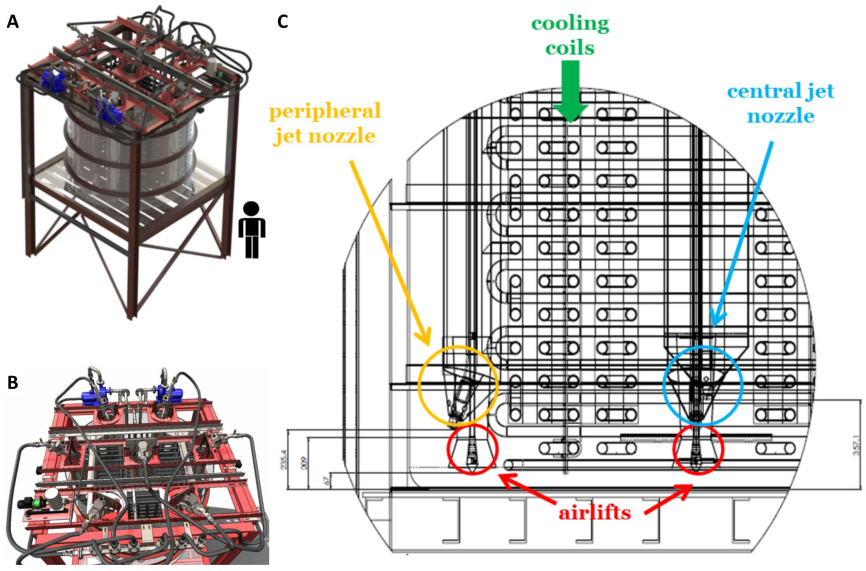

Figure 3.15: FTR CAD schematics; (a) side view, (b) overview and (c) section drawing of internal structure at the base, from Dodds (2015).

to Jet 2 and 2 MHz was positioned closer to Jet 3. The schematic in figure 3.16 provides an indication of the positioning of the transducers relative to Jets 2 and 3, although it is not to scale. Incidently the region between Jets 2 and 3 was the only access point free from internal coils to enable ABS measurement. A transducer pulse repetition rate of 64 Hz was operated with one full depth profile collected every second, which enabled sufficient time between backscattered pulse measurement and the emission of the subsequent pulse. The depth profiles were segregated into 5 mm measurement bins.

A range of HAST operation cycles were replicated in the FTR in order to better understand daily operational dynamics. Their influence on bed erosion, resuspension and settling dynamics was investigated to justify acceptable time frames between operating cycles. The implemented regimes are summarised in table 3.4. Notably there were constraints associated with operating the large scale experimental rigs, which directly impacted regime selection. Regimes 1 and 2, where only Jet 1 and the Central Jet were operated, are analogous to the preliminary trials conducted by Hunter *et al.* (2012c) in the first stage of the study to gauge whether the ABS could be applied in an industrial tank

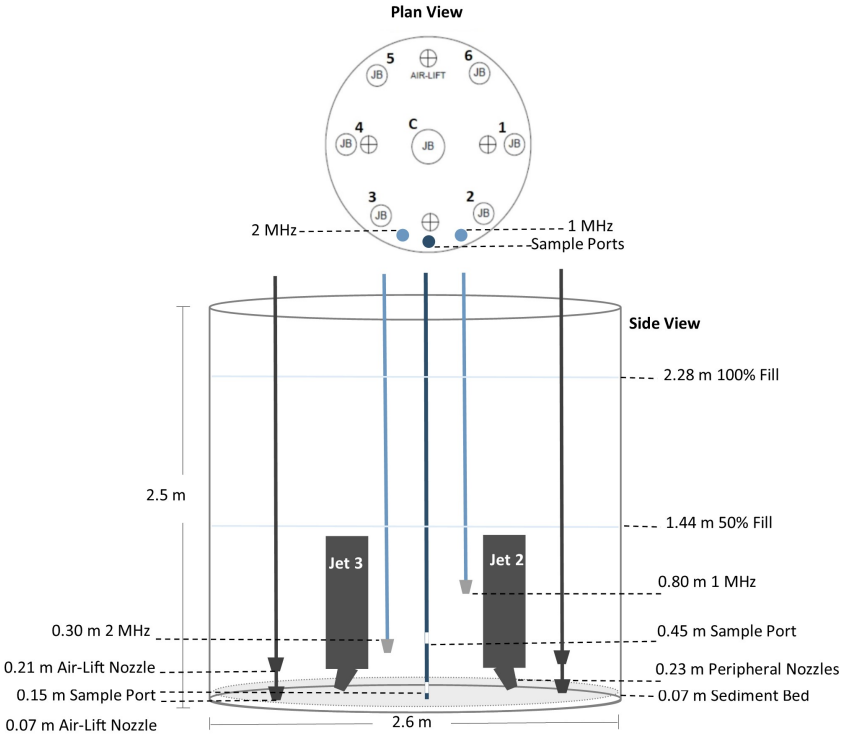

Figure 3.16: Top down view and side-view schematic, denoting the positioning of transducers and sampling ports relative to Jet 2 and Jet 3 (not to scale).

scenario. Notably the dummy cooling coils were not present in the FTR during the corresponding experiments. Regimes 3 and 4 are more representative of those implemented in actual daily HAST operations. Regime 4 investigates the effects of air-lift operation. Note these are only usually operated to homogenise the dispersion during HAST decanting operations. ABS measurement commenced upon firing of the final jet in each regime and ceased by 30 minutes post firing. Hunter *et al.* (2012c) previously established that the suspended particles settled close to background levels well within a 30 minute time frame. Although for precaution, 60 minute inoperative periods were allowed between experiments, to provide a practicable time frame for sediment to resettle close to background levels. One minute background readings were taken in between experiments.

Regime 4 experiments were conducted at a later stage, by which point a second 2 MHz probe had been acquired. Therefore in this case, the additional probe was

Table 3.4: FTR experimental regimes

Regime	Jet Sequence	Burst Duration	Fill
R1	1	40 min	50%
R2	1+C	40 min	50%
R3.1[a] / R3.2[b] / R3.3[c]	2 cycles with 100 s delay between jets; 5+C, 6, 1, 2, 3, 4	20 s	50%
R4.1[d]/ R4.2[e]	2 x clockwise cycles; 4, 5, 6, 1, 2, 3 & C[f]	20 s	100%

[a] ABS measurement taken after Jet 2.

[b] ABS measurement taken after Jet 3.

[c] ABS measurement taken after Jet 4.

[d] No air-lifts.

[e] All air-lifts operated throughout regime.

[f] Central Jet continuously operated throughout regime.

co-located with the 1 MHz to profile changes in the corresponding upper region. By this stage it was also possible to conduct an independent sampling experiment using Regime 4, in order to gauge actual physical solids concentration. Sampling was initiated post firing of Jet 2 in the second cycle, i.e. 30 s prior to cycle completion. 2 x 20 ml samples were extracted with a peristaltic pump at selected times. An initial experiment extracted samples at 15 cm from the base (near-bed region). Additionally it was possible to access the underside of the transparent rig and observe the bed clearance profiles generated by each jet. The length (diameter) and width (radius) of the semi-ellipsoid clearance profiles pictured in figure 3.17B were measured to determine eroded surface area in Regime 4.

3.3.2 Results & Discussion

FTR Results; Regime 4 (Erosion)

Initially the erosion success of the jets is discussed. During Regime 4 without air-lifts, the sediment bed clearance area was estimated from the measured length and width of the cleared semi-ellipsoid shape. The modelled jet clearance pattern from McArthur *et al.* (2005) is shown in figure 3.17. The profiles in the

experiments were eroded inhomogeneously however, and formed semi-ellipsoid type shapes, similar to the approximate shape pictured in figure 3.17. The actual measured dimensions and resulting surface area values of the eroded bed profiles are presented in table 3.5, to give an indication of jet clearance success. In many cases in table 3.5, the measured radius is not directly half the value of the measured diameter, thus inferring inhomogeneity. The surface area was calculated assuming a semicircle which provides an over estimation for this shape. Therefore the surface area was calculated using both radius and diameter measurements, and the difference was subtracted from the largest surface area value, in an attempt to provide a more realistic surface area value for the semi-ellipsoids, as provided in table 3.5. The cleared surface areas of the peripheral jets 1 - 6, are very similar. The Central Jet exhibited a circular profile due to the nature of that particular jet. In this case the clearance profile was compared for when it was fired in sequence with the other jets (short bursts), with that of the clearance when fired continuously during the sequence of the six other jets (a markedly longer duration). The $0.79\,\mathrm{m}^2$ clearance in the latter scenario is markedly improved compared to the $0.28\,\mathrm{m}^2$ clearance in the short burst scenario. This demonstrates that longer jet firing is required to improve erosion, however increasing duration by a factor of six times didn't correspond with the same clearance ratio. The maximum clearance would be governed by the jet dimensions and velocity. The duration necessary to achieve full clearance would require further investigation, so that optimal firing times could be determined. Interestingly, the jet clearance model from McArthur *et al.* (2005), suggests that there are inevitably bed regions which remain unperturbed, thus full clearance is not achieved. This would certainly be a problematic scenario if reminiscent in an active HAST.

FTR Results Regime 1-3 (Erosion, dispersion & settling)

Here the results of Regimes 1 - 3 are reported. In particular, sediment erosion, redispersion and resettling are discussed. In figure 3.18A-B the backscatter profiles are presented for all regimes via 1 and 2 MHz respectively. They represent the average profiles taken over five consecutive seconds. Longer time averages

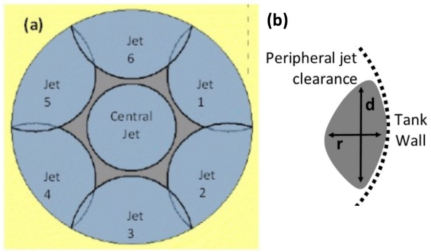

Figure 3.17: (a) Jet clearance pattern adapted from McArthur *et al.* (2005) and (b) approximate shape of cleared sediment.

Table 3.5: Summary of measured clearance dimensions and associated clearance area for each jet

Jet	Radius (m)	Diameter (m)	Clearance Area (m^2)
Central (continuous)	0.50	-	0.79
Central (in sequence)	0.30	-	0.28
1	0.47	0.94	0.35
2	0.46	1.00	0.33
3	0.50	1.07	0.39
4	0.51	0.92	0.33
5	0.53	0.92	0.33
6	0.52	0.97	0.37

were not taken in order to smooth the data because the settling tests in section 3.2.2 (Settling Test Results), suggested that barytes undergoes rapid bulk settling. These particular profiles haven't been smoothed by distance averaging so that peak intensities are retained in order to observe bed dynamics.

First and foremost, Regimes 1 and 2 portray a strong peak at a transducer range of 0.75 m. Interestingly Regime 3.1-3.3 displays a shift in the peak away from the transducers. This implies that the peak corresponds with the sediment bed position, not the FTR base. This also suggests that the bed was not eroded from the base in the ABS profiling region by Regimes 1 and 2. This is somewhat unsurprising since Regimes 1 and 2 utilise jets which aren't in the vicinity of the ABS measurement region. The jet clearance model from McArthur *et al.* (2005) in figure 3.17, indicates that the overlap in bed clearance by neighbouring

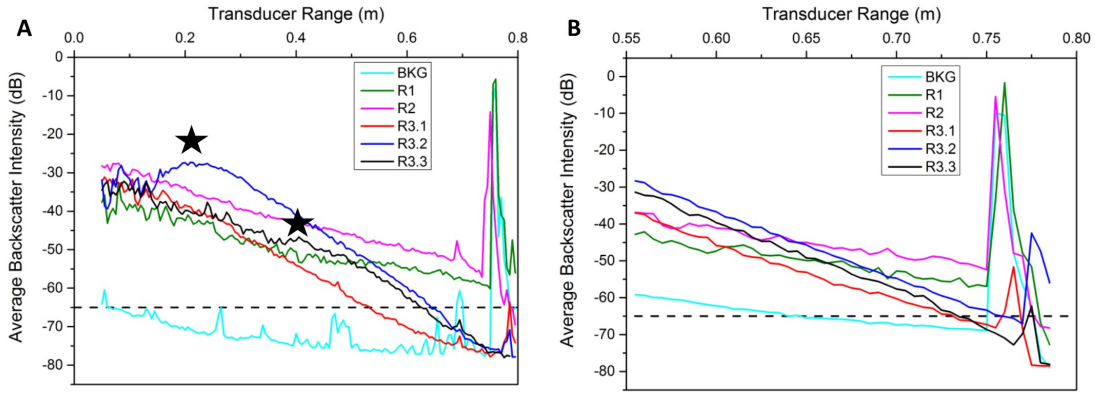

Figure 3.18: Time averaged backscatter profiles at T(0) via (a) 1 MHz upper region and near-bed, and (b) 2 MHz near-bed region. Asterisks indicate position of settling front.

jets is only minor. The 1 MHz however does show a very minor additional peak in the near-bed region for Regime 2. Since the probes were not co-located, it is possible that some eroded sediment from the Jet 1 and Central Jet regions, may have swept into the 1 MHz profiling zone (Jet 2 region). Indeed, Regime 2 which simultaneously employs Jet 1 and the Central Jet, depicts a stronger overall backscatter intensity than Regime 1 (Jet 1 alone). This corroborates some minor sweeping of particles from the Jet 1 and Central Jet regions, into the ABS profiling zone. These findings suggest that although there is minor mobilisation of particles between neighbouring jets, the cooling coils are hinder the movement of resuspended particles around the FTR, hence resuspension is very much localised. Hunter *et al.* (2012c) also reported in very preliminary investigations that, although the jets are sufficient at resuspending the sediment, they are poor at dispersion and homogenisation resulting in a fluidised bed in the near-bed region. Hunter *et al.* (2012c) experiment was conducted without the presence of cooling coils. Here, the cooling coils significantly obstruct the mobilisation of resuspended particles. Therefore operation of the jets alone, is unlikely to achieve optimal mobilisation and homogenisation of resuspended particles.

Now focussing on the near-bed 2 MHz profiles of Regime 3 (figure 3.18 B), there is a significant reduction in the sediment bed peak intensity in the vicinity

of the probes. R3.1 corresponds with measurement directly after the firing of Jet 2, which is not entirely in the vicinity of the 2 MHz profiling zone. However since some erosion is witnessed, it may be within the small overlap region between Jet 2 and 3, as shown on the jet clearance model in figure 3.17. R3.2 corresponds with measurement directly after firing of Jet 3 which is the closest jet to the 2 MHz probe. Here further erosion of the bed is indicated by the additional shift of the bed peak. The initial bed height measured at the tank walls was approximately in the 5-7 cm range. The maximum peak shift incurred in Regime 3 was cm, indicating that the bed was not eroded from the base in its entirety, within the ABS profiling region. Likewise the clearance patterns observed from the underside of the tank were incomplete and inhomogeneous. These observations are very impactful with respect to HAST operating regimes, especially if they do not achieve maximum clearance.

When referring back to R3.2 1 MHz profile (figure 3.18), a broad peak is observed at a transducer range of 0.2 m, signifying the height to which the eroded particles were resuspended. The peak shifts further down the column to approximately 0.4 m by R3.3 which corresponds with measurement directly after Jet 4 which is further away, hence indicating resettling. By this stage the bed height is also slightly increased inferring the deposition of some resuspended particles. Settling rate between R3.2 and R3.3 is 0.8 mm s^{-1} which is equivalent to the rate of 50 mm min^{-1} calculated by Hunter *et al.* (2012c). The rapid settling behaviour observed, signifies the importance of maintaining and optimising jet operations in a HAST.

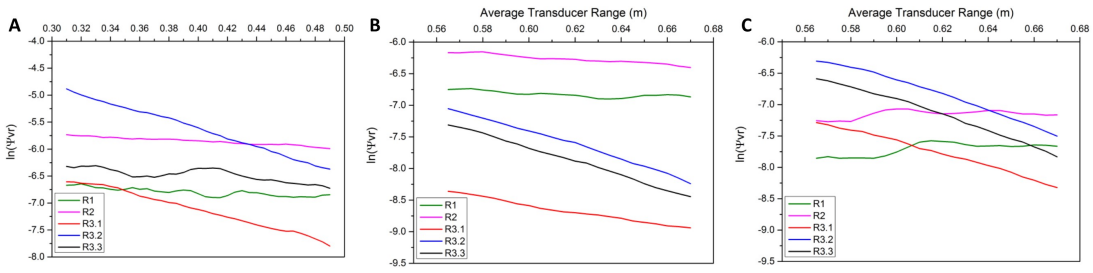

Figure 3.19: G=ln(ψVr) against r profiles of (a) upper region via 1 MHz, and near-bed regions via (b) 1 MHz and (c) 2 MHz.

Naturally the attenuation of the Regime 3 profiles is significantly enhanced compared with those of Regimes 1 and 2, owing to improved particle resuspension within that region. The attenuation changes in the near-bed region were quantified in terms of concentration by using the 1 and 2 MHz calibration reference relationship for barytes. Firstly, the G function (G=ln(ψVr)) was plotted with respect to transducer range for the upper (0.31-0.49 m) and near-bed (0.56-0.67 m) sections of the profiles. Figure 3.19A depicts the upper zone via 1 MHz, and B-C depict the near-bed zone via 1 and 2 MHz respectively. Note the G function was taken as a moving average over five consecutive time and distance bins, to reduce the influence of noise. Concentration was then calculated using the corresponding linear slope of $\frac{dG}{dr}$. Concentration was not calculated for R1-2 2 MHz as those particular natural log profiles didn't depict a linear attenuation, due to high variability.

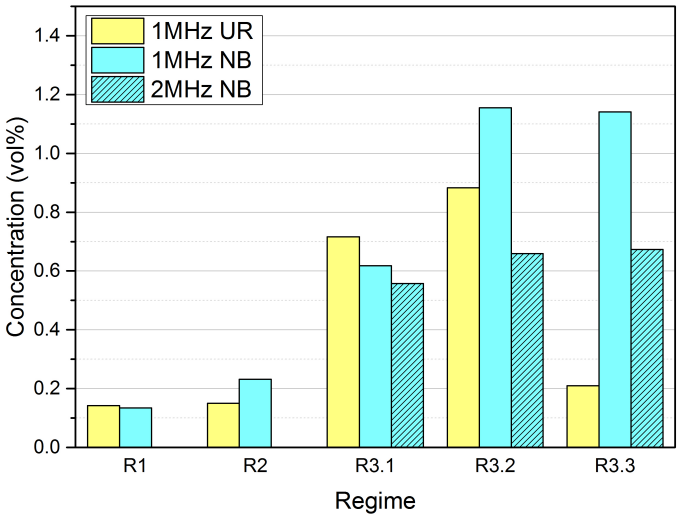

Figure 3.20: Concentration change per regime measured in the upper-region and near-bed with 1 and 2 MHz.

The corresponding concentrations are quantified on a bar chart in figure 3.20. Firstly the upper and near-bed zones show minimal sediment resuspension via 1 MHz for Regime 1 as expected. For Regime 2, although there is little resus-

pension in the upper region, a slight increase in concentration is noticed in the near-bed, which corresponds with the sweeping scenario previously discussed. In the 1 MHz upper region, suspended concentration increases markedly from R2 to R3.1, slightly increases from R3.1 to R3.2 and notably recedes from R3.2 to R3.3. These observations align with the resuspension settling front and resettling scenarios discussed. The $0.8\,\mathrm{mm\,s^{-1}}$ settling rate calculated between R3.2 and R3.3, corresponds with concentrations <0.7 vol%. This rate is lower, but comparable to the barytes settling rates derived in the calibration experiments in table 3.3.

In the near-bed region the volume fraction is higher than in the upper zone and is significantly higher by R3.3. This is indicative of the rapid particle deposition behaviour seen in the laboratory settling tests (section 3.2.2 Settling Test Results). Note at R3.2 and R3.3, there is a marked discrepancy between estimated concentration in the near-bed between the 1 and 2 MHz probes. Generally, the 2 MHz is more sensitive to concentration fluctuations than the lower frequency, and there is also less noise associated with the measurement. However, the primary reason for the observed difference, is because the two frequencies were not co-located. This observation in itself highlights the lack of mobilisation and homogeneity throughout the tank, when the jets alone are operated. This leads onto the discussion of the impact of air-lifts with respect to the ability to mobilise eroded sediment.

FTR Results Regime 4 (Mobilisation & Settling)

Here the erosion, dispersion and resettling of particles are discussed with specific focus on mixing dynamics with respect to air-lift operation. Thus far it is clear that the jet operation alone doesn't promote suitable mobilisation of eroded particles, such as to prevent rapid resettling. Therefore the impact of operating air-lifts is directly compared with the mixing achieved without their operation.

Backscatter profiles were obtained for Regime 4 both with and without air-lift operation. The level of dispersion in each scenario is compared in the corresponding attenuation profiles presented in figure 3.21A (without), and figure 3.21B (with). Specifically in this figure, the changes in attenuation of the backscatter profiles are presented with respect to time. Levels of attenuation experienced in

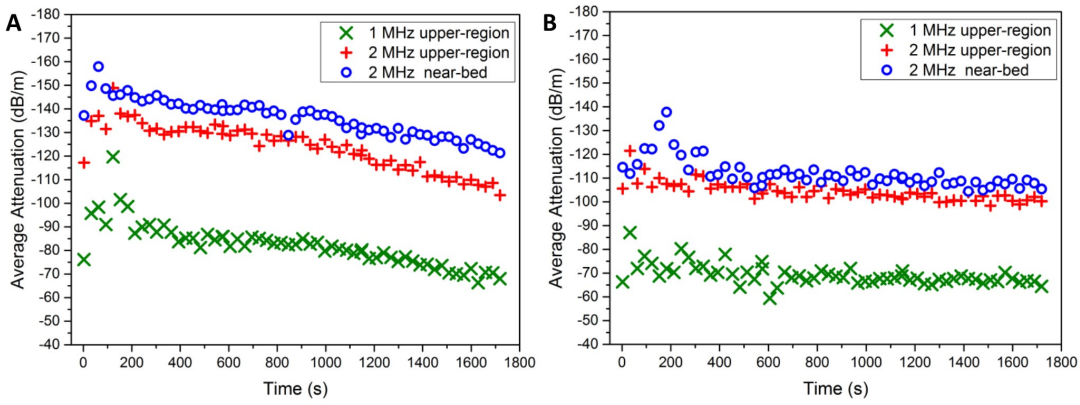

Figure 3.21: Average backscatter attenuation changes with time in the upper-region measured via 1 and 2 MHz, and near-bed region measured by 2 MHz (a) without air-lift and (b) with air-lift operation

the upper-region via 1 and 2 MHz, and in the near-bed via 2 MHz are compared. In the first instance, the initial data in the region of T(0) depict high variability, which is associated with the initial mixing of the dispersion from recent jet fire. The 1 MHz results naturally exhibit systematically lower values of attenuation than the 2 MHz as expected. Measurements were initiated after the firing of Jet 2 although the cycle completed at Jet 3. During this time erosion and particle dispersion was still underway, hence the initial data points in all profiles show a corresponding increase in attenuation. Both profiles with and without air-lifts depict a general reduction in attenuation overtime, which is indicative of a settling dispersion. Importantly, the gradient representing the reduction over time in the air-lift scenario (figure 3.21B), is very shallow in comparison to no air-lift operation (3.21A). This denotes very gradual and diffuse particle resettling in the air-lift case. Additionally, the general attenuation values are also lower here. Importantly, these observations suggest improved mobilisation and a enhancement in particle resettling duration, in this particular regime.

These settling dynamics can be correlated with particle size. The size distributions of samples withdrawn from the near-bed at various regime intervals in minutes, are presented in figure 3.22. On the first hand, the T(0) profiles with air-lift operation demonstrate the resuspension of larger particles compared with

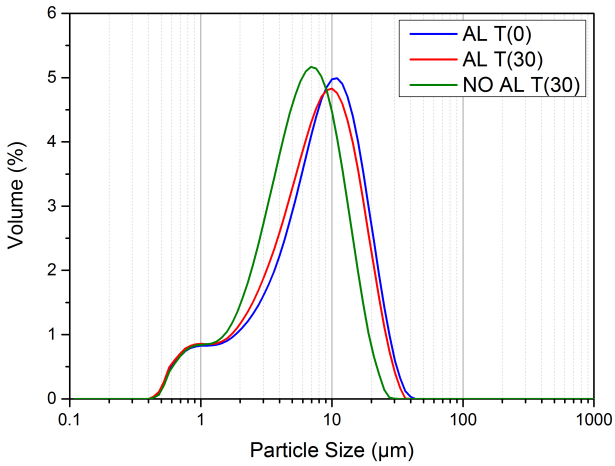

Figure 3.22: Comparison of size distribution of suspended particles at selected times and regimes. Time given in minutes.

the no air-lift scenario. This suggests that the jets alone are not sufficient at dispersing eroded sediment. Additional turbulence is required to enhance dispersion of a wider distribution of particulates. The profiles at T(0) and T(30) with air-lift operation do not vary much, inferring that redispersed particles are well mixed beyond the localised jet region.

Referring back to figure 3.21, attenuation values with air-lift operation are systematically less than without. This indicates lowered concentration, and hence improved dispersion of resuspended particles beyond the localised jet region in the air-lift regime. Indeed the similarity in attenuation values via 2 MHz measurement in the upper and near-bed profiles, corroborates this, as well as demonstrating general homogeneity within both regions of the FTR. On the other hand, there is a distinct segregation in attenuation via 2 MHz measurement in the upper and near-bed 3.21A, indicating inhomogeneous dispersion without air-lifts.

Samples were withdrawn from the FTR at 15 cm (near-bed zone) in order to compare the characterised concentrations using the G procedure previously discussed, with actual physically measured concentration. Figure 3.23 compares sampling and characterised values obtained in both with and without air-lift scenarios. Specifically, ABS concentrations were calculated using the measured

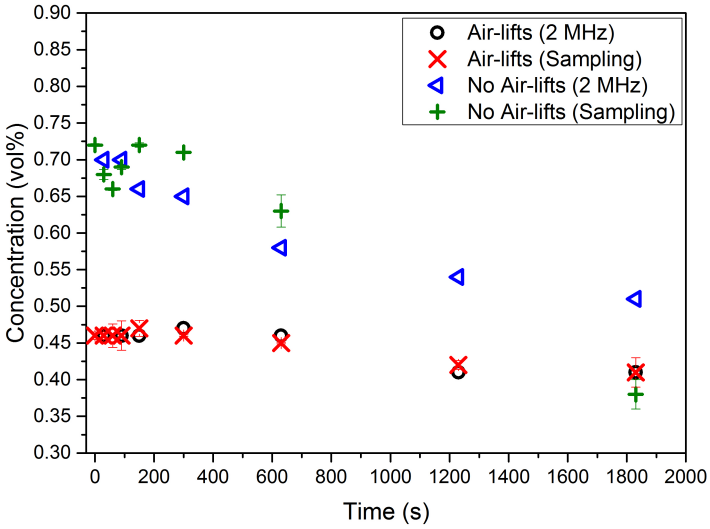

Figure 3.23: Comparison of concentration measured via ABS and physical sampling in the near-bed region, with and without air-lift operation.

range 10-20 cm, whereas the samples were taken at a specific 15 cm point from the base. In the first instance, air-lift concentrations are markedly lower than the alternative scenario. The gradient in both cases also follow the corresponding trends as discussed. But most importantly, both sets of data demonstrate that the characterised concentrations align well with actual measured samples, ensuring confidence in the G method and the reference concentration-attenuation relationship obtained in from the calibration.

These concentration changes are also henceforth presented with respect to depth, in figure 3.24. Specifically, fluctuations in the near-bed zone via the 2 MHz, are shown at selected time profiles in minutes. Figure 3.24A represents the changes in the absence of air-lift operation. As discussed, the corresponding profiles do corroborate slightly higher concentrations than those in figure 3.24B, the air-lift scenario. Interestingly they also show a greater span in concentration range per profile, suggesting that the resuspended particles are not as homogeneously dispersed in the measurement zone. In both cases, from T(0) to T(2), there is increased variability as the settling dispersions become less homogeneous

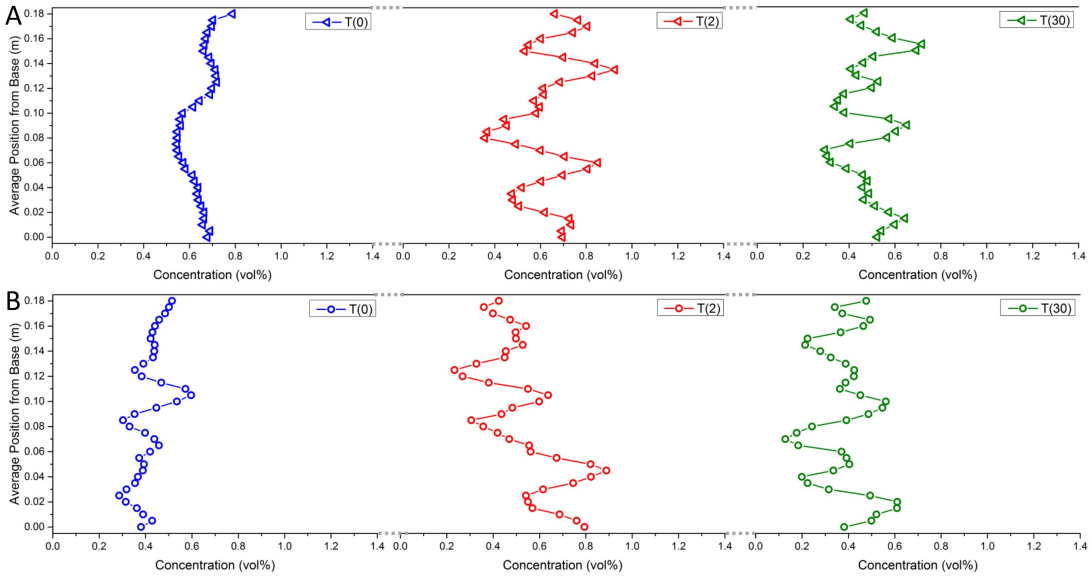

Figure 3.24: Concentration changes measured with 2 MHz in the near-bed region (a) without air-lift and (b) with air-lift operation.

over time. This is possibly due to obstructions in settling owing to the presence of cooling coils. Additionally by T(30), there is an overall reduction in bulk concentration without air-lifts in A, where as it remains unchanged in the air-lift case in B, thus corroborating the enhanced dispersion of particles beyond the localised jet region in the latter. This observation concurs with settling observed in the bench scale settling tests at low volume fractions < 1 vol%(refer to section 3.2.2 Settling Test Results), where settling was diffuse (Balastre *et al.*, 2002). In this case a clarifying supernatant - settling suspension boundary was not formed and the dispersion remained turbid for some time post operation.

3.3.3 Industrial Characterisation Summary

The ABS profiled a large scale non-active HAST tank in order to model how jet and air-lift operation influence sediment erosion, dispersion and resettling dynamics. The calibration reference relationship that was determined via the Rice method was successful at quantifying backscatter attenuation changes with actual

physical concentration changes within the industrial scale tank. The information that was attained suggested very localised resuspension with rapid settlement of larger particles in jet only operations. The smaller size fraction remained suspended for quite some time however, particularly in the case of air-lift operation. Air-lift operation generally enhanced particle dispersion. Neighbouring jets did not influence erosion dispersion in adjacent regions much, although there was minor sweeping of sediment from the Central jet into adjacent zones. Jet clearance was inhomogeneous and the bed wasn't eroded from the base in its entirety in any scenario. Ultimately, inhomogeneous and incomplete jet clearance would be problematic from an operational perspective as this would readily impact the formation of radioactive hotspots on the HAST base.

The information gathered from these experiments is very insightful to understanding and modelling erosion, dispersion and settling behaviour of a dense material in a HAST. It is invaluable in terms of optimising daily operations. Notably the methodology here required an initial laboratory calibration to enable actual quantification of concentration changes in the FTR. Perhaps in the case where a laboratory calibration is not possible, say due to suspension radioactivity, ABS measurement is still insightful because analysis of attenuation changes in a backscatter profile can infer concentration changes and settling dynamics from a qualitative perspective, as was seen here. Quantifying these changes into actual concentration changes in this work served to corroborate the behaviour that had been inferred from looking at the profiles in the first instance.

The dynamics of mixing in large scale tanks in nuclear engineering and the broad process engineering context, is not generally well understood, and relevant information is not easy attained via *in situ* methods (De Luca *et al.*, 2004; Iritani *et al.*, 2009). The novelty in this work not only lies in the application of the instrument and corresponding Rice and empirical methods for characterisation on a very large scale. But also in the knowledge and understanding that was gained about a complex dispersion in a very complex tank system.

Chapter 4

Manufacture and Acoustic Research of a Latex Particle System

Chapter 4 reports on the novel manufacture and acoustic characterisation of a latex dispersion system. Initially section 4.1 explains the reasoning and drive for this research. In sections 4.2 - 4.5, the novel manufacture of monodisperse emulsions via a high throughput controlled jetting regime is discussed. Subsequently the emulsions are successively polymerised on a large 2l scale, yielding latex beads which retain initial droplet size characteristics. The challenges involved in achieving optimal polymerisation and corresponding reformulation requirements are discussed. Particle size, shape and stability characteristics are determined via various techniques, and the particles are subsequently aggregated. In sections 4.6 - 4.8, the acoustic backscatter response of all three systems; the emulsion and corresponding aggregated and non-aggregated particle dispersions, are directly compared for the first time here. Acoustic properties such as sediment attenuation and backscattering constants are also directly derived via the Rice method.

4.1 Introduction

The preceding chapter reported on extending ABS application beyond its traditional scope, and demonstrated characterisation capability within relatively

concentrated inorganic mineral suspensions; both on the small laboratory and large industrial scale settings. Naturally it was fitting to extend these investigations to suspension systems comprising organic particles. To relate back to the original driving theme of the project and as discussed in chapter 1 section 1.1, complex organic type sludges are common contaminants in the nuclear industry, for example in the Pile Fuel Storage Pond (Sellafield Ltd, Cumbria), an open air, spent radioactive nuclear fuel storage pond, comprising additional bio-disperse materials. Characterisation of this facility and various other tanks and silos is highly complex (Gregson *et al.*, 2011; Jackson *et al.*, 2014). However the ability to perform even rudimentary *in situ* qualitative characterisation of the sludges and suspensions would certainly be beneficial for the monitoring and eventual decommissioning of such facilities.

On a broader scope, organic suspensions are ubiquitous in countless industries including foods, paints, pharmaceuticals, cosmetics and so forth. Consequently the acoustic response and characterisation of organic emulsions and latex suspensions have been investigated by various groups, mainly McClements (1991) in food science, and (Holmes *et al.*, 1993) and (Tebbutt & Challis, 1996) in engineering. These groups have demonstrated the capability to determine particle size and volume fraction via small scale *ex situ* instrumentation, using a broad band frequency attenuation measurement approach outlined in chapter 1 section 1.2.2.

Another area of significant interest with respect to developing ABS characterisation capability in arbitrary suspensions, is the influences of particle aggregation on acoustic backscatter response. This is primarily because there are innumerable suspension systems both in nature and in industry which incorporate aggregated particulate structures. Some groups have investigated this via kaolin suspensions (Austin & Challis, 1998; MacDonald *et al.*, 2013), glass beads suspensions (Hunter *et al.*, 2012b; Thorne *et al.*, 2014) or emulsions (McClements, 1994). However the interaction is very complex (McClements *et al.*, 1998) and is not yet well understood for application of *in situ* instrumentation (Rouhnia *et al.*, 2014; Vincent & MacDonald, 2015).

Latexes are organic polymer particles which are typically stabilised in dispersion by the presence of a surface charge. Hence they can be readily destabilised and aggregated via the addition of an electrolyte (Burns *et al.*, 1997), making

them an ideal choice for the research in this chapter. Furthermore, they also have a density close to that of water ($\sim$1 g cm^{-3}) which is advantageous because they would provide relatively non-settling particulate dispersions for experimentation. Acoustic research of polymer micro-spheres is also relevant because they have many applications in the aforementioned industries.

The primary focus of this chapter is the development of a robust manufacturing method for monodisperse Latex dispersions on a relatively large litre scale with high throughput rates. Generating large volumes of monodisperse dispersions for acoustic testing is challenging, so membrane technology which provides a route for upscaling is investigated. Thus a novel protocol is established to facilitate rapid manufacturing for future acoustic Latex studies. Particle generation in the near colloidal size range akin to Barytes in chapter 3 is attempted to enable direct comparison of acoustic density effects. A secondary but equally important aim is the acquisition of *in situ* backscatter data to firstly understand the influence that soft particle scattering mechanisms have on the signal in such a device, and also investigate the differences when scattering arises from particles that have undergone aggregation. The acoustic response of three systems obtained from *in situ* instrumentation; initial emulsion, polymerised dispersion and aggregated dispersion, are compared directly for the first time here. Furthermore the Rice method is tested under organic dispersion systems and corresponding sediment attenuation and backscattering constants are derived. Since the *ex situ* techniques typically utilised for characterisation of such dispersions relay on attenuation measurement (chapter 1 section 1.2.2, the backscattering properties of such particles has not previously been quantified in this respect.

4.2 Particle Synthesis Literature Review

A latex suspension comprises of organic polymer particles. A synthetic latex can be manufactured by polymerising an emulsified monomer. A simple emulsification involves the dispersion of a liquid in the form of droplets within an immiscible liquid. Typical emulsification methods include ultrasonics (Biggs & Grieser, 1995), high pressure homogenizers, rotor-stator systems and colloid mills (Gijsbertsen-Abrahamse *et al.*, 2004). These techniques generate turbulent flows

to rupture droplets of one liquid phase within a continuous liquid phase. Hence energy requirements are substantial and droplet size distribution is poly disperse, since it depends on the magnitude of flow turbulence which is inherently difficult to control and cannot be homogeneous throughout a reaction vessel (De Luca *et al.*, 2004). Thus generating monodisperse particles is costly.

Alternatively, membrane emulsification (ME) technologies encompass a drop-by-drop production approach whereby droplets are formed *in situ* via the permeation of a pure disperse phase through a membrane into a continuous phase. Droplet detachment is induced by an imbalance in shear stress at the membrane - continuous phase interface and also in the Laplace pressure, hence energy requirements are markedly reduced and the droplet size distributions of the resulting emulsions are more uniform. Consequently ME is considered to be more ideal for industrial scale-up (Charcosset *et al.*, 2004; Joscelyne & Trägårdh, 2000; Santos *et al.*, 2015).

ME was first demonstrated by Japanese groups (Nakashima *et al.*, 1992; Omi *et al.*, 1994) whom utilised Shirasu Porous Glass (SPG) membranes made from Shirasu (Japanese volcanic ash), lime and boric acid. Since their pioneering work, a variety of membranes have been developed from other materials including ceramic (Williams *et al.*, 1998), metallic, polymeric and micro-engineered devices (Vladisavljević & Williams, 2005). Furthermore ME has also branched out into numerous technological variations, including; cross-flow or shear induced by a stirred cell (Dragosavac *et al.*, 2008), membrane rotation in a stationary continuous phase (Manga *et al.*, 2012), membrane oscillation normal to the disperse phase flow (Holdich *et al.*, 2010) and emulsification via a membrane with micro-channels (Simons *et al.*, 2013). There are innumerate applications for membrane technologies; formulation in pharmaceutical, foods, cosmetics and paints industries are typical reoccurring themes (Peng & Williams, 1998). For the purposes of this study, the cross-flow membrane emulsification (XME) technique, which incorporates a ceramic membrane, was utilised. Thus, henceforth a literature review of XME and the subsequent polymerisation stage is presented.

4.2.1 Crossflow Membrane Emulsification

The XME process involves the pressurisation of the disperse phase through the pores of a micro-porous membrane, and subsequent dispersion into the continuous phase. The emerging disperse phase is unstable with respect to the continuous phase it is entering, thus it reduces its surface tension by forming droplets to minimise its interfacial area, also known as the Rayleigh-Plateau instability (Nunes *et al.*, 2013). Since the continuous phase flow is coaxial to the membrane surface from which the disperse phase is emerging, a drag force is induced which shears droplets as they grow at the pore tips and disperses them in the crossflow (Williams *et al.*, 1998). The process of emulsification is illustrated in figure 4.1.

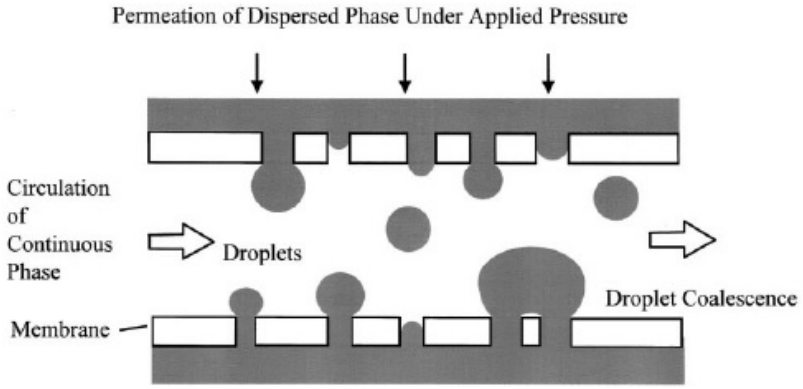

Figure 4.1: Membrane emulsification schematic from Joscelyne & Trägårdh (2000).

There are a multitude of parameters which influence the emulsion droplet size, and these are typically categorised as either membrane, formulation or process related (Spyropoulos *et al.*, 2014). Interfacial tension and the counteracting viscous forces of the fluid which oppose droplet growth are formulation related parameters (Nunes *et al.*, 2013; Spyropoulos *et al.*, 2014). Key process parameters include the drag force induced by the crossflowing continuous phase, which shears the droplets as they inflate at the pore tips. Also the pressure applied to the disperse phase which directly affects the Laplace pressure (pressure difference inside and outside the growing droplet surface) and the dynamic lift and buoyancy forces of

the inflating droplet, which act perpendicular to the membrane surface (De Luca *et al.*, 2008). Figure 4.2 illustrates how these forces act on a growing droplet.

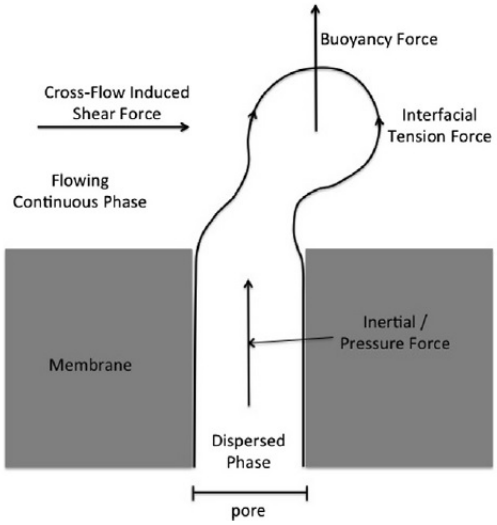

Figure 4.2: Forces acting on growing droplet from Hancocks *et al.* (2013).

On the micrometre scale, the influence of the inertial force of the disperse phase is typically negligible (Nunes *et al.*, 2013). This is known as the 'dripping' production regime where droplet detachment is induced by the shear force of the crossflow. There are two suggested models for droplet detachment in this case. The torque balance model implies that the droplet detaches once the torque is balanced at the foremost point of the pore circumference. Alternatively the force balance model takes into account the deformation of growing droplets in high shear stress environments. Here, droplet detachment occurs where the inclination angle of the deformed growing droplet is such that the interfacial tension can no longer counterbalance the Laplace pressure and the shear forces in particular (De Luca *et al.*, 2008).

Alternatively at high disperse phase flow rates where the inertia exceeds the interfacial tension, then the disperse phase may emerge as a 'jet' within the continuous phase. The disperse phase is pulled downstream as the droplet inflates thus it is elongated as pictured in figure 4.3. The elongated droplet eventually detaches from the membrane due to the viscous forces which oppose the deformation and create a 'pinch-off' (Nunes *et al.*, 2013). Essentially the droplet is pulled

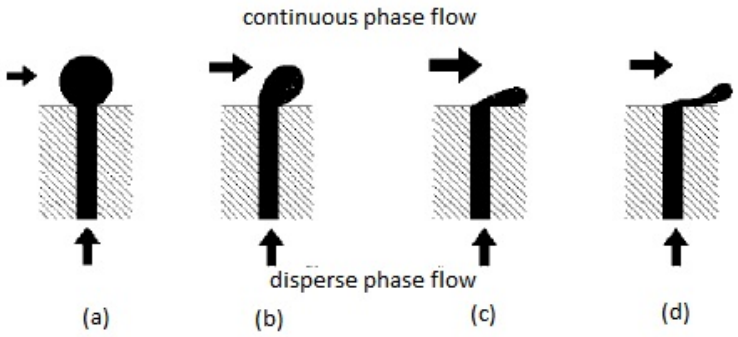

Figure 4.3: Droplet detachment scenarios; (a) negligible shear force, (b) shear force greater than interfacial tension, (c) low contact angle or high shear force, (d) membrane wetted with dispersed phase from Peng & Williams (1998).

further downstream before it detaches. Jetting typically generates polydisperse droplets due to Rayleigh instabilities, hence emulsions are not generally produced in this manner. However some groups have reported obtaining adequate conditions for producing monodisperse droplets smaller than the pore size in a jetting regime. This is mainly reported via microfluidic technologies with coaxial and T-junction geometries (Li *et al.*, 2015; Nunes *et al.*, 2013; Utada *et al.*, 2007).

The capillary number (Ca) and Weber number (We) of the continuous and disperse phases respectively, are often utilised to quantify the flow dynamics and thus provide an indication type of droplet production regime. The capillary number describes the fluid flow as a ratio of viscous forces to interfacial tension. The continuous phase capillary number Ca_c quantifies the balance of local shear stresses and capillary pressure at the pore tip. The relationship is summarised in equation 4.1 (Nunes *et al.*, 2013);

$$Ca_c = \frac{\mu_c \nu_c}{\gamma}. \tag{4.1}$$

Increasing capillary number indicates the increase of shear stresses experienced at the pore tip. Secondly the dispese phase Weber number (We_d) quantifies the balance of fluid inertia to capillary pressure. The relationship is summarised in

equation 4.2;

$$We = \frac{\rho_d D \nu_d^2}{\gamma}. \tag{4.2}$$

Increasing *We* infers the increasing dominance of inertial forces (Gu *et al.*, 2011; Nunes *et al.*, 2013; Peakall & Warburton, 1996). The capillary number of the continuous phase flow, and the Weber number corresponding with the disperse phase flow are often used in conjunction to predict the type of flow regime. A phase diagram, akin to the one presented in figure 4.4 is useful to visualise the balance between the two dimensionless numbers and the resulting flow. Typically in microfluidics transition to jetting can occur when capillary numbers are in the range of $\times 10^{-2}$ - 0.2×10^{-1} (Nunes *et al.*, 2013). Meyer & Crocker (2009) reported capillary and Weber numbers for an XME experimental set-up. Figure 4.4 also suggests a non-linear relationship in the transition between the two regimes at high Ca. Meyer & Crocker (2009) also suggest that for high Ca values $>10^{-2}$ where the cross flow velocity is high, the transition to jetting can occur at low Weber numbers $<10^{-2}$ as long as the membrane is not largely wetted by the disperse phase. This is especially likely when the droplet size to pore diameter ratio $\frac{D_d}{D_p} > 2$ (although it was not explicitly shown on the phase diagram).

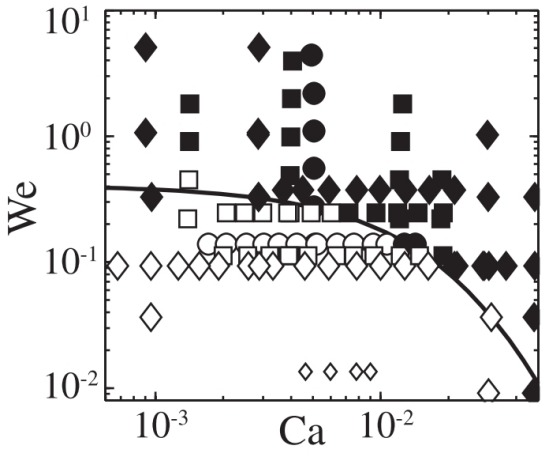

Figure 4.4: Phase diagram illustrating the transition between dripping and jetting regimes from Meyer & Crocker (2009). This diagram is a collation of data obtained via various microfluidic research groups. The solid line denotes the transition threshold.

Generally the crossflow velocity is dominant in controlling particle size especially in the dripping regime, where an increase in velocity results in smaller sizes owing to the increase in shear. In figure 4.5, Williams *et al.* (1998) depicts the decrease in size and the narrowing of the size distribution with increasing crossflow velocity. A slight increase in size with increasing transmembrane pressure is also shown. This is because the disperse phase flux is also increased. In the case where detachment time remains constant, it is possible for a slightly larger volume of droplets to form. This effect is more pronounced at lower crossflow velocities (Peng & Williams, 1998).

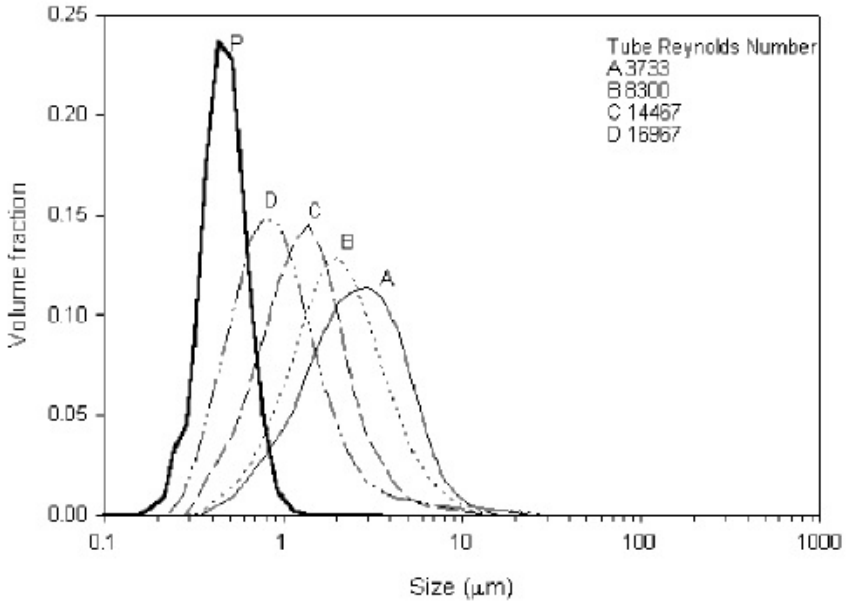

Figure 4.5: Effect of increasing crossflow velocity on the droplet size distribution (A, B, C, D) produced from a membrane having the pore size distribution (P) from Williams *et al.* (1998).

There are a number of additional parameters which require consideration to ensure a regular droplet detachment scenario and uniform size. One key formulation consideration is the emulsifier content dissolved in the continuous phase. An emulsifier lowers the dynamic interfacial tension of the growing droplet surface by adsorbing to it. This stabilises the droplets against coalescence and aggregation

both at the membrane surface and in the bulk emulsion (Joscelyne & Trägårdh, 2000).

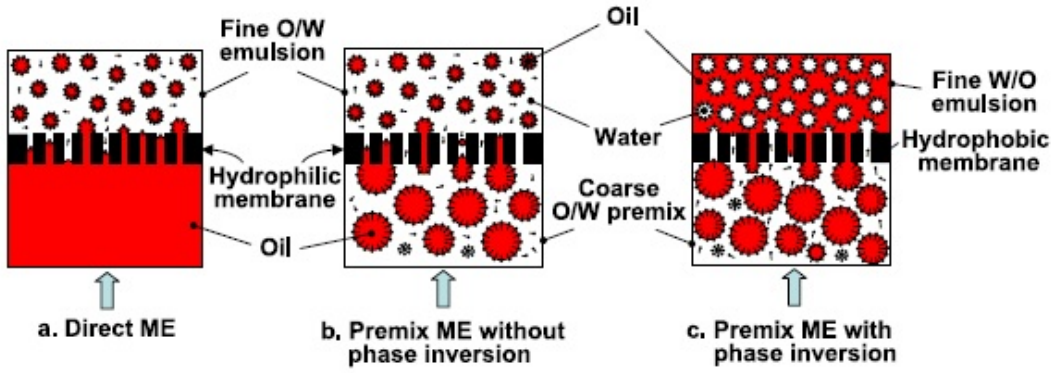

Figure 4.6: Processes for generating oil-in-water (O/W) and water-in-oil (W/O) emulsions via membranes from Vladisavljević & Williams (2005).

Other membrane related parameters include the size, morphology and uniformity of the pores. Typical droplet sizes range 2 - 10 times that of the pore size; usually from a few microns up to 100 microns (Gijsbertsen-Abrahamse *et al.*, 2004). Membrane porosity is influential such that in the case where a high number of pores become active, then pore spacing must be sufficient to prevent the coalescence of growing droplets or steric hindering of neighbouring particle growth (Williams *et al.*, 1998). The membrane wettability properties have significant consequences. As a droplet inflates at the pore tip and then detaches, it forms a spherical shape if shear force is less than interfacial tension (refer to figure 4.3(a)). However if the membrane surface is wetted by the disperse phase, then the shape of the growing droplet becomes elongated (see figure 4.3(d)) and the process transitions to jetting. Although interfacial tension returns the droplet to a spherical shape post detachment, distortion during the growth stage impacts droplets growing at neighbouring pores and the resulting size distribution (Peng & Williams, 1998). Thus a hydrophilic membrane is required to produce oil-in-water (O/W) emulsions and a hydrophobic membrane for water-in-oil (W/O) emulsions. Care

must be taken during production to ensure that the membrane is thoroughly wetted by the continuous phase before the disperse phase is injected. Hydrophilic membranes can be chemically treated to become hydrophobic although rapid desorption during emulsification is common, however there is a hydrophobic polymeric membrane option (Mi *et al.*, 2015).

Opportunely this concept can be exploited for the phase inversion of premixed emulsions. For example figure 4.6(c) illustrates how an O/W emulsion can be inverted to a W/O emulsion by pressing it through a hydrophobic membrane (Vladisavljević & Williams, 2005). Other opportunities include the production of multiple phase emulsions e.g. O/W/O and the homogenisation of coarse premixed emulsions as depicted in 4.6(b) (Vladisavljević & Williams, 2005). Essentially achieving a specific droplet size and size distribution, requires finding a balance and fine-tuning a complex array of physical and chemical parameters.

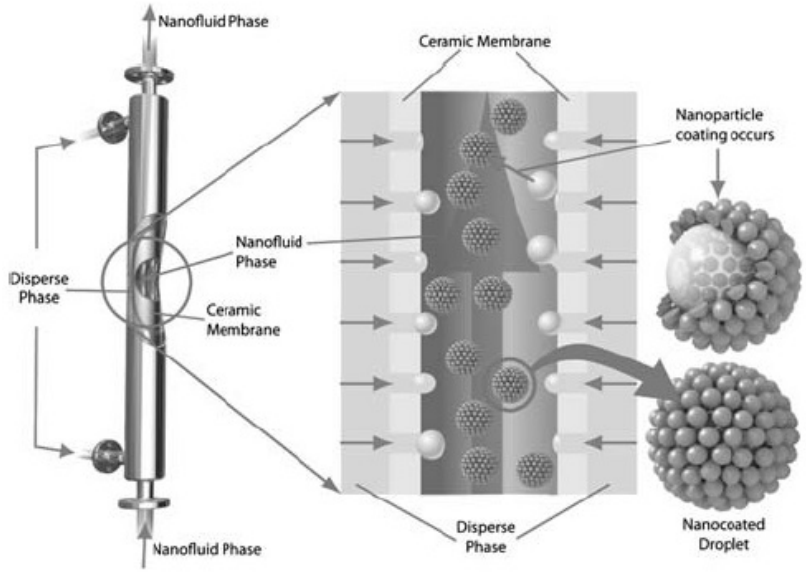

Figure 4.7: XME process illustration Yuan *et al.* (2010).

The original pioneering membrane emulsification method employs SPG membranes with a CaO-Al_2O_3-B_2O_3-SiO_2 composite structure. It is a laboratory scale set-up with typical membrane dimensions in the region of 10 ϕ (diameter) x 170 mm (Omi *et al.*, 2000). SPG emulsification has proven to produce emulsions with a very uniform droplet size distribution for kerosene (Nakashima *et al.*, 1992),

styrene (Omi *et al.*, 1994) and methyl methacrylate (MMA) (Omi *et al.*, 1995) for example. Although for MMA the authors implemented a two stage emulsification approach to avoid wetting of the hydrophilic membrane; whereby an emulsion comprising large hydrophobic droplets was prepared via SPG and subsequently mixed with an emulsion of small hydrophilic MMA droplets. This resulted in the diffusion of the unstable MMA droplets into the large stable droplets without affecting their size (Omi *et al.*, 1995). However in a subsequent report by the aforementioned authors, a one step emulsification was conducted. It is assumed that the membrane wettability properties may have been adjusted (Nuisin *et al.*, 2006) but it was not explicitly stated. One caveat of the SPG method is the low disperse phase volume fraction limit (typically 5 - 7%) of the emulsion. In comparison the production of polystyrene emulsions up to 20 vol% have been reported via metallic membranes (Wolska & Bryjak, 2009).

Peng & Williams (1998) and Williams *et al.* (1998) upscaled the ME process for industrial level manufacture via the XME approach which utilises a ceramic Al_2O_3-SiO_2 membrane. They developed a pilot-scale rig (Williams *et al.*, 1998) with membrane dimensions ϕ20x600 mm comprising seven continuous phase channels. The pilot-scale XME set-up can achieve relatively higher throughputs compared with SPG. For example disperse phase flux has been reported to be in the range of 50-250 $dm^3\,m^{-2}\,h^{-1}$ for a 0.2 µm membrane compared with 5-15 $dm^3\,m^{-2}\,h^{-1}$ via SPG (Charcosset *et al.*, 2004). XME is also more suited for high disperse phase volume fractions up to 30% (Williams *et al.*, 1998). Figure 4.7 is a schematic of the XME operational process. The disperse phase is outside the membrane and is pressurised through the membrane pores into the continuous phase channels. It is possible to have membranes with nominal pore sizes from 0.2-10 µm(Williams *et al.*, 1998). In their initial work, Williams *et al.* (1998) demonstrated the successful production of surfactant stabilised emulsions with monodisperse droplet size. In later work, Yuan *et al.* (2008, 2010) reported the production of monodisperse surfactant stabilised and particle stabilised oil and monomer emulsions, the latter is depicted in figure 4.7. Furthermore they compared XME to a typical homogeniser emulsification and reported the former technique to be far superior with respect to size uniformity (Yuan *et al.*, 2008, 2010).

4.2.2 Suspension Polymerisation

The emulsified monomer droplets are subsequently converted into solid polymer particles (beads) via heat-induced suspension polymerisation. In the case of an O/W emulsion, an oil-soluble radical initiator is already incorporated within the disperse phase during emulsification. Thus upon heating, the initiator breaks down to form radicals which initiate polymerisation within the droplets (Arshady & Ledwith, 1983). Figure 4.8 depicts a typical polymerisation sequence. Agitation of the emulsion is required to prevent settling or creaming, hence final particle size depends on droplet coalescence and break-up rates. A stabiliser can be incorporated in the formulation to prevent this so that the polymerised beads retain initial droplet size. Accordingly monomer volume fraction and stabiliser concentration are also key to particle size (Dowding & Vincent, 2000). Nitrogen bubbling is required since polymerisation is less rapid and more controlled in a deoxygenated environment. Generally if conditions are adequate, then suspension polymerisation enables good retention of droplet size characteristics (Dowding & Vincent, 2000).

$$\left.\begin{aligned} \mathrm{I} &\longrightarrow 2\,\mathrm{R}^{\bullet} \\ \mathrm{R}^{\bullet} + \mathrm{M} &\longrightarrow \mathrm{M}_1{}^{\bullet} \end{aligned}\right\} \textit{Initiation}$$

$$\left.\mathrm{M}_n{}^{\bullet} + \mathrm{M} \longrightarrow \mathrm{M}_{n+1}{}^{\bullet}\right\} \textit{Propogation}$$

$$\left.\begin{aligned} \mathrm{M}_n{}^{\bullet} + \mathrm{M}_m{}^{\bullet} &\longrightarrow \mathrm{M}_n\text{–}\mathrm{M}_m \\ &\longrightarrow \mathrm{M}_n(^{+}\mathrm{H}) + \mathrm{M}_m(-\mathrm{H}) \end{aligned}\right\} \textit{Termination}$$

Figure 4.8: Polymerisation Sequence from Brooks (2010).

Emulsion polymerisation is an alternative technique in which the initiator is incorporated within the continuous phase. Here the radicals form oligoradicals by attaching several monomer units. Once the oligoradicals are sufficiently hydrophobic they enter a micelle (an aggregate of surfactant molecules) and initiate polymerisation within. The polymer can increase in size by the diffusion of monomer droplets into the micelle (Cunningham, 2008). This process is typically

utilised for the production of particles within the nanometre size range. However with suspension polymerisation, the initial droplet size can be more readily retained (if conditions are adequate) since the polymerisation locus is within the droplet itself. This method is ideal for the production of particles within the micron size (Dowding & Vincent, 2000).

Numerous groups have demonstrated monodisperse particle syntheses via membrane emulsification and subsequent suspension polymerisation (ME-SP), where the polymer beads retained similar size characteristics to that of the initial droplets. Some of these data are presented in table 4.1. The coefficient of variation C_ν (previously introduced in chapter 2 equation 2.17), which corresponds with the ratio of standard deviation (θ) to mean size (μ), is a quantity that is typically used to quantify polydispersity by emulsification groups. C_ν values <35% are typically regarded as monodisperse and beyond this threshold polydispersity is inferred (Yuan *et al.*, 2008).

Table 4.1: List of monodisperse particle production and corresponding coefficient of variation .

Particle	Membrane	Size (μm)	C_ν (%)	Paper
Poly(styrene)	SPG	2 - 9	10	Omi *et al.* (1994)
Poly(methyl methacrylate)	SPG	3 - 35	10	Omi *et al.* (1995)
Poly(styrene-*co*-*N*-dimethylaminoethyl methacrylate)	SPG	6-10	10	Ma *et al.* (2001)
Poly(styrene-*co*-divinylbenzene)	metallic	23 - 34	-	Wolska & Bryjak (2009)
O/W microcapsules	XME	0.8 - 46	27 - 46	Yuan *et al.* (2008)
O/W microcapsules	XME	4 - 10	34 - 43	Yuan *et al.* (2010)
O/W microcapsules	rotating	80 - 500	10 - 35	Yuan *et al.* (2008)

Although table 4.1 demonstrates a breadth of research on ME-SP, the polymerisation stages were conducted on a small scale, <0.3 l even in the case of XME where 1-2 l of emulsion was manufactured. Therefore it was deemed pertinent to extend this research by testing the upscaling of the entire ME-SP. The novelty of the work presented in this chapter is the production of a monodisperse emulsion with a high volume fraction and subsequent suspension polymerisation on a relatively larger 2 l scale. This quantity was also appropriate with respect to the volume requirements for subsequent acoustic experiments.

4.2.3 Particle Aggregation

Another justification for the manufacturing of a latex particle suspension was to enable successive aggregation of the particles. Specifically, to observe differences in the acoustic response with respect to the initial non-aggregated state. Particles were suspended uniformly via agitation. Therefore a system with low density and correspondingly low settleability was preferential to avoid the requirement of high mixing rates, which could potentially shear aggregates.

The PMMA particles manufactured here were stabilised via steric and electrostatic mechanisms. Steric stabilisation is imparted by macro-molecules (typically a polymer) which attach to the particle surface via grafting or physical adsorption. They form an 'anchor' so to speak. Electrostatic stabilisation is imparted by the balancing of ionic charges between the dispersion and particles. In the steric case, aggregation can be initiated by decreasing the solvent power of the dispersion medium to the stabilising moieties. For example, in an aqueous dispersion, the addition of an electrolyte can reduce the solvency that water displays for the stabilising anchor polymer (Napper, 1983). Aggregation via the addition of an electrolyte is classed as coagulation. Flocculation is the term used where the process occurs via the addition of a polymeric electrolyte. The latter process usually forms a porous structure (Napper, 1983). Flocculation of a sterically stabilised suspension can be reversed via subsequent dilution which increases the solvent power of the dispersion medium, as long as the suspension has not been in a flocculated state for an extended duration. Coagulation of an electrostatically stabilised suspension on the other hand is irreversible due to

the strong van der Waal forces between aggregated particulates. Other methods to reduce the solvent power of the dispersion medium and invoke instability is via temperature and pressure change (Napper, 1983). There are a number of additional parameters which can influence aggregation behaviour. Although the extent of their individual influence is complex and can also depend on the role of other parameters present. Contributors include; particle concentration where dilute suspensions are generally more stable, particle size since large particles can induce stronger van der Waal forces, molecular weight and surface coverage of the stabilising moieties since low molecular weight and surface coverage result in greater instability, and the chemical nature of the disperse phase and anchor polymer (Napper, 1983).

4.3 Synthesis Experimental Methods

4.3.1 Materials Selection

The emulsification of Methyl Methacrylate (MMA) monomer via XME has been demonstrated without report of the disperse phase wetting the ceramic membrane (Yuan *et al.*, 2008, 2010), an occurrence which was suggested via the SPG membrane (Omi *et al.*, 1995), hence it was selected for the experiments here. Moreover the density of MMA ($0.9377\,\mathrm{g\,cm^{-3}}$ at $25\,^{\circ}\mathrm{C}$ (Haynes, 2015)) and the resulting polymer (PMMA) ($1.2\,\mathrm{g\,cm^{-3}}$ (Haynes, 2015)) are close to that of water which was desirable for the corresponding acoustic experiments. MMA (Sigma Aldrich, 30 ppm) was passed through an alumina column to remove inhibitors. Benzoyl peroxide [BPO] (Alfa Aesar, 25% moisture content) was added to the disperse phase as an oil soluble initiator. Figure 4.9 depicts the polymerisation sequence of MMA with BPO to form PMMA. Since the sintered ceramic (Al_2O_3-SiO_2) XME membrane is hydrophillic and could potentially be wetted by relatively hydrophillic substances such as MMA, Lauryl Alcohol [LA] (Sigma Aldrich, 98%) was incorporated in the oil phase to increase its hydrophicity as a preventative measure. Advantageously, diffusion between the oil droplets and the aqueous continuous phase is also negated (Ma *et al.*, 1999). However the ratio of LA co-surfactant to MMA requires careful consideration since Ma *et al.* (1999) found

that this affects the droplet morphology. LA needs to fully engulf the droplets to achieve stabilisation and subsequently produce spherical beads. The disperse phase solution comprising these three components was stored in a refrigerator prior to use.

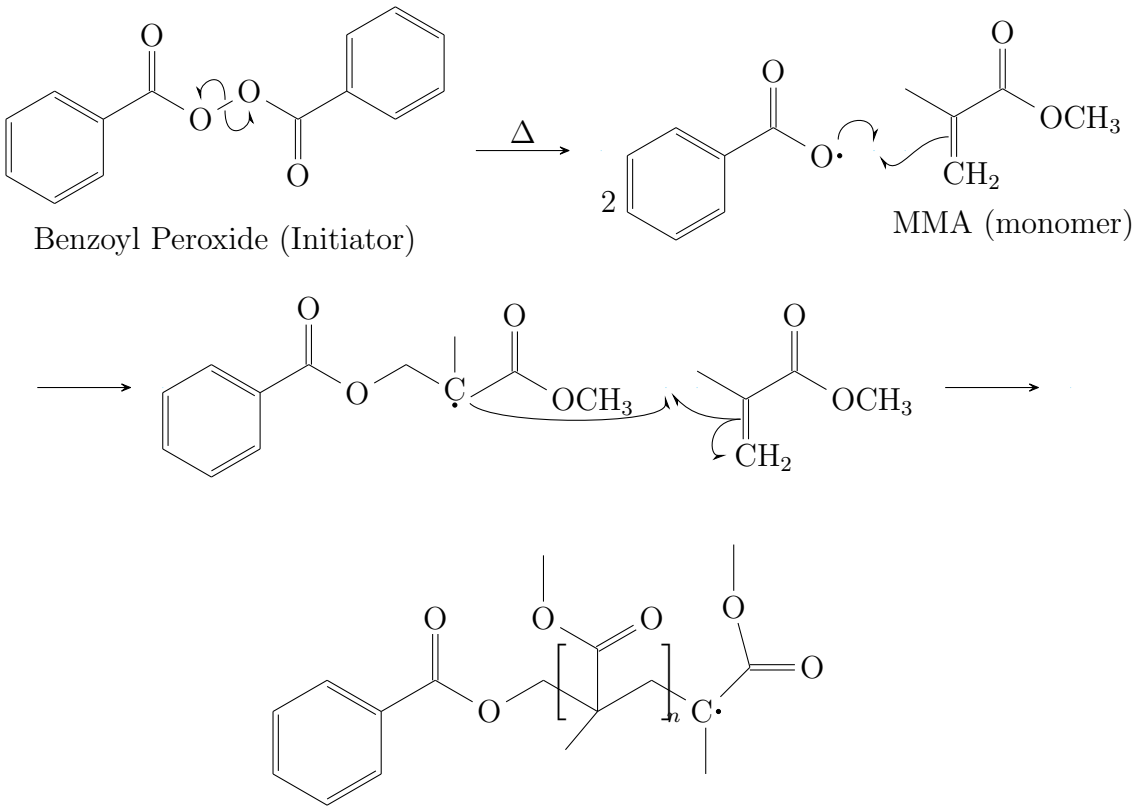

Figure 4.9: Polymerisation Reaction Mechanism Schematic.

The continuous phase primarily consisted of Millipore Milli-Q grade water. Other components included Mowiol (polyvinyl alcohol 8-88) [PVA] (Sigma Aldrich, degree of polymerisation $\sim 1,400$, 86.7 - 87.7 mol% hydrolysis, molecular weight $\sim 67,000$); sodium dodecyl sulphate [SDS] (Sigma Aldrich, 98%); hydroquinone [HQ] (Alfa Aesar, 99%) and sodium sulfate [SS] (Sigma Aldrich, 99%). PVA was used as the emulsifier providing steric stabilisation of the droplets growing at the membrane. PVA with 70 - 90% hydrolysis and molecular weight of $\sim 70,000$

is optimal as it has been shown to form a thick layer around the droplet which is unlikely to deadsorb. Below this range, PVA would increase the tendency towards coalescence, and above this range, destabilise to produce shapeless polymers (Brooks, 2010; Jahanzad *et al.*, 2005). SDS, an anionic surfactant, prevented coalescence in the bulk emulsion by means of electrostatic stabilisation (Joscelyne & Trägårdh, 2000; Wolska & Bryjak, 2009). HQ was incorporated as an inhibitor to prevent secondary nucleation in the continuous phase (Vladisavljević & Williams, 2005). Finally SS is a fairly unreactive salt so was incorporated to buffer electrolyte concentration.

Table 4.2: Formulation quantities of disperse and continuous phases respectively.

Chemical	Initial (wt%);[ab]	Final (wt%);[ab]	Typical Quantities [b]
MMA	31.2/-	15.8/-	-
BPO	0.6/2	0.3/2	0.1-0.5 wt% Dowding & Vincent (2000)
LA	1.6/5	0.8/5	5 wt% Omi *et al.* (1995)
Water	65.6/207	82.3/522.3	-
SDS	0.03/0.09	0.3/2	<CMC[c] to prevent emulsion polymerisation Dowding & Vincent (2000), 0.2 wt% Omi *et al.* (1994)
PVA	0.4/1.4	0.5/3.5	3 wt% Omi *et al.* (1995)
HQ	0.5/0.07	0	0.15 wt% Omi *et al.* (1995) & 0.003 wt% Ma *et al.* (2001)
SS	0.02/0.1	0	Omi *et al.* (1994)

[a] wt% with respect to total emulsion

[b] wt% with respect to monomer

[c] Critical Micelle Concentration

The quantities of each component are presented in table 4.2. The initial formulation presented here is an amalgamation of formulations devised by the various groups discussed. Notably the components and their quantities were adapted to suit the experimental requirements of the XME rig. Specifically the rig capacity for a single batch run is 0.5-1 l and 1-3 l of disperse and continuous phases respectively. During the course of the investigation, the polymerisation stage proved to be more challenging than expected. For example it was found that

the addition of HQ inhibited overall polymerisation rather than just secondary nucleation in the disperse phase. This result is discussed further in section 4.4.2. Hence it became necessary to conduct a series of experiments to determine optimal polymerisation conditions. Specifically a range of emulsions with formulation variations were manufactured and polymerised. The final reformulation is also presented in table 4.2, however the intermediary formulation stages are discussed later in section 4.4.2.

4.3.2 Emulsification

The XME pilot-scale rig developed by Williams *et al.* (1998) was employed for emulsification experiments here. As previously mentioned, a ceramic membrane was used with dimensions ϕ20x600 mm comprising seven continuous phase channels, with rig capacities ranging 0.5-1 l disperse phase and 1-3 l continuous phase. Figure 4.10 depicts the rig, its components and direction of the flowing phases. Initially the membrane was wetted with the continuous phase for 5 minutes to avoid wetting by the disperse phase. Wetting by the disperse phase could result in the activation of a small number of coarse pores leading to a bimodal size distribution, or jetting which could result in polydispersity (Joscelyne & Trägårdh, 2000). Subsequently the disperse phase was pressurised through the outer casing of the membrane, into the membrane and dispersed into each of the seven continuous phase channels.

Figure 4.11 presents images of the membranes employed and a micrograph depicting the tortuous network of interconnected pores. Since emulsified droplet diameter is typically in the region of 2 - 10 times that of the pore size (Gijsbertsen-Abrahamse *et al.*, 2004), both the 3 µm and 10 µm (largest pore size) membranes were selected with the aim of manufacturing particles within the 1-100 µm size range, in line with particle sizes of preceding ABS investigations of Titania (Bux *et al.*, 2015), Barytes (chapter 3) and spherical glass particles (chapter 2). Furthermore as discussed in chapter 1 section subsec:I.APM.Mech, since acoustic dissipation via thermal losses is dominant for soft particles, manufacturing large particles is preferable to ensure adequate measurable backscatter intensity in subsequent acoustic experiments.

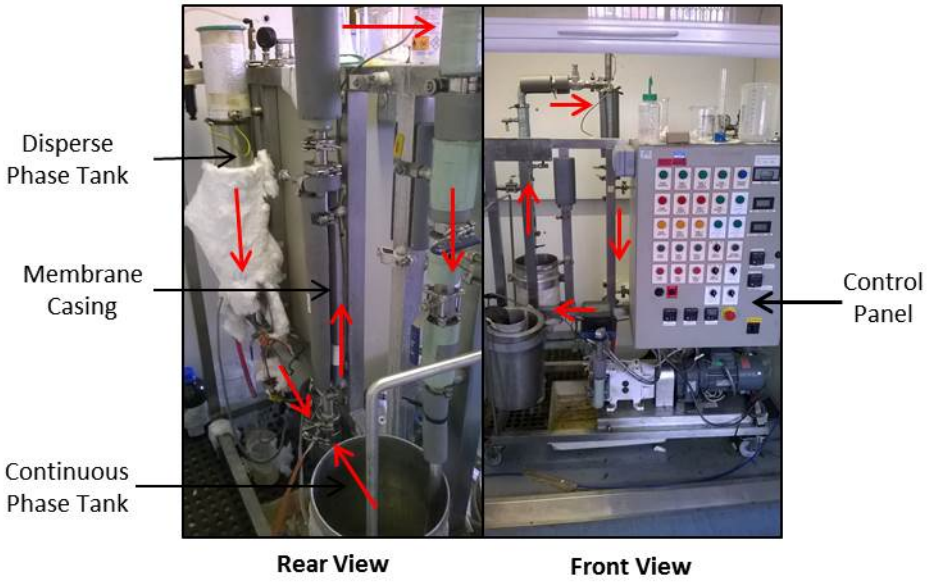

Figure 4.10: Photo of XME rig; red arrows indicate direction of flow.

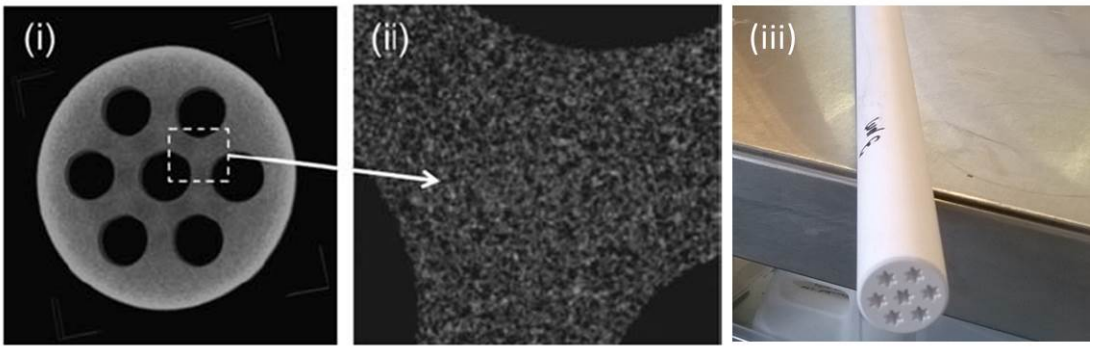

Figure 4.11: (i-ii) 10 µm tubular channel membrane with corresponding micrograph from Yuan *et al.* (2010) and (iii) 3 µm star channel membrane.

One aim of the emulsification was to achieve high throughput rates to enable rapid manufacture, whilst retaining monodisperse droplets. pressure adjustment was selected as the key variable in emulsification because disperse phase flux is

primarily responsible for throughput rates alongside pore size (Peng & Williams, 1998). The emulsification was conducted at a constant intermediate cross flow velocity $2\,\mathrm{m\,s^{-1}}$ ($560\,\mathrm{l\,h^{-1}}$) akin to the operating values used by Yuan *et al.* (2008, 2010), to ensure a reasonably narrow size distribution for acoustic experiments. The pressure was adjusted in the range 0.15-0.23 MPa (0.5-1.25 $\mathrm{bar_g}$), to fine tune particle size. The emulsions were recirculated for a further 2 - 5 minutes post emulsification to ensure homogeneity, especially in the case of rapid emulsification at higher disperse phase fluxes. The specific operational parameters are presented in table 4.3 in section 4.4.1 where the impact of their adjustment on emulsion droplet size is discussed in detail.

4.3.3 Suspension Polymerisation

Figure 4.12: Polymerisation apparatus; small scale Carousel-6 reactor and large scale 2 l reactor.

A two stage experimental approach was implemented in order to optimise the suspension polymerisation step. Initially 100-200 g samples of emulsion were polymerised in a Carousel-6 reactor with a Tornado overhead stirrer (Radleys Ltd., UK), depicted in figure 4.12. The samples were purged with nitrogen for 20

minutes to remove oxygen for controlled polymerisation. They were stirred at an intermediary rate of 200-225 RPM to prevent coagulation and droplet breakup (Arshady & Ledwith, 1983; Jahanzad *et al.*, 2005) and then maintained at 65 °C (initiator activation temperature). Polymerisation of the preliminary emulsion batch was unsuccessful, therefore a series of batch tests were conducted to determine the optimum balance of parameters. Specifically reaction duration was varied, alongside monomer volume fraction and surfactant, inhibitor and salt concentration. This required the production of several variations of emulsion. An extensive list of the experimental variations are presented later (section 4.4.2 table 4.4), where the corresponding results and strategies are discussed. Once the optimal formulation was achieved, polymerisation was upscaled to a 2 l reactor vessel with heated jacket and overhead stirrer, as pictured in figure 4.12. Similarly the emulsion was purged with nitrogen for 1 hour, stirred at 225 RPM and maintained at 65 °C for 8 hours. In both cases the samples were filtered with glass wool to remove coagulum generated in the stirrer region.

4.3.4 Droplet and Particle Characterisation

The emulsified droplet diameter was characterised via dynamic light scattering, specifically with the Malvern Mastersizer 2000 (Malvern Instruments Ltd., UK), operation of which was previously presented in section 2.3. Notably here it was necessary to disperse the emulsion in a water solution comprising surfactant to prevent droplet coalescence during measurement; 0.05 g of SDS was used per 100 g of MilliQ water. The stirrer speed of 1000 RPM was sufficient to suspend the droplets without inducing breakage or coalescence, i.e. no change in droplet size was noticed between successive measurements of a sample. Ten sequential measurements were made per sample and a minimum of three separate samples were measured per emulsion batch. This process was duplicated for particle size characterisation. However in the case of measuring aggregated particle diameter, it was necessary to reduce the stirrer speed due to aggregate breakage. The lowest setting which still enabled flow of the aggregated suspension through the measurement cell was selected. Nonetheless aggregate breakage was still observed

between successive sample measurements. Therefore these data only serve to provide an indication of initial aggregate size.

Particle size and shape were also characterised via scanning electron microscopy (EVO MA15 SEM, Carl Zeiss Ltd., UK), the technique of which is previously discussed in section 2.3. The SEM stubs were prepared with diluted samples and coated with a 15 nm 80/20 platinum /palladium coating. In addition particle concentration was determined gravimetrically. Samples were weighed wet, dried in an oven at approximately 70 °C for 24 hours and reweighed once dry to determine concentration from dry/wet ratios.

4.3.5 Particle Aggregation and Characterisation

Prior to aggregation, a systematic study was undertaken to determine the stability of the latex suspensions. Stability was inferred by means of their zeta potential measurement via the Malvern Zeta Sizer Nano ZS (Malvern Instruments Ltd, UK). Essentially a charged particle in suspension encompasses a layer of surrounding counter ions to neutralise the charge, called the Stern layer. Beyond the Stern layer, ions exist in the diffuse layer, these are not bound by the charged particle. Thus when a voltage is applied, a hydrodynamic shear is generated between the diffuse and Stern layers when the particle moves. Zeta potential measures this shear, from which the stability of the particle can be inferred. For example in the case where the particle is highly charged, the diffuse layer will have a tendency to move with the particle in order to neutralise the charge, hence the hydrodynamic shear will be low, indicating that the particle is unstable and the forces preventing it from flocculating are diminished. The zeta potential value is highly dependent on conditions of pH. One can identify the isoelectric point, the region of zero zeta where the particles readily aggregate by measuring zeta for a range of pH values.

Correspondingly, the isoelectric point was determined for 0.1 wt% PMMA samples at a range of pH levels. The pH was adjusted via the addition of 0.1 mol or 1 mol nitric acid or potassium hydroxide according to the requirement, and measured for a minimum of three times per sample with a Mettler-Toledo MP225 pH meter (Mettler-Toledo Ltd., UK). In addition, since electrolyte addition can

instigate aggregation, the particle stability was investigated at three salt concentration levels; 1×10^{-4} mol, 1×10^{-3} mol and 1×10^{-2} mol. Specifically potassium nitrate salt was employed to complement the ions incorporated from the acid and alkali addition. The zeta potential measurement parameters were as such; refrigerated samples were equilibrated to 25 °C for a two minute duration, three sub-samples were measured per solution with specific pH and salt concentration, three runs were conducted per sub-sample giving an average result compiled from 10 - 100 measurements depending on the consistency of the result.

4.4 Synthesis Results & Discussion

4.4.1 Emulsification Results

The droplet size distributions of the MMA emulsions prepared via XME are reported here. The operational parameters, resulting size distributions and corresponding C_ν values are summarised in table 4.3. Firstly figure 4.13 presents the droplet size distributions of the emulsions obtained via the 3 µm membrane. Specifically the influence of increasing pressure is demonstrated whilst the cross-flow velocity is kept constant at 1.8 m s^{-1}. This figure depicts an increasing trend in droplet size with decreasing pressure. The size distribution also becomes more polydisperse with decreasing pressure. C_ν progressively increases and exceeds the monodisperse threshold at the lowest pressure. Another notable observation is that the difference in C_ν is significant considering that the differences in the applied pressure are small.

As discussed in section 4.2.1, when droplets are produced in the dripping regime, pressure is not a significant influence on size because the inertia of the dispersed phase is never markedly higher than the Laplace pressure. Thus the shearing and interfacial forces primarily govern droplet growth and detachment (De Luca *et al.*, 2008). An increase in pressure generally results in only a slight increase in droplet size. This is due to the resulting increase in dispersed phase flux which enables the droplet to inflate to a slightly larger volume (note detachment time remains unchanged) (Peng & Williams, 1998). There is a breadth of work published on the production of droplets via ME in the dripping regime,

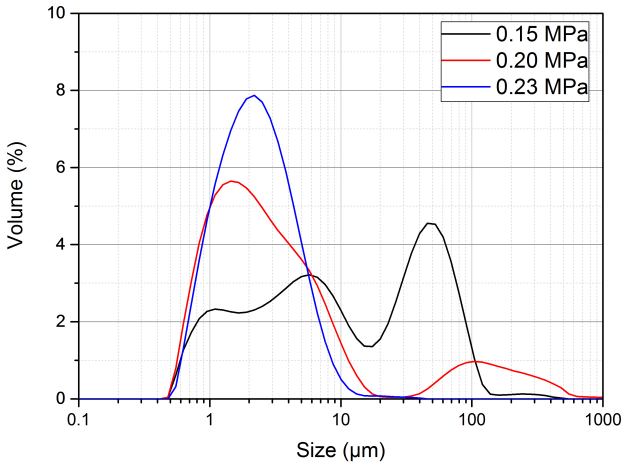

Figure 4.13: MMA emulsion; droplet size distribution with corresponding changes in pressure.

because uniform droplet growth and detachment renders monodisperse emulsions (refer to section 4.2 for extensive list). Interestingly this trend is not observed in the data presented in table 4.3 and figure 4.13, suggesting that the droplets may not have been produced in the dripping regime.

Table 4.3: Emulsification parameters and resulting droplet size, coefficient of variation, Weber number and Capillary number.

Pore Size (µm)	Pressure (MPa)	Disperse Phase Flux[a] ($l\,m^{-2}\,h$)	Continuous Phase Velocity ($m\,s^{-1}$)	D_{50} (µm)	C_ν (%)	We^b	Ca^b
3	0.15	273	2	13.3	85	-	-
3	0.20	684	2	2.5	18	-	-
3	0.23	3,650	2	2.0	7	2.3×10^{-3}	1.77
10	0.23	10,945	2	2.4	7	6.8×10^{-2}	1.77

[a] Calculated on the basis assuming a typical 5% pore activity (Lepercq-Bost *et al.*, 2010).

[b] Calculation assumes interfacial tension of $1\,mN\,m^{-1}$ based on SDS-water (Lepercq-Bost *et al.*, 2008).

The capillary and Weber numbers corresponding to the experiments here are presented in table 4.3. Note interfacial tension was assumed in the calculations as $1\,\mathrm{mN\,m^{-1}}$ based on SDS-Water continuous phase (Lepercq-Bost *et al.*, 2008). At the highest pressure used for the 3 µm membrane, the capillary and Weber numbers are 1.77 and 2.3×10^{-3} respectively, hence within the threshold for transition to jetting behaviour. Although values for the crossflow velocity and applied pressure are within the ranges previously published for this specific rig XME (Williams *et al.*, 1998; Yuan *et al.*, 2008, 2010), the membrane sizes of three and ten microns, are respectively one and two orders of magnitude larger than those previously employed at the given pressures. Naturally, larger pore channels do not require as much force to press the disperse phase flow through. The emulsification duration itself was extremely rapid, ranging 10-20 s, in the experiments here. Thus inferring high disperse phase flux and overall throughput rates. Hence it is plausible that the inertial force of the droplets became larger than the Laplace pressure and interfacial tension here, producing droplets in a jetting regime (De Luca *et al.*, 2008). Droplet size is significantly influenced by changes in disperse phase flux when in the jetting regime (Li *et al.*, 2015).

Interestingly the droplet diameter (2 µm) to pore size (3 µm) ratio is less than two in the present case. As discussed in section 4.2.1, transition to jetting behaviour is possible at low Weber numbers when this ratio is less than two (Meyer & Crocker, 2009), as in the present case. One must note that this type of analysis has not previously been conducted for the XME set-up specific for this rig. The XME set-up in the Meyer & Crocker (2009) experiments consisted of a small membrane with a single circular pore, which is a much smaller and less complex set-up than the large membrane with seven channels used here (refer to figure 4.11). Furthermore, as the disperse phase is pressed from outside the membrane and into the channels, it is likely that the dispersion into each of the seven channels is somewhat non-uniform. Therefore the Weber and capillary number values can only be taken as guidance and not definitive values for describing the behaviour in experiments here.

As seen in table 4.3, emulsification was also tested via a 10 µm membrane to maximise size. This was conducted at the highest pressure, in-line with the monodisperse emulsion produced at this pressure via the 3 µm membrane. For

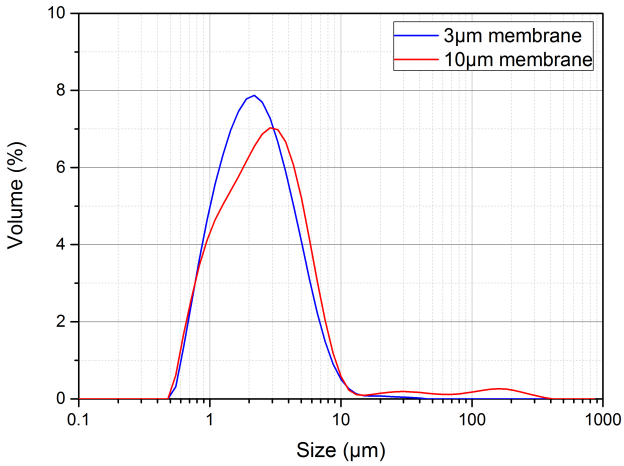

Figure 4.14: MMA emulsion; droplet size distribution with corresponding changes in nominal membrane pore size at 0.23 MPa.

comparative purposes, the corresponding size distributions are presented in figure 4.14. Interestingly, the 10 µm membrane produced a mean droplet size (D_{50}) similar to that via the 3 µm membrane. This result was surprising since it was expected that the larger pore size would produce larger droplets. Typically, mean emulsified droplet size via ME range 2 - 10 times that of the pore size (Santos *et al.*, 2015). However the correspondingly high Weber number of 0.03 indicates that production was well within the jetting regime threshold. Additionally jet diameter is independent of pore size, so a steady jet can have a very small diameter compared with the source (Nunes *et al.*, 2013), thus resulting in a small mean droplet diameter. Lepercq-Bost *et al.* (2008) reported that small droplets are produced at high capillary numbers. They suggested a Ca of 0.5 to be the threshold above which the droplet size produced is smaller than the pore diameter. Ca of 0.12 here is close to the suggested threshold determined via a membrane <1 μm comprising a single continuous phase channel. One other note when comparing the distributions via the two membranes is that the distribution of the 10 µm appears to be slightly broader than the 3 µm. Lepercq-Bost *et al.* (2010) reported pore activity to be in the region of 1-6 % for 0.2-0.8 µm membranes within pressure ranges comparable here. Pore activity quantifies the number of pores that

are activated, such that the dispersed phase flows through them during emulsification. Pore activity is generally enhanced with increasing pore size since the channels are more accesible. Therefore it is likely that in the 10 µm membrane case, there is greater pore activity as well as enhanced access to coarser and finer pores, thus leading to a slightly broader size distribution (Lepercq-Bost *et al.*, 2010).

Another notable observation in figure 4.13 which depicts the size distributions for three pressures via the 3 µm membrane, is that as pressure is reduced, the size distributions become increasingly polydisperse. Note all three distributions depict a primary peak in the 2-6 µm region, which approximately aligns with the expected droplet to pore diameter size ratio threshold $\frac{D_d}{D_p} > 2$ (Meyer & Crocker, 2009). In addition, a secondary peak is observed at larger sizes and a minor peak observed at lower size fractions. During jetting, the growing droplets have distended necks. The free energy of a droplet increases with deformation, hence a large elongation of the neck can result in a droplet snapping off in order to lower its free energy. In doing so, the droplet returns from an ellipsoid to a spherical shape. The snap-off can also result in the formation of a smaller secondary satellite droplet Spyropoulos *et al.* (2014). Hence the emulsion becomes more polydisperse due to the incorporation of a finer fraction of droplets. The elongated droplets can also span over several adjacent pores, generating coalescence events during the growth stage (Lepercq-Bost *et al.*, 2010). This corresponds with the significant large size fraction observed at the lowest pressure. Notably this peak is only exhibited at the lower pressures and recedes altogether with increasing pressure, since the time to detachment is less in the latter scenario, which reduces the likelihood for coalescence (Simons *et al.*, 2013). One can rule out wetting of the membrane by the disperse phase for the cause of polydispersity because a monodisperse emulsion is achieved at the highest pressure. If the membrane had been wetted by the disperse phase then the increased disperse phase flux at high pressure would have activated more coarse and fine pores and thus enhanced polydispersity (Joscelyne & Trägårdh, 2000).

The nature of the emulsifier and the correspondingly incorporated concentration is yet another factor that could have influenced the droplet size. In the case where it is incorporated in excess, then its adsorption to the droplet may be

such that the interfacial tension is rapidly stabilised and the droplet detaches at smaller sizes (Joscelyne & Trägårdh, 2000). Notably SDS is a fast adsorber and emulsifier (Berot *et al.*, 2003). Another notable point is that the XME operates as a recycling system, where the emulsion is recirculated to create a crossflow environment. There is potential here for additional shearing to reduce droplet size.

The experimental observations in this section highlight that there are numerous parameters which influence droplet size, primarily; crossflow velocity, transmembrane pressure, pore size, membrane wetttability properties and emulsifier nature and content, as discussed. But in addition there is the pore shape, membrane morphology, porosity, temperature, volume fraction and phase viscosities (Gijsbertsen-Abrahamse *et al.*, 2004; Wolska & Bryjak, 2009). This vast array of parameters renders size prediction to be a challenging task. The Weber and capillary numbers gave a good indication of the flow type, although comparison could not be made with data published for a like for like system. Notably here, a substantial volume of monodisperse emulsion with a high volume fraction was produced within the jetting regime, demonstrating perhaps an upper threshold for high throughput manufacture, and therein lies the novelty.

4.4.2 Polymerisation Results

The monodisperse emulsions produced at the highest pressure underwent suspension polymerisation; firstly in the small scale Carousel-6 reactor, and subsequently in the 2 L scale-up. The original emulsions produced via the 3 and 10 µm membranes in section 4.4.1, were unsuccessful. Figure 4.15 illustrates their discolouration and separation of the oil phase. The yellowish tinge is likely from the HQ component which is known to yellow when exposed to light for extended durations. Furthermore, the final polymer yield was low, in the range of 1-4 wt%. Consequently a series of experiments were conducted where various parameters were adjusted in order to achieve optimal polymerisation conditions. Table 4.4 provides a summary of the key variations and corresponding experimental observations.

Figure 4.15: Unsuccessful polymerisation attempts of MMA emulsions; 2×3 µm batches (left) and 2×10 µm batches (right).

HQ content was the first variable that was adjusted. It was incorporated to prevent secondary nucleation reactions within the continuous phase and hence aid the retention of monodispersity. However table 4.4 portrays an increase in polymer yield with reduction in HQ concentration. In fact the highest polymer content was achieved in the cases where HQ was removed from the formulation. Therefore the inhibition of polymerisation was not restricted to the aqueous continuous phase. Ma *et al.* (2001) and Simons *et al.* (2013) also reported a reduction in monomer conversion with the addition of HQ inhibitor. In the latter study 76 - 100 % reduction was reported. Therefore HQ was removed from the final formulation.

The second polymerisation was conducted in the 2 L reactor with HQ removed from the formulation. After the 6 hour mark, the suspension rapidly thickened, which resulted in the stoppage of the stirrer. The resulting suspension contained thick coagulum and a significant mass of solidified polymer. When an emulsion is gently mixed in a non-polymerising state, the monomer droplets can collide, coalesce and re-divide in a state of dynamic equilibrium. However at a certain stage in the polymerisation, also known as the sticky period (observed between 25-75% conversion), it becomes increasingly difficult for any coalesced particles to re-divide due to increase in viscosity from the increasing polymer content. Enhanced viscosity increases the frequency of collisions. If the partially polymerised droplets can be maintained in a state that prevents coalescence, for instance by reducing the agitation rate or incorporation of stabilisers or coagulation inhibitors, then the polymerising droplets gradually harden and become particles in suspension.

Table 4.4: Formulation variations for polymerisation experiments.

Batch	HQ (wt%) [a]	SS (wt%) [a]	SDS (wt%) [a]	Duration (hours)	Polymer (wt%) [b]	Dispersion Colour & Consistency
Initial 3&10μm	0.16	0	0.09	24	1-4	Beige & yellow emulsions with oily droplets (see figure 4.15)
3μm[c]	0	0	0.09	6	-	White emulsion thickened and solidified
3μm	0.16	0	2	24	12	Yellow separated emulsion with oil droplets
3μm[d]	0.07	0.03	2	24	16	Yellow separated emulsion with oil droplets
3μm	0.07	0.003	2	24	27	Very thick beige emulsion, coagulum eventually stopped magnetic stirrer
3μm	0	0	2	3	30	Thick white emulsion, solid lumps of coagulum eventually stopped magnetic stirrer
3μm	0	0	2	20	35	Very thick white emulsion, solid lumps of coagulum eventually stopped magnetic stirrer
Final 3μm[c]	0	0	2 [e]	6	14 [e]	White emulsion

[a] wt% with respect to monomer

[b] wt% with respect to total suspension

[c] polymerisation conducted in 2 L reactor

[d] repeat

[e] 1 part 30 wt% emulsion and 1 part continuous phase

Otherwise continued coalescence could result in coagulation of the entire monomer phase (Arshady & Ledwith, 1983), which was observed here. It was thought that the SDS concentration in the first two polymerisation trials may have been low therefore the SDS content was increased in subsequent polymerisation trials (refer to table 4.2).

Another notable point from table 4.4 is that in many of the trials, some thickening of the suspension was observed. It is thought that the high volume fraction of monomer was responsible for this. Most thickening was observed where polymer concentration was in the maximum region of 30 wt%. Typical

monomer volume fractions for suspension polymerisation are 0.1-0.5 because at higher fractions there may be insufficient space between droplets in suspension causing coagulation (Dowding & Vincent, 2000). To remedy this, the final large scale polymerisation was diluted to lower the monomer to suspending phase ratio. Specifically one part continuous phase was incorporated per one part of 30 wt% emulsion. The resulting polymerised suspension was less viscous.

Omi *et al.* (1994) reported the incorporation of SS salt in their formulation as a pH buffer. Therefore SS was trialled in some formulations, as presented in table 4.4, however no real benefit was exhibited thus it was negated from the final formulation. Variations in reaction duration were also trialed. The data in table 4.4 demonstrate that a 24 hour duration was not required to achieve good monomer conversion, therefore a shorter duration was adopted for the final reaction.

Images of the particles manufactured in the final large scale polymerisation trial are presented in figure 4.16. The SEM images depict the PMMA samples at varying magnifications. The images exhibit fairly monodisperse, smooth, non-porous beads. This type of bead is expected if the polymer is soluble in the monomer, as in this case. In the alternative scenario, rough porous beads are expected (Dowding & Vincent, 2000).

The size distributions of the emulsion and polymerised suspension are presented in figure 4.17. The PMMA particles have a D_{50} of 2.3 µm with 41% C_ν. The size is slightly larger but very close to the original droplet D_{50} of 2.0 µm (3% C_ν), thus inferring successful polymerisation conditions. It is expected in suspension polymerisation that the size of the polymer beads is approximately the same as the initial monomer droplets as long as adequate polymerisation conditions are achieved (Dowding & Vincent, 2000). However it is common for some coalescence to generate a bead size that is slightly larger than the initial emulsion droplet (Wolska & Bryjak, 2009). The MMA droplets exhibit an asymmetric distribution curve, whereas the PMMA consists of a primary peak in the 3 µm region, a minor peak in the submicron range and a very minor broad peak in the 20 µm region. However the overall span of both distribution curves is similar. Specifically in the submicron range, a distinct peak is formed which merges with the primary peak, however notably the volume fraction of particles in the submicron range is less

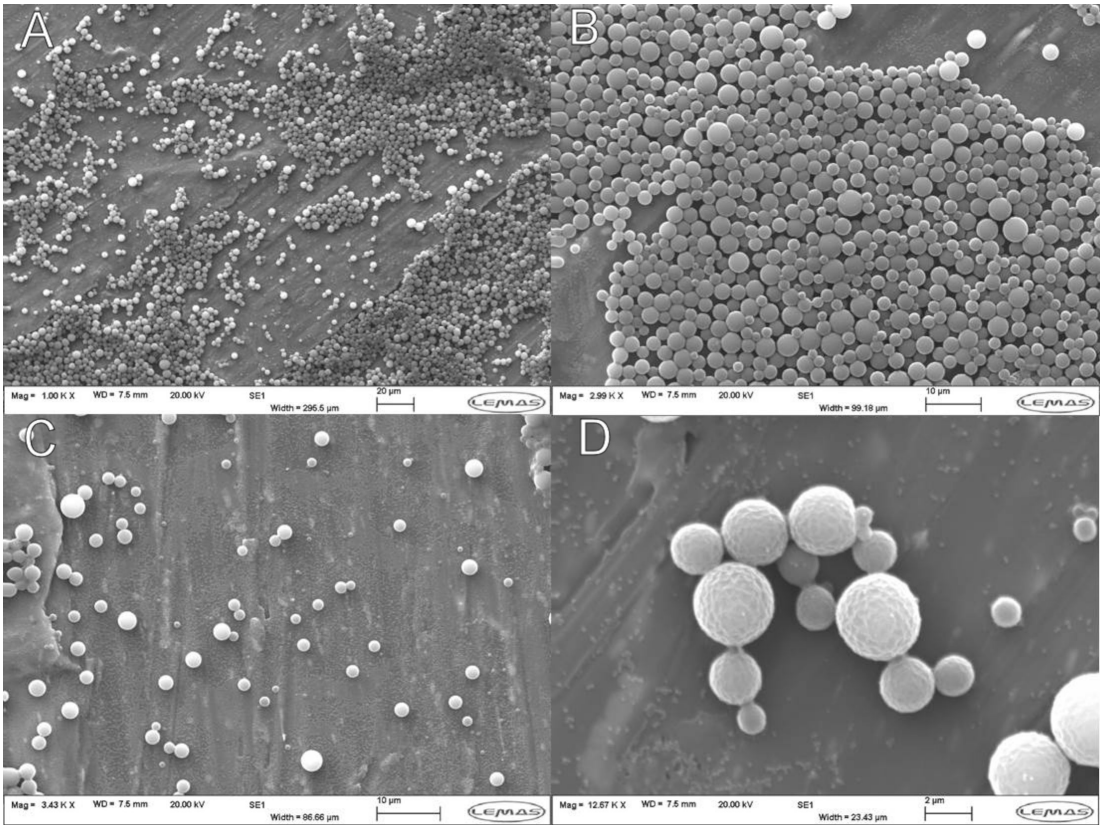

Figure 4.16: SEM micrographs of final polymerised particles; (a) sample 1 at x1,000 magnification, (b) sample 1 at x2,990 magnification, (c) sample 2 at x3,430 magnification and (d) sample 3 at x12,670 magnification.

than that of the droplets in that size range. One possible explanation for this is Ostwald ripening. This is the mechanism by which smaller particles reduce their interfacial tension by diffusing into larger stable particles (Simons *et al.*, 2013). A reduction in the submicron volume fraction and a slight shift towards the larger size fractions is indicative of Ostwald ripening.

It is common for coalescence to occur in this type of experimental set-up. The very minor peak in the large size range is indicative of coalescence events generating a few large particles. However in this case the volume fraction is reassuringly small. Another factor which may have influenced the size distribution is the surfactant concentration. MMA is sparingly soluble in water (1.5 g/100 mlH_2O

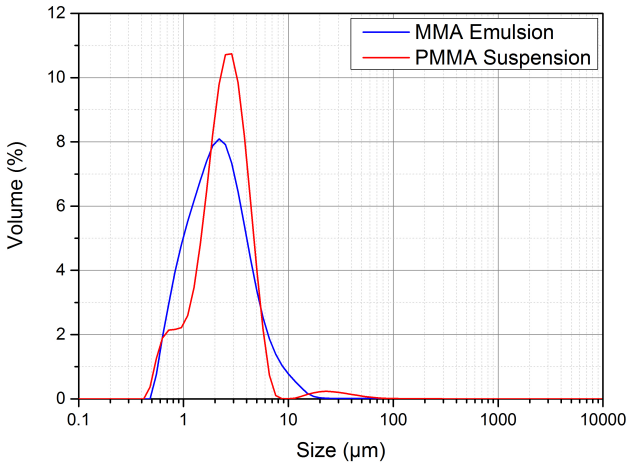

Figure 4.17: Size distribution of emulsion and subsequently polymerised suspension.

(Kricheldorf, 1991)). If some monomer diffuses into the aqueous continuous phase, then the chances of free radicals encountering micelles and initiating emulsion polymerisation within, is increased. This is more likely to occur when there are excess surfactant molecules aggregated in suspension. The corresponding secondary nucleated products would typically be in the submicron range (Simons *et al.*, 2013).

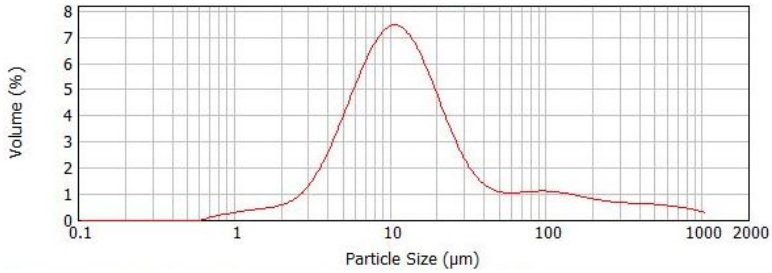

Figure 4.18: Size distribution of polymer beads produced via a typical high shear emulsification process and subsequent suspension polymerisation, Calum Furgeson, University of Leeds (2015).

For comparative purposes an alternative example of a common emulsification - suspension polymerisation process (conducted Calum Furgeson at the Univeristy

of Leeds) is provided. This typically involves emulsification via a high shearing process in order to disperse monomer droplets within the continuous phase. This is subsequently followed by a suspension polymerisation stage akin to the one conducted here. Specially emulsification was conducted at a shear rate of 5000 RPM and the suspension polymerisation at 300 RPM and 70 °C. The dispersed phase comprised 20 wt% MMA and Vazo 64 (AIBN) initiator, (monomer/intitator ratio = 318). The continuous phase; 3 wt% PVA and water, with overall emulsion volume of 50 ml. Figure 4.18 presents the particle size distribution of the resulting polymer beads. The corresponding size distribution is very broad inferring high polydispersity. This is primarily due to the random droplet breakage in the high shear environment in the emulsification stage. Then a high inhibitor to monomer ratio is used to prevent further polydispersity in the polymerisation stage. This highlights the robustness of the membrane emulsification - suspension polymerisation approach adopted in the present case.

To summarise, the finding of suitable suspension polymerisation conditions proved to be more challenging than anticipated due to the complex array of influential parameters involved. Careful consideration of chemical components and operational reactor conditions was required. Rather appropriately, Arshady & Ledwith (1983) gives the view that polymerisation is an art rather than a science. Simons *et al.* (2013) also state that production of stable particles via suspension polymerisation within the 1-50 µm range is challenging in the stirred tank set-up. Nonetheless a suitable emulsion formulation was realised via a series of polymerisation trials. This enabled the production of a 2 l quantity of monodisperse particles in a single batch run, which retained their originating droplet size characteristics.

4.4.3 Aggregation Results

This section reports on the stability and aggregation of the PMMA beads. Electrolyte addition is a common method for reducing the solvent power of the aqueous phase to the stabilising moieties (PVA in this case) (Napper, 1983). Therefore a series of experiments were conducted where the effects of salt addition were investigated with respect to the stability of the particles. Figure 4.19 portrays the

zeta potential variation with pH, of 0.1 wt% PMMA at three salt concentrations; 1x10^{-4} M, 1x10^{-3} M and 1x10^{-2} M KNO_3. All three salt concentrations exhibit the same trend, whereby the magnitude of zeta potential decreases with reduction in pH. This indicates that the particles are destabilised and likely to aggregate in regions of low pH. Note the isoelectric point was not reached although pH was adjusted to 2. This is perhaps unsurprising since the suspension comprises a surplus of SDS anions and negatively charged alcohol ions from PVA. Hence a significant amount of acid addition is required to neutralise the negative charge and reach the isoelectric point. Figure 4.19 also depicts a decrease in zeta potential magnitude with increasing salt concentration; 1×10^{-4} M, 1×10^{-3} M and 1×10^{-2} M respectively. At the highest salt concentration, the zeta variation with pH is minor, indicating that the particles would readily aggregate with sufficient addition of salt.

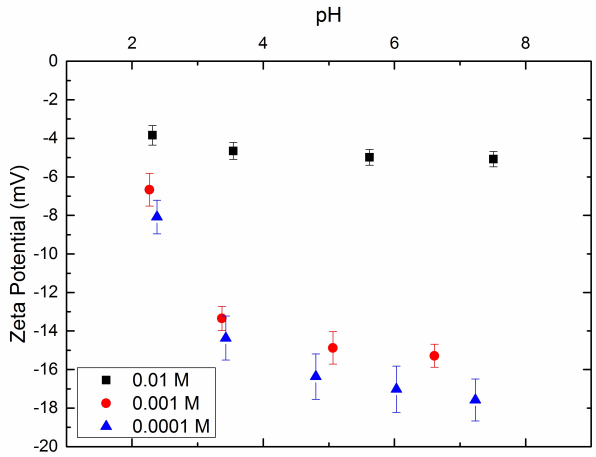

Figure 4.19: Zeta potential with varying salt concentrations; 1×10^{-4} M, 1×10^{-3} M and 1×10^{-2} KNO_3.

It was thought that the aggregation of particles could be somewhat hindered due to the steric stability imparted by the adsorbed PVA particles. Adjustment of temperature is another parameter than can initiate the onset of aggregation (Napper, 1983) therefore the effects of temperature variation were briefly investigated. Figure 4.20 portrays 15 wt% PMMA samples at the three salt concen-

trations post heating to 30 °C for a 30 minute duration. This image shows the aggregation of the 1x10^{-2}M sample (highest salt concentration). Particle concentration is yet another parameter that can influence aggregation behaviour, where suspensions with high particle concentration aggregate more readily due to the increased frequency of collisions. Taking these factors into consideration, a 5 wt% PMMA sample was selected for aggregation via the addition of 1 M KNO_3 salt concentration. The sample was not heated due to the large 1.5 L quantity that was to be utilised for acoustic experiments, however the influence of heating on aggregate size was briefly investigated. The size distributions of no salt addition, salt addition and salt addition with 30 minute heating at 30 °C are compared in figure 4.21. The average size, coefficient of variation and span of the distributions are also presented in table 4.5 for comparative purposes.

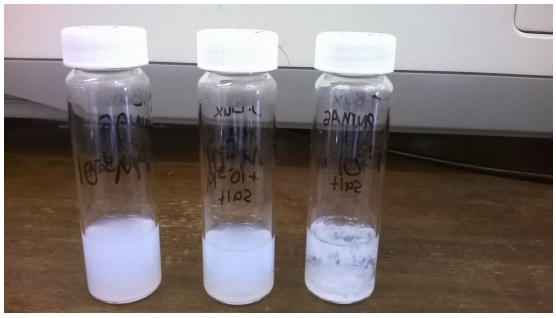

Figure 4.20: Aggregated suspensions at varying salt concentrations; 1×10^{-4} M, 1×10^{-3} M and 1×10^{-2} M KNO_3 (left to right).

Figure 4.21 and table 4.5 exhibits an increase in diameter in the cases where salt has been added, thus inferring successful aggregation of the PMMA particles. The coagulation process involves the destabilisation and the collapse of the thin steric layer around the particles. Furthermore the size of the particles which make up the aggregate are within the colloidal region. For these reasons it is likely that a fairly well bound aggregate structure is formed with low porosity. However the data in figure 4.21 only serve to provide an indication of initial particle size because aggregate breakage was observed in successive size measurements, due to the shear in the Mastersizer measurement cell. This indicates that the aggregate structure is loosely bound. Generally at larger sizes, flocs are generated. These

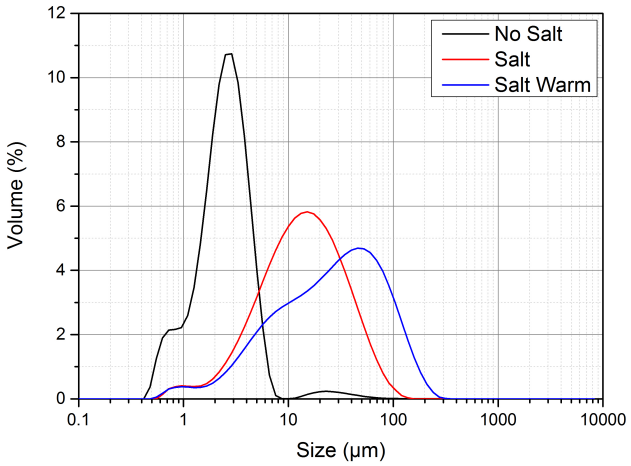

Figure 4.21: Size distribution of coagulated samples compared with the initial dispersion

are a looser form of aggregate where the particles are held together relatively far apart in a porous structure (Napper, 1983). There are many variables to consider in the aggregation process. Particles which have strong interactions tend to stick and form porous structures. Particles with weaker interactions can rearrange upon collision and eventually form closely packed denser aggregates. The size of the aggregate also depends on the particle size, concentration and aggregation kinetics. Furthermore it is not necessarily the case that all particles in a dispersion aggregate (Austin & Challis, 1998). In this case since the particles are colloidal in size they are likely to form closely packed aggregates. However since the dispersion incorporates strong ionic interactions, it is also plausible that they formed porous structures. Unfortunately it was not possible to visually verify the aggregate structure in the present case.

The measured aggregate diameter of the coagulated sample that also underwent heating is further increased, suggesting enhanced aggregation. Upon comparison of the warmed and non-heated coagulated dispersions, it is clear that the particles have not aggregated to their full extent in the latter case. It is likely that a temperature increase enhanced coalescence generating a larger size in former case.

Table 4.5: Aggregation size distribution data including mean size, coefficient of variation and span of the distribution.

Suspension	D_{50} (μm)	Cν (%)	Span
No Salt	2.3	5.1	1.4
Salt	12.9	7.4	2.8
Salt Warm	25.6	5.9	3.4

4.5 Particle Synthesis Summary

Sections 4.2 - 4.4 outlined a novel high throughput manufacturing process for monodisperse emulsions and latex particles on a large (2l) scale. The two step process involved membrane emulsification to generate a monomer emulsion and subsequent suspension polymerisation to convert the emulsion into a latex bead suspension. Although the two techniques themselves are well known, some important advancements were made in the work reported here. Typically membrane emulsification is performed in the dripping regime to ensure droplet monodispersity. Droplets generating via jetting are typically polydisperse. However in this work, monodisperse droplets were generated in a 'controlled' jetting scenario, whereby suitable emulsions with high volume fraction were manufactured rapidly. This has implications for enhancing throughput dramatically, which is of particular interest on an industrial scale.

Secondly in the laboratory, suspension polymerisation is generally conducted on a <0.3l scale. Achieving adequate conditions to produce latex beads which retain their initial droplet characteristics is somewhat challenging. However successful suspension polymerisation on a 2l scale was demonstrated in which the resulting beads retained the initial droplet size characteristics. Albeit the process proved challenging such that several emulsion reformulations were required to achieve optimal polymerisation results. Finally, the stability of the latex beads was also investigated and they were subsequently coagulated via electrolyte addition to form aggregates for subsequent acoustic investigations.

4.6 Latex Acoustics Experimental Methods

In the final body of work, ABS investigations were implemented for the comparison of the acoustic response of a monomer emulsion, the corresponding polymer suspension and the aggregated dispersion. Experiments were conducted in line with the general ABS methodology prescribed in sections 2.2 - 2.3, although with a few alterations. Since the volume of available emulsion and dispersion was restricted to 1-2 l, experiments were conducted in a smaller rig pictured in figure 4.22. The column with dimensions 0.11 m x 0.33 m was placed on a magnetic stirrer plate and mixed at speed 7 from a selection of 10 speed levels. In some cases it was possible to profile a 0.2 m depth which provided enough data within the far-field region. However in some high concentration scenarios, it was only possible to profile up to a 0.1 m depth, in which case the normalised near-field data was incorporated in analysis. The profiled emulsions and dispersions are listed in table 4.6. The Latex dispersion was aggregated and then diluted to obtain a range of concentrations listed in the table. This approach was taken to ensure constant aggregate size in all experiments to enable direct comparability of results. 1 x 1 MHz, 2 x 2 MHz and 1 x 4 MHz frequencies were utilised at a pulse rate of 32 Hz in 2.5 mm bins. An average backscatter intensity was obtained via 3 x 10 minute runs per frequency.

4.7 Latex Acoustics Results & Discussion

Experimental results of sound propagation in monomer emulsions and the corresponding aggregated and non-aggregated polymer dispersions are reported here. Note that the polymerised dispersions were used as is, so the manufactured polymer beads were not precipitated out of the SDS suspension and re-suspended in water. In this way, the suspending phase of the emulsions and particle dispersion were identical enabling direct comparison of ABS results. Referring back to the dispersions zeta potential data in figure 4.19, the polymer particles were fairly unstable across the pH range that was investigated, so the electrostatic stabilisation imparted by the SDS surfactant in suspension was required in this case. If we refer back to the emulsion formulation (table 4.2), the emulsion droplets

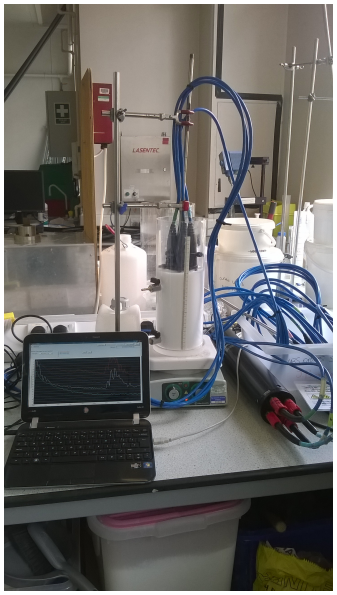

Figure 4.22: Latex acoustics experimental set-up.

Table 4.6: List of profiled emulsions and dispersions.

Type	Concentration ($kg\,m^{-3}$)	Concentration (wt%)	Depth (m)
Monomer Emulsion	14.8	1.5	0.2
	50.3	4.8	0.1
	113.1	10.1	0.1
Polymer Suspension	3.0	0.3	0.2
	12.0	1.2	0.2
	21.0	2.1	0.2
	44.7	4.3	0.2
	87.9	8.1	0.2
Aggregated Polymer Suspension	3.0	0.3	0.2
	21.0	2.1	0.1

were also stabilised sterically via the addition of PVA (a soft Latex), which adheres to the droplet surface. It is also likely that some PVA molecules would be attached to the polymer particle surface also. The PVA would likely be in one of two orientations, either sticking out of the particle or wrapped around the

particle somewhat. The latter case is likely where a low concentration of PVA is utilised and would form an effective sphere around the particle of approximately 10-20 nm thickness. This would not likely alter the acoustic response of PMMA Latex significantly.

4.7.1 Latex Dispersion Profiles

Initially, the acoustic profiles and properties of the non-aggregated PMMA Latex dispersions are discussed. The backscatter profiles with respect to transducer range are presented in figure 4.23. Average intensity in decibels are given for 1, 2 and 4 MHz in A-C respectively. The corresponding G profiles are given directly below each frequency D-F. Note that the column base is located at approximately 0.15 m and the near-field focus point in each case is indicated with a vertical dashed line. The concentrations 3-88 kg m^{-3} correspond with 0.3 - 8.1 wt% (refer to table 4.6).

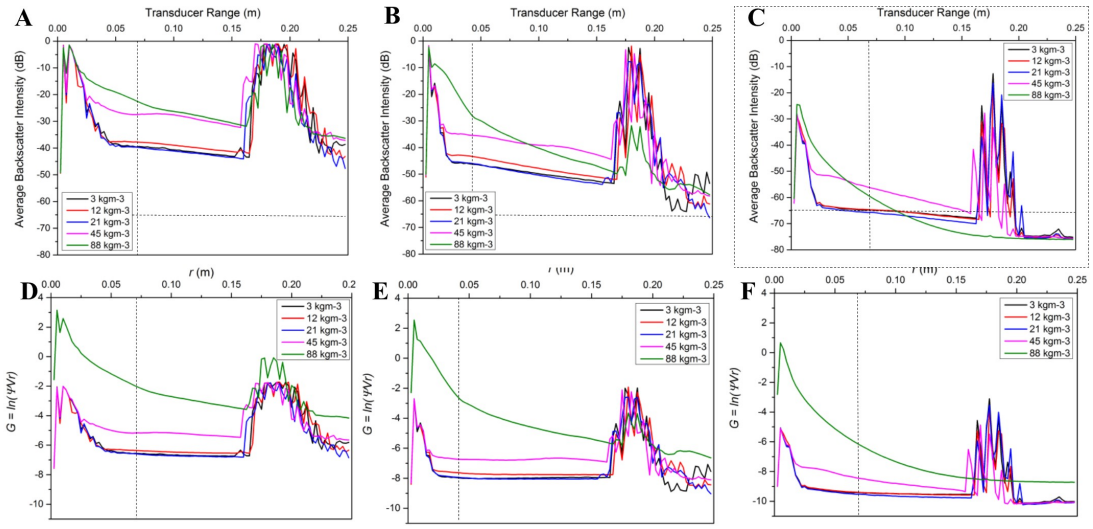

Figure 4.23: Latex backscatter against transducer range for all concentrations; decibel profiles via (a) 1 MHz, (b) 2 MHz and (c) 4 MHz, and corresponding G profiles via (d) 1 MHz, (e) 2 MHz and (f) 4 MHz

Interestingly, the general backscatter intensity and the associated signal de-

cay is markedly weaker than that which has been reported for rigid Honite and Barytes particles in sections 2.4.1 and 3.2.2 at similar concentrations. The G profiles are fairly flat up until the highest concentration. This feature is attributed to the size and density of the PMMA particles. Firstly the diameter (2.3 µm) is much smaller than that of Barytes (7.8 µm) and Honite (40.5 µm and 78.9 µm). Therefore the scattering cross-section of the Latex is smaller, resulting in a weaker backscatter amplitude. The density of the Latex is also low (1180 $\mathrm{kg\,m^{-3}}$) rendering it a softer and more compressible particle than Barytes (4418 $\mathrm{kg\,m^{-3}}$) and Honite (2453 $\mathrm{kg\,m^{-3}}$ and 2469 $\mathrm{kg\,m^{-3}}$) which are denser rigid particles. The dominating interactions of an ultrasonic wave incident on a soft particle differ from those on a rigid particle. Where the density contrast between the fluid and the particle is low, but the thermal properties of the phases differ, a temperature gradient is generated at the particle surface due to pressure-temperature coupling, thus causing heat flow and dissipation of acoustic energy around the particle surface (Dukhin & Goetz, 2001). This so called thermoacoustic scattering is enhanced with decreasing particle size (Challis *et al.*, 2005; Hazlehurst *et al.*, 2014), and therefore is the dominant scattering effect in the 2.3 µm Latex dispersion here, (refer to chapter 1 section 1.3.1 for discussion on scattering mechanisms). For these reasons, the reflected pulse energy of the Latex is markedly weaker. Again when comparing the magnitude of backscatter intensity and attenuation with that of colloidal titanium dioxide (density 3900 $\mathrm{kg\,m^{-3}}$) of similar size and concentration from Bux *et al.* (2015) (chapter 1 section 1.4.2), Titania backscatter profiles exhibit much greater intensities and intensity decay due to visco-inertial effects dominating scatter of rigid particles <3 µm in size. Therefore it is clear that losses from visco-inertial effects are negligible in the Latex case due to the low density contrast.

The stark contrast in the gradient of the curves when transitioning from the near-field to the far-field, is another notable feature. This is especially pronounced in the G function profiles in figure 4.23D-F. This has not previously been observed in other investigated dispersion systems, which were either viscous or scattering attenuators. Therefore, this feature must be attributed to the thermal attenuating properties of the Latex particles.

The Latex profiles do however depict some general characteristics seen in backscatter profiles of rigid particle dispersions, with respect to concentration and frequency; although these features are not as prominent and do not necessarily arise from the same effects. Firstly, an increase in intensity and signal attenuation is observed with increasing concentration. This has been observed before with both Barytes (chapter 3 figure 3.5) and Honite (chapter 2 figure 2.6), where the scattering intensity is naturally enhanced with the increasing concentration of scatterers in the dispersion. This also results in a more rapid extinction of the signal owing to enhancement of inter-particle scattering deviating reflected waves from their path back to the transducer (Bux *et al.*, 2015; Hunter *et al.*, 2012b). Interestingly, this particular effect is only observed at the two highest concentration profiles of the Latex dispersions, from 4wt%. There is not an appreciable difference between the lowest concentration profiles which exhibit a very weak scatter and no clear trend with concentration. It is likely that by ∼4wt% the critical volume fraction has been exceeded. This is the volume fraction at which the thermal layers of neighbouring particles begin to interact and overlap, mediating heat flow which reduces the temperature gradient at any one given paticle. A reduction in overall attenuation via thermal losses, is the primary consequence of networked particles (Challis *et al.*, 2005; Hazlehurst *et al.*, 2014), (refer back to chapter 1 section 1.3.1 and 1.5). This is likely the reason why the profiles exhibit a sudden increase in intensity at higher concentrations >4wt%.

The thickness of the thermal layer is proportional to the reciprocal square root of frequency (see chapter 1 equation 1.2, hence a low frequency gives rise to a longer thermoacoustic wave, enhancing the thermal overlap and reducing overall attenuation via thermoacoustic scattering (Challis *et al.*, 2005; Hazlehurst *et al.*, 2014). So overall intensity is expected to decrease with increasing frequency. This was indeed observed in figures A to C, where overall profile intensity diminished with increasing frequency; 1, 2 and 4 MHz respectively. Accordingly, the base column peak is no-longer visible at 8 wt% via the 4 MHz.

These results indicate that although the ABS may not be most ideal for characterising soft colloidal particle dispersions with low volume fractions, they are

in fact measurable. This further highlights that it is possible to obtain backscatter intensity profiles of soft particles at much higher concentrations than rigid particles, which makes it very ideal for commercial applications.

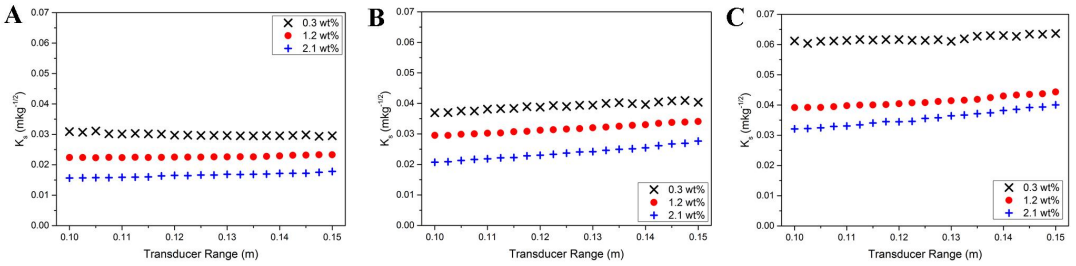

Figure 4.24: Latex Ks profiles with respect to transducer range via (a) 1 MHz, (b) 2 MHz and (c) 4 MHz.

Table 4.7: PMMA backscattering constants and corresponding standard deviation.

Frequency (MHz)	Ks	σ
1	0.023	0.007
2	0.032	0.008
4	0.046	0.014

The profiles in figure 4.23 depict a dramatic transition in attenuation between the near-field and the far-field regions, hence only data from 0.10-0.15 m are utilised for analysis purposes going forward. First the gradient of the G profiles $\frac{dG}{dr}$ were plotted against concentration in order to determine the sediment attenuation constant as per the Rice method (chapter 1 section 1.4.3). This is discussed later in figure 4.28 where the sediment attenuation constant is compared for all three emulsion/dispersion systems. The measured ξ was then utilised to estimate the back scattering constant using equation 1.4 and Kt measured in chapter 2 section 2.4.3. The estimated Ks is plotted against transducer range in figure 4.24 for each frequency. The Ks values at each concentration for 1 MHz are constant with respect to distance and are in reasonable proximity, although there is greater variability at the higher frequencies, which had a much weaker

signal. The distance averaged backscattering constant for each frequency is listed in table 4.7. Notably, in ultrasonic spectroscopy, which is the primary field in which scattering of latexes has been studied, the techniques typically measure acoustic attenuation and infer particle size from this measurement. Hence various groups have derived attenuation coefficients for Latexes (Dukhin & Goetz, 2001; McClements, 1991; Tebbutt & Challis, 1996) but little work has been done to derive backscattering constants, as presented here.

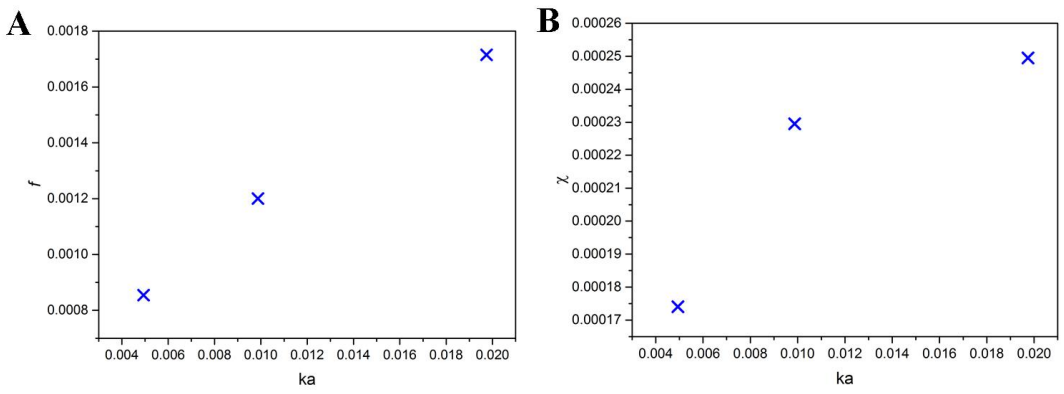

Figure 4.25: (a) Form function and (b) total normalised cross-section versus *ka* for PMMA particles.

Likewise very little is known about how well the heuristic form function and total scattering cross-section equations describe scattering effects at low *ka* values (Vincent & MacDonald, 2015). From the measured χ and Ks it was possible to determine the form function and total scattering cross-section for the Latex particles. These are depicted in figure 4.25. f and χ, and have not previously been determined for Latex particles. These data are invaluable in beginning to understand scattering influences in the low *ka* region, and indeed there is little data in literature for f and χ at such low *ka* values (Betteridge *et al.*, 2008; Moate & Thorne, 2012; Thorne & Meral, 2008; Thorne *et al.*, 1993).

4.7.2 Emulsion Profiles

Next the backscatter response of the dispersion is compared with the associated emulsion here. The average backscatter decibel profiles of a 1.2 wt% dispersion are compared with a comparable 1.5 wt% emulsion in figure 4.26 for all frequencies. Note the particle and droplet sizes are 2.3 µm and 2.0 µm respectively. Figure 4.26 portrays a small systematic reduction in echo intensity in the case of the emulsion with respect to the dispersion. The density of emulsified droplets (0.94 g cm^{-3}) is marginally less than that of the dispersed polymer beads (1.18 g cm^{-3}) hence the droplets are more compressible than the particles, hence a reduction in reflected intensity is expected due to marginally greater energy loss from thermal scattering. As expected the intensity also recedes with increasing frequency. The influence of particle density on sound propagation within dispersions is examined further in chapter 5 where data from all measured particle systems from chapter 2-4 are compared. Note the emulsion and suspension data appear to converge at 0.06 m, however these data are within the near-field regions and were not utilised during analysis.

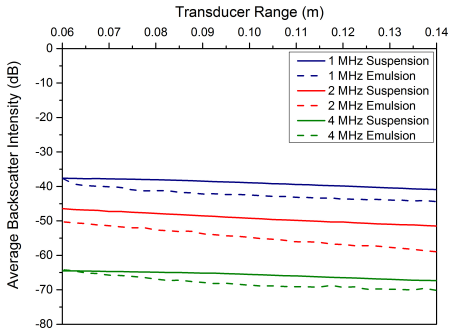

Figure 4.26: Backscatter comparison of monomer emulsion (1.5 wt%) with polymerised suspension (1.2 wt%) at 1, 2 and 4 MHz.

4.7.3 Aggregated Dispersion Profiles

The latex dispersions were aggregated as described in section 4.4.3 to a nominal size >15 µm. The aggregated dispersion backscatter profiles in decibels are

presented for 0.3 and 2.1 wt% via 1, 2 and 4 MHz figure 4.27 A-C respectively. The corresponding non-aggregated dispersions are also depicted at each concentration. The profiles in figure 4.27 depict a marked increase in both intensity and attenuation in the aggregated case. This is partly attributed to the increase in size by an order of magnitude in the aggregated case, so naturally the scattering intensity is enhanced. An increase in size also enhances overall attenuation of the backscattered pulse somewhat since the larger scattering cross-section enhances scattering of the pulse at angles other than 180°. In the aggregated case, the close proximity of the particles would also cause thermal layer overlap between adjacent particles, thus reducing overall attenuation and enhancing the backscatter intensity with respect to the non-aggregated case. When comparing the aggregated profiles, the highest concentration scenario is most attenuated. This corresponds with the enhancing of inter-particle scattering events with concentration, receding the echo intensity (Hunter *et al.*, 2012a). The profiles indicate that signal decay between concentrations is perhaps dominated by scattering effects rather than thermal.

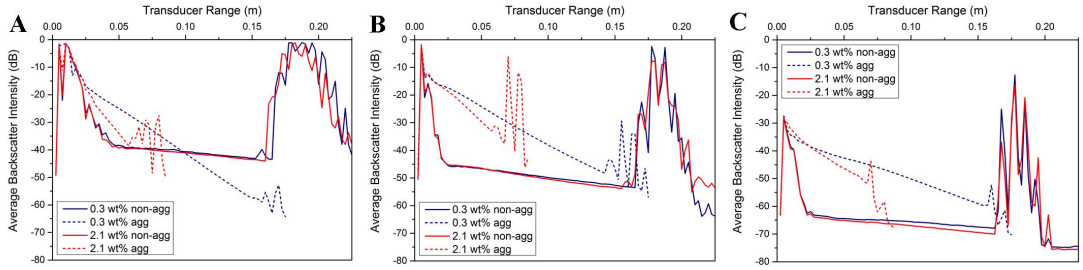

Figure 4.27: Comparison of aggregated and non-aggregated backscatter profiles at 0.3 wt% and 2.1 wt% via (a) 1 MHz, (b) 2 MHz and (c) 4 MHz.

A very interesting observation is made when comparing the intensity and attenuation between frequencies; 1, 2 and 4 MHz corresponding with A, B and C respectively. In the scattering of rigid particles, attenuation is enhanced with increasing frequency and has been observed in chapter 2 figure 2.6 and chapter 3 figure 3.5. Also as previously discussed in chapter 1 section 1.5 with respect to the scattering of soft particles, attenuation is also enhanced with increasing

frequency due to reduced overlap between neighbouring particle thermal layers. On the contrary, the aggregated profiles in A-C depict a counter-intuitive trend whereby the attenuation increases with decreasing frequency. At low frequency and correspondingly long wavelength, thermal layer overlap is enhanced so it is expected that attenuation via thermal losses would be reduced. But Hazlehurst *et al.* (2014), states that the actual proximity of particles strongly influences the scatter in the far-field region. In the case where the particles are touching $ka{\sim}1$, the thermal field behaves as that of a single larger particle. When distance is increased but the particles are still close in proximity, the far field is much larger $ka{\sim}2$ (refer to chapter 1 figure 1.9). In this aggregated structure, there are interactions with touching particles, particles adjacent to these in the aggregate structure and neighbouring particles in the dispersion. This deems a very strongly coupled network in which the aggregated particles may be behaving larger than they actually are. It is realistic to postulate that coupling could mediate very strong particle-particle interactions throughout the extended network, and thus various other factors could be influential in the attenuation.

Acoustic losses incurred via structural interactions are significant in this case. The network structure is governed by particle size, packing, shape and uniformity. When particles are joined together in a networked structure, additional energy dissipation is incurred via resulting oscillations of inter-particle bonds (Dukhin & Goetz, 1996). Since network interactions are greater at the lower frequency, this could be a key reason for the enhanced attenuation observed via the 1 MHz. There may also be increased potential for the occurrence of visco-inertial losses. Typically these are negligible where there is low density contrast between the mediums. Viscous skin depth is greater than thermal skin depth (introduced in chapter 1 section 1.5), both of which are in the hundred nanometre range. The electrokinetic mechanism is linked closely with the viscous mechanism (Dukhin & Goetz, 1996). It is also typically expected to have negligible effect on attenuation. However in this case, there is an extended networked structure which is also highly charged, the interactions of which are more strongly coupled at the lower frequency. These could result in a net increase in effective viscosity. Electroviscous effects are expected to vanish when the electric double layer thickness around the charged particle is small. However it is possible that its contribution is

greater in this extensive network (Booth, 1950). Details on acoustic mechanisms can be found in chapter 1 section 1.3.1.

This particular observation highlights the complexity associated with characterising such systems. Unfortunately in the present case the precise size, shape and structure of the aggregates is not known. Observations suggest that the aggregate structure may be more porous than expected and that the networked particles may be behaving larger than expected due to extensive thermal field overlapping. It is not possible to make a definitive postulation within the scope of this research. Nonetheless it has shown that the scattering of soft aggregates is strongly influenced by network interactions, which is contrary to current postulation for scattering of aggregated rigid particles, where it is thought that the influences of the individual particles within the structure are more influential (Vincent & MacDonald, 2015).The current status of soft matter acoustic theory has seen the recent publication of a multiple scattering theory for the advancement of the ECAH theoretical basis. This is essentially to account for the effects of multiple scatters which is introduced in high concentration regimes (Hazlehurst *et al.*, 2014). The incorporation for aggregated or flocculated particle interactions also requires further work (McClements *et al.*, 1998; Vincent & MacDonald, 2015). Much work needs to be done to understand the scattering via aggregated particles and to advance theoretical models for their incorporation in both the soft and rigid case. Here, a robust method has been established for the manufacture of monodisperse Latex beads which are readily aggregated such that these interactions can be studied via the ABS on a litre scale.

4.7.4 Comparison of Three Systems

The level of acoustic attenuation imparted in emulsified droplet and aggregated and non-aggregated particle dispersions systems are visualised by means of $\frac{dG}{dr}$ versus concentration in figure 4.28 A-C, for all frequencies. Note, although only two data plots are presented for the aggregated dispersion, a linear fit has been drawn between the points to give an indication of the likely possible linear gradient for comparative purposes only. The gradient of $\frac{\frac{dG}{dr}}{dM}$ steepens from, emulsion, Latex dispersion to aggregated suspension respectively. This trend is expected

since there is a density increase between the emulsion droplets and the Latex particles, then the aggregated dispersion exhibits marked inter-particle scattering.

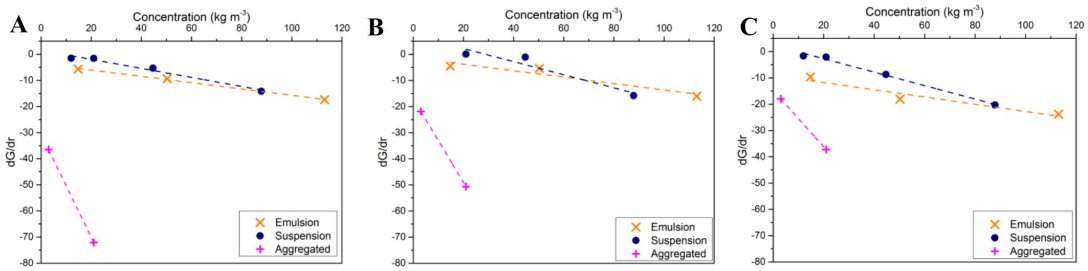

Figure 4.28: Comparison of attenuation-concentration relationship of emulsion, suspension and aggregated suspension via (a) 1 MHz, (b) 2 MHz and (c) 4 MHz

Measured values of distance averaged K_s and ξ are summarised in table 4.8 for the three systems. K_s values were not determined for the emulsion due to high variability, or in the aggregated dispersion due to attenuation in K_s values measured in the near-field. These systems have not previously been compared in this manner. The Rice method (Rice *et al.*, 2014) enabled direct measurement of attenuation, even in weakly attenuating dispersions. The attenuation constants depict the general expected increase with frequency (Rice *et al.*, 2014) for the emulsions and non-aggregated dispersions. Interestingly, the dispersions attenuate more strongly than the emulsions, althouth the correponding density of PMMA is slighlty higher and thus thermal attenuation is expected to be weaker. One possible explanation for this is that the constrast in thermal properties between PMMA and water is higher than that of MMA and water. Specifically the thermal conductivity and specific heat of PMMA, water and MMA are 0.17-0.19, 0.60 and 0.15 $W\,m^{-1}\,K$, and 1.4-1.5, 4.0 and 2.0 $J\,kg^{-1}\,K$ respectively. The aggregated dispersions are the strongest attenuators due to significant enhancement of inter-particle scattering events. However they do not follow the typical trend of attenuation increase with frequency. This is likely due to the highly networked structure of the thermally attenuating particles discussed earlier (section 4.7.3), which is not yet well understood.

Table 4.8: Backscattering and attenuation constants for the three particle systems with associated standard deviations.

System	Frequency (MHz)	K_s ($m\,kg^{-1/2}$)	σ	ξ ($kg^{-1}\,m^{-2}$)
Emulsion	1	-	-	0.0603
	2	-	-	0.0615
	4	-	-	0.0689
Non-Aggregated Dispersion	1	0.023	0.0007	0.0950
	2	0.032	0.008	0.1253
	4	0.046	0.014	0.1362
Aggregated Dispersion	1	-	-	0.9890
	2	-	-	0.8007
	4	-	-	0.5342

4.8 Latex Acoustics Summary

The backscatter profiles for emulsions, corresponding Latex and aggregated Latex dispersions were obtained and compared directly for the first time. The novel Rice method approach was taken for analysis in order to determine whether it is applicable in organic systems comprising soft particles. Although the soft particles are weak scatterers, they do attenuate, thus is was possible to determine attenuation constants for all systems via the Rice method. Backscattering constants were also calculated for the non-aggregated Latex dispersions.

The Rice approach enabled determination of the form function and normalised total scattering cross-section for Latex dispersions. Currently it is not known how well the empirical equations (Betteridge *et al.*, 2008; Thorne & Meral, 2008) describe the form function and normalised total scattering cross-section for low ka values since data are lacking (Vincent & MacDonald, 2015). There is increasing interest in the low ka range since it is postulated that the backscatter of large floc systems may be governed by that of the small aggregates from which they are comprised (Vincent & MacDonald, 2015). Indeed the low ka range is of interest for colloidal applications discussed here. The data obtained from particles in a very low ka region here, provide a means of investigating the validity of the

equations (refer to chapter 5) and filling the knowledge gap.

The backscatter intensity of the soft particles was markedly reduced compared to the rigid particles case since attenuation is governed by thermoacoustic scattering rather than visco-inertial. A marked increase in intensity and attenuation was exhibited in the aggregated case. In particular an interesting result was observed whereby enhanced attenuation was observed via the lowest frequency. It was postulated that this may be due to the enhanced inter-particle interactions in the networked structure when it is insonified via a frequency of longer wavelength. However further studies are required to better understand the backscatter response of aggregated structures both in the soft and rigid particle cases.

Chapter 5

Comparison of Particle Scattering Properties and Future Research Outlook

Chapter 5 is in two parts. First, the scattering properties of all the studied particle systems are compared directly. Specifically the data are collated to yield the form function f and total normalised scattering cross-section χ, in the very low ka region for the first time here. Importantly, these data show that f and χ do not align with the assumptions made in the Thorne model (Thorne & Hanes, 2002), in the Rayleigh scattering regime. This report then closes with a brief summary of the main conclusions, specifically with a view to further research.

5.1 Comparison of Measured Particle Scattering Properties in the Rayleigh Regime

A wide range of particle dispersion systems were investigated in Chapters 2 - 4; large glass bead scatterers, viscously attenuating irregularly shaped Barytes (inorganic mineral), thermally attenuating organic emulsions, Latex dispersions and aggregated Latex. In previous work, the author also investigated viscously attenuating colloidal Titania dispersions (Bux *et al.*, 2015). As discussed in chapter 1 section 1.4.1 and chapter 2 section 2.1, a particle's scattering and attenuating

properties are quantified by the form function f and total normalised scattering cross-section χ respectively. Here we compare these properties for all investigated particle systems in figure 5.1 A-B corresponding with χ and f respectively. There are no available published data at ka<1 for χ and ka<0.1 for f (Vincent & MacDonald, 2015), because it is not possible to sieve particle diameters below ~40 µm. Therefore, these data are invaluable because they provide insight into the form of the heuristic expressions for χ and f in the Rayleigh scattering region, albeit no clear trend is observed in these figures.

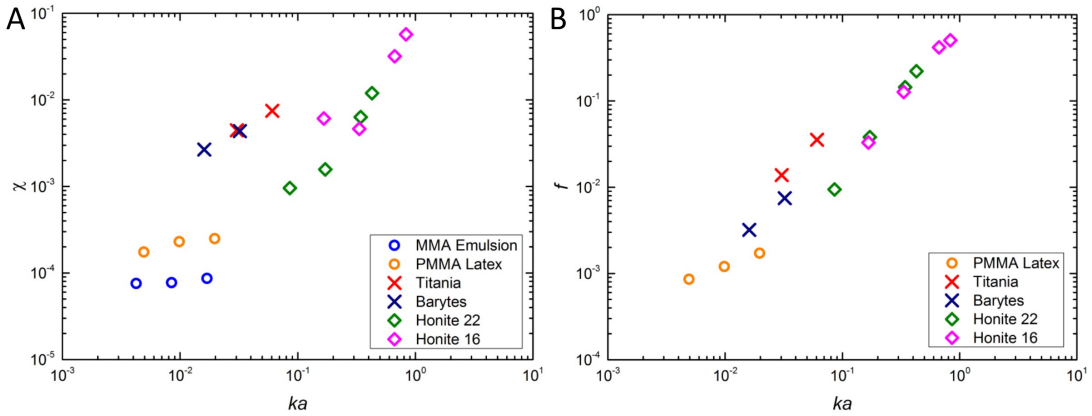

Figure 5.1: Measurement of (a) χ and (b) f in the low ka region.

Throughout investigations of each particle system, the significance of density with respect to particle scattering behaviour influences has been highlighted. Equation 1.4 denotes that V_{RMS} is proportional to α_s and K_s. Subsequently, α_s is proportional to $\frac{\chi}{\rho}$ (equation 1.11), and K_s is proportional to $f\sqrt{\rho}$ (equation 1.6). Therefore the scattering and attenuating properties of the various sediments can be directly compared by normalising the quantified χ and f by ρ and $\sqrt{\rho}$ respectively. Since χ and f are dimensionless parameters, it would seem prudent to normalise them with respect to specific gravity ϱ to retain non-dimensionality. This density normalisation approach has previously been utilised by (Moate & Thorne, 2012) to enable direct comparison of mineral sands with differing densities, see figure 5.2.

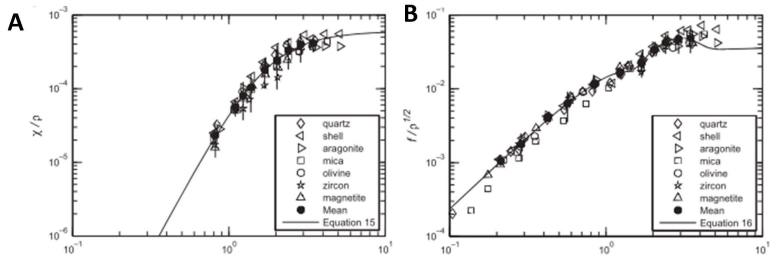

Figure 5.2: (a)χ and (b) f with respect to ka.

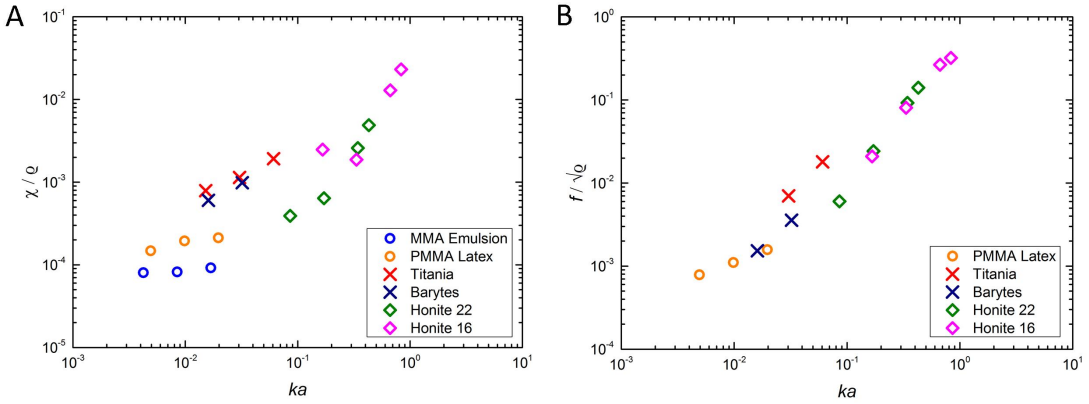

Figure 5.3: Measurement of (a) χ and (b) f normalised by $\sqrt{\varrho}$ and ϱ respectively.

Figure 5.3 presents the density normalised χ and f for the range of measured particle species. There is only a marginal improvement in the alignment of the data when normalised here, compared with the un-normalised version in figure 5.1. Note that the magnitude of the y axis values in figure 5.3 are offset with respect to those of the published data in figure 5.2. It is likely that the corresponding authors normalised via density rather than specific gravity, although they did not specify. However, normalising via the latter parameter is more appropriate in this case, since the units of the y axis retain non-dimensionality. Hence the data is presented as such. These data provide some key information with respect to the heuristic polynomial equations formed via the Thorne model (Thorne & Hanes, 2002). The form of the heuristic expressions as illustrated in figure 5.2 assume that the trend becomes linear for χ in the range $0.1<ka<1$,

however no data were acquired in that region to confirm this. For f, data was provided up to ka=0.1 and no further assumptions were made below this value. Markedly, figure 5.3A shows that the linear assumption made for χ, is incorrect. The figure 5.3 portrays an asymptotic tail off in the range $0.001<ka<1$ rather than a linear decay. Hence the heuristic equations do not describe the form of χ correctly in the Rayleigh scattering regime. Similarly, f also tails off in an asymptotic manner in the range $0.001<ka<1$. In fact, the asymptotic curve is more pronounced for f. Hence f also deviates from the heuristic equations in the Rayleigh scattering regime. Due to increasing interest in viscously attenuating particles, Vincent & MacDonald (2015) recently stated that it is not clear how well f and χ quantify particle scattering and attenuating at low ka values. These data are eye-opening and significant in that respect.

Finally in the interests of completeness, it would seem prudent to close the results discussion with a summary of key measured data comparing the scattering and attenuating properties of each particle system. Accordingly table 5.1 lists the backscattering constants K_s, and sediment attenuation constants, ξ, measured via the Rice method process (Rice *et al.*, 2014), for each particle type. Notably both K_s and ξ for all particles, (with the exception of aggregated Latex for reasons discussed in chapter 4 section 4.7.3), follow an expected increasing trend with respect to frequency (Thorne *et al.*, 1993). Each system is discussed henceforth.

- The MMA emulsions which comprise the smallest (droplet) size investigated, exhibited the weakest scatter and attenuation. Note there was a high degree of variability in calculating K_s due to the very weak backscatter intensity, so a definitive value could not be obtained. Given the weak backscatter response, the attenuation constant for the emulsion droplets is also low. Thermal absorption is the key contributor to attenuation for these soft droplets.

- K_s and ξ are also low for the polymerised Latex dispersions, inferring similar behaviour to the soft emulsions. However the attenuation constant is slightly higher than the less dense emulsions.

Table 5.1: Summary of measured K_s and ξ for all investigated particles

Particle	D_{50} (µm)	Density ($kg\,m^{-3}$)	Shape	f_r (MHz)	K_s ($m\,kg^{-1/2}$)	ξ ($kg^{-1}\,m^{-2}$)
MMA	2.0	940	spherical	1	-	0.060
Emulsion				2	-	0.062
				4	-	0.069
PMMA	2.3	1180	spherical	1	0.023	0.095
Latex				2	0.032	0.125
				4	0.046	0.136
PMMA	>15	-	-	1	-	0.989
Latex				2	-	0.801
Aggregated				4	-	0.534
Titania	7.2	3900	spheroidal[b]	2	0.117	0.238
				4	0.300	0.400
Barytes	7.9	4418	irregular	1	0.020	0.115
			jagged	2	0.060	0.189
Honite	40.5	2453	spherical	1	0.04	0.014
22				2	0.170	0.024
Glass				4	0.650	0.096
Beads				5	0.990	0.181
Honite	78.6	2470	spherical	1	0.110	0.047
16				2	0.410	0.036
Glass				4	1.340	0.247
Beads				5	1.620	0.441

[a] Calculations based on Thorne & Meral (2008) equations.

[b] Tightly bound spheroidal aggregates made up of $\sim 2\mu$m particles.

- The aggregated Latex dispersions exhibit the highest values for ξ. This is mainly due to inter-particle scattering events deflecting echoed pulses. Attenuation is also influenced by thermal losses which are due to overlapping of neighbouring particle layers in the aggregate structure. It is also thought that additional losses are incurred due to structural features. The scattering and attenuation mechanisms of these aggregated dispersions is highly

complex, and discussed in detail in chapter 4 section 4.7.3.

- Titania exhibits higher values for K_s than the emulsion and Latex dispersions. This is partly due to the slightly larger size, but mainly due to the markedly higher density associated with Titania. Values for ξ are also much higher. Since Titania is highly dense, attenuation is governed by visco-inertial losses. Viscous losses are greater than thermal losses.

- Barytes which is a similar size and density to Titania, exhibits slightly lower K_s values. Barytes particles are irregularly shaped jagged crystals. In the case of non-spherical shapes, the angle of incidence of the insonifying compression wave is key with respect to backscatter intensity (Moore *et al.*, 2013a), hence the probability of 180° reflections is lowered. ξ values for Barytes are also slightly lower than Titania. The Titania particles in this case are tightly bound spheroidal aggregates. It is likely that some inter-particle scattering of the aggregate would enhance the attenuation of titania slightly.

- The Honite 22 glass beads exhibit much higher values for K_s. These particles are much larger and thus much stronger scatterers than the previous colloidal systems. Values for ξ are also lower than the viscously attenuating Titania and Barytes particles. In this larger size range, the governing attenuating mechanism is that of scattering, where the larger scatterer leads to increased scattering at angles other than 180° (refer to chapter 1 figure 1.1).

- Honite 16 glass beads are the largest investigated particles. Hence they are the strongest scatterers, exhibiting the largest K_s values. ξ values are also slightly larger than those of Honite 22. Referring back to chapter 1 figure 1.2, we see that the scattering attenuation coefficient peaks and then decays with respect to particle size. Hence the reason there is an increase in ξ with size here.

5.2 Future Research Outlook

This report outlined the investigations of the characterisation of concentrated dispersions, via a novel *in situ* acoustic backscatter technique. Specifically the novelty lies in establishing a robust analysis protocol to characterise any arbitrary particle type in any concentration range up to the acoustic penetration depth limit. Characterisation included quantification of particle specific scattering and attenuation properties, dispersion concentration changes with time and settling kinetics in dynamic dispersions.

The Rice method (Rice *et al.*, 2014) was truly validated for quantification of the sediment specific attenuation constants of any arbitrary particle, via measurement in a range of particles with widely varying physical properties. The method was proven at a much larger depth scale than Rice's pipe-flows (Rice *et al.*, 2014, 2015b). A simple, rapid, robust protocol was established for the calibration of acoustic backscattering transducers. This enabled decoupling of K_t from K_s, thus enabled the quantification of K_s for any arbitrary particle for the first time here. Importantly the Rice method enables a simple quantification of f and χ via direct measurement. This is key because figure 5.3 clearly showed that the high order polynomial heuristic equations describing f and χ in the Thorne model, which assume linearity in the low Rayleigh scattering region, are in fact invalid for that range. Therefore the Rice direct measurement approach is more appropriate for small particles. It would be prudent to gather more data in the very low ka range so that the corresponding trends in f and χ can be further verified, especially since the Rayleigh scattering region is of increasing interest going forward.

The summary of key measured properties in table 5.1 is very eye-opening with respect to how particles of differing densities, size, shape and structure; scatter and attenuate the acoustic wave. From this information, initial prediction of the type of scattering behaviour can begin to be attempted, for different dispersions that may be of interest for characterisation. Importantly, it wasn't clear whether a measurable signal could be achieved in some cases such as colloidal particles, especially the thermally attenuating soft particles and droplets. However herein, it has been proven that it is possible to measure and characterise these systems, and as a consequence, the possible applications for this technique are vast. In

order to promote this, it would be ideal to expand on the information gathered in table 5.1 and build a database of the backscattering and attenuation constants including a number of common industrial and laboratory dispersions as well as systems which are of specific interest to a very specific application, for example nuclear legacy wastes. Such information would negate the need for specific calibrations in some cases and thus mediate rapid characterisation. It could also be used as a pre-measurement predictive step for scattering and attenuating behaviour to be expected from similar dispersion systems, thus enable prediction of penetration depth limitations.

Proving application of this method in a large scale industrial setting is yet another novelty highlighted in this report. Specifically it provided a quantification and an overall illustration of intricate dynamics during operations in a very complex tank system; sediment bed erosion, particle resuspension and settling kinetics both in local and wider locations in the tank. In the first instance, the ABS enabled qualitative monitoring capabilities, hence the true on-line monitoring nature of the instrument was demonstrated. The observed behaviours were subsequently quantified and verified via specific calibration with the dispersion in question. This work gave insight to enable predictive modelling of dynamics in the larger scale inaccessible radioactive tanks system based at Sellafield Ltd. The information is invaluable in terms of enabling the optimisation of daily operations and in the development of decommissioning strategies. For future development specifically relating to the nuclear industry, it would be necessary to test the ABS in a radioactive dispersion. Although the radioactivity itself is not likely to influence the acoustic response, such an exercise would be very insightful with respect to understanding how well non-active nuclear dispersion analogues and test materials correspond with the corresponding radioactive dispersions.

The commercial ABS utilised in this research has proven to be a very useful tool. However the main limitation in this work is associated with the achievable depth penetration. This in turn is directly related to the dispersion characteristics. Although the ABS has far greater penetration threshold than alternative light scattering methods, achieving flexibility is key for the development of a technique which can be applied in arbitrary dispersion systems. This feature can only be overcome by instrument design. For example some sort of transducer

array system for profiling, which can be adjusted for additional depth adjustment when required, and one that enables truly remote monitoring capabilities, would be ideal. As such, an ABS system which incorporates such features has recently been developed to incorporate improved flexibility (Cowell *et al.*, 2015). The instrument, is currently in the testing stages. Note that the development of this bespoke instrument is separate from, and beyond the scope of the work conducted in this report.

On a final note, *in situ* characterisation of weakly scattering, thermally attenuating soft organic dispersions was achieved at even low concentrations. The behaviour exhibited by the aggregated Latex dispersions, was very interesting and somewhat unexpected with respect to frequency. This work highlighted the truly complex nature of directly networked particle systems. It would seem that the behaviour of soft particle flocs would differ in some respects with respect to that of dense particle flocs. Both system types however are ill characterised. Flocculated structures are of ever increasing interest in numerous sedimentology (Vincent & MacDonald, 2015), and industrial applications (Hazlehurst *et al.*, 2014). The behaviour of soft flocs is of particular interest to the nuclear industry, where various organic flocs are encountered in legacy waste systems (Jackson *et al.*, 2014). In chapter 4, a very robust, efficient, novel protocol was established for the large litre scale manufacture of monodisperse Latex dispersions. This protocol will facilitate further research for the understanding of the ultrasonic scattering characteristics, of flocculated organic dispersions. Further research of these systems with the bespoke ABS instrument, coupled with the Rice characterisation and Hunter's empirical concentration analysis approach, is the key direction going forward.

Appendix A

Publications, Conferences & Industrial Contact

Publications, conference opportunities and industrial experiences arising directly from this research are listed herein.

A.1 Journal Papers

- Bux, J., Peakall, J., Biggs, S. & Hunter, T.N. (2015). *In situ* characterisation of a concentrated colloidal titanium dioxide settling suspension and associated bed development: Application of an acoustic backscatter system. *Powder Technology,* **284**, 530-540.

- Bux, J., Manga, M.S., Hunter, T.N. & Biggs, S. (2016). Manufacture of poly(methyl methacrylate) microspheres using membrane emulsification. *Philosophical Transcations A*, **In Press**.

- Bux, J., Paul, N., Dodds, J.M., Peakall, J., Biggs, S. & Hunter, T.N. (2016). *In situ* characterization of sedimentation dynamics in a jet ballast tank: application of an ABS. *Journal of the American Institute of Chemical Engineers*, **In Preparation**.

- Bux, J., Rice, H.P., Peakall, J., Biggs, S. & Hunter, T.N. (2016). Measurement of the backscattering and attenuation constants of particle with

a range of densities, in low ka scattering regimes. *Journal of the Acoustical Society of America*, **In Preparation**.

A.2 Conference Papers

- Bux, J., Paul, N., Dodds, J.M., Peakall, J., Biggs, S. & Hunter, T.N., Acoustic *in situ* characterisation of a nuclear test material suspension, in impinging jet ballast tanks; a laboratory calibration. *IChemE Sustainable Nuclear Energy Conference*, 9-11 April 2014, Manchester, UK.

- Bux, J., Paul, N., Dodds, J.M., Peakall, J., Biggs, S. & Hunter, T.N., *in situ* characterisation of mobilization, dispersion and re-settling in impinging jet ballast tanks with an acoustic backscatter system. *Waste Management Symposium 2014*, 2-6 March 2014, Phoenix, Arizona, USA. http://www.wmsym.org/archives/2014/papers/14097.pdf.

- Bux, J., Paul, N., Dodds, J.M., Peakall, J., Biggs, S. & Hunter, T.N., Characterising nuclear simulant suspensions *in situ* with an acoustic backscatter system - extended abstract. *ICEM*, 8-12 September 2013, Brussels, Belgium. doi:10.1115/ICEM2013-96088.

- Bux, J., Hunter, T.N., Peakall, J. & Biggs, S., A Novel Acoustic Backscatter System Application: Characterising Settling Suspensions *In Situ*, *Separations 2013*, 21-23 June 2013, Falmouth, Cornwall, UK.

A.3 Conferences

- **Oral Presentation**; Nuclear Decommisioning Authority PhD Student Conference, January 2016.

- **Oral Presentation**, Up-scaling crossflow membrane emulsification & polymerization, and *in situ* acoustic characterization of the colloidal dispersions; 6th Asian Conference on Colloid and Interface Science, 24-27 November 2015, Sasebo, Japan.

- **Attended, some research herein presented by supervisor**; Soft interfacial materials: from fundamentals to formulation, Royal Society, London, UK.
- **Oral Presentation**, IChemE Sustainable Nuclear Energy Conference, 9-11 April 2014, Manchester, UK.
- **Oral Presentation**; Waste Management Symposium 2014, 2-6 March 2014, Phoenix, Arizona, USA.
- **Oral Presentation**; NDA PhD Student Conference, January 2014.
- **Oral Presentation**; ASME - 15th International Conference on Environmental Remediation and Radioactive Waste Management, 8-12 September 2013, Brussels, Belgium.
- **Oral Presentation**; Separations 2013, 21-23 June 2013, Falmouth, Cornwall, UK.
- **Poster Presentation**; NDA PhD Student Conference, January 2013.
- **Poster Presentation**; Research Frontiers in Radioactive Waste Management Symposium, 10 October 2012, Sheffield, UK. Awarded prize for best poster from academic section.
- **Attended**; DIAMOND 2012 Conference, 11-12 December 2012, Coventry, UK.

A.4 Research Related Work Experience

- **Nuclear Site Work Experience**; THORP Management Centre, Sellafield Ltd, April 2014, Cumbria, UK.
- **Acoustics Work Experience**; National Physical Laboratory, March 2013, London, UK.
- **Nuclear site tours**; Low Level Waste Repository & Sellafield Ltd, February 2013, Cumbria, UK.

- **Oral Presentation**; Sellafield Sludge Working Group Meeting, October 2013, Cumbria, UK.
- **Calibration experiments with Thorne group**; National Oceanography Centre, Dec 2012, Liverpool, UK.
- **Test probes in water thickener**; Yorkshire Water, July 2012, South Yorkshire, UK.
- **Industrial Experiments**; National Nuclear Laboratory, May 2012, December 2012, May 2013, Cumbria, UK.

Appendix B

Bessel and Hankel Functions

$$f_m = \frac{2}{ix}\sum_{n=0}^{\infty}(2n+1)(-1)^n b_n \qquad \chi = \frac{2}{x^2}\sum_{n=0}^{\infty}(2n+1)|b_n|^2$$

The value for b_n as determined by *Gaunaurd and Uberall* [1983] is given by

$$b_n = \frac{\begin{vmatrix}\beta_1 & \alpha_{12} & \alpha_{13}\\ \beta_2 & \alpha_{22} & \alpha_{23}\\ 0 & \alpha_{32} & \alpha_{33}\end{vmatrix}}{\begin{vmatrix}\alpha_{11} & \alpha_{12} & \alpha_{13}\\ \alpha_{21} & \alpha_{22} & \alpha_{23}\\ 0 & \alpha_{32} & \alpha_{33}\end{vmatrix}}$$

where

$$x = ka_s \qquad x_t = x\frac{c}{c_t} \qquad x_l = x\frac{c}{c_l}$$

where j_n and h_n are spherical Bessel functions of the first and third kind and the prime denotes differentiation with respect to the argument. c is the velocity of sound in the water, and c_l and c_t are the compression and shear wave velocities, respectively, in the sphere. k is the wave number in the water, a_s is the sphere radius, and ρ and ρ_s are the density of the water and sphere.

$$\beta_1 = -x_t^2\frac{\rho}{\rho_s}j_n(x) \qquad \beta_2 = xj_n'(x)$$

$$\alpha_{11} = x_t^2\frac{\rho}{\rho_s}h_n^{(1)}(x) \qquad \alpha_{21} = -xh_n^{(1)\prime}(x)$$

$$\alpha_{12} = [2n(n+1) - x_t^2]j_n(x_l) - 4x_l j_n'(x_l)$$

$$\alpha_{22} = x_l j_n'(x_l) \qquad \alpha_{32} = 2[j_n(x_l) - x_l j_n'(x_l)]$$

$$\alpha_{13} = 2n(n+1)[x_t j_n'(x_t) - j_n(x_t)]$$

$$\alpha_{23} = n(n+1)j_n(x_t)$$

$$\alpha_{33} = 2x_t j_n'(x_t) + [x_t^2 - 2n(n+1) + 2]j_n(x_t)$$

Spherical Bessel and Hankel functions for the form function f and the total normalised scattering cross-section χ, with corresponding solutions, from Thorne *et al.* (1993).

References

Admiraal, D. & Garcia, M. (2000). Laboratory measurement of suspended sediment concentration using an acoustic concentration profiler (acp). *Experiments in fluids*, **28**, 116–127. 17

Ainslie, M.A. & McColm, J.G. (1998). A simplified formula for viscous and chemical absorption in sea water. *The Journal of the Acoustical Society of America*, **103**, 1671–1672. 21

Allegra, J. & Hawley, S. (1972). Attenuation of sound in suspensions and emulsions: theory and experiments. *The Journal of the Acoustical Society of America*, **51**, 1545–1564. 16, 17

Arshady, R. & Ledwith, A. (1983). Suspension polymerisation and its application to the preparation of polymer supports. *Reactive Polymers, Ion Exchangers, Sorbents*, **1**, 159–174. 119, 128, 137, 141

Atkinson, C. & Kytömaa, H. (1992). Acoustic wave speed and attenuation in suspensions. *International Journal of multiphase flow*, **18**, 577–592. 17

Austin, J.C. & Challis, R.E. (1998). The effects of flocculation on the propagation of ultrasound in dilute kaolin slurries. *Journal of colloid and interface science*, **206**, 146–157. 29, 30, 108, 144

Balastre, M., Argillier, J., Allain, C. & Foissy, A. (2002). Role of polyelectrolyte dispersant in the settling behaviour of barium sulphate suspension. *Colloids and Surfaces A: Physicochemical and Engineering Aspects*, **211**, 145–156. 5, 86, 90, 105

Berot, S., Giraudet, S., Riaublanc, A., Anton, M. & Popineau, Y. (2003). Key factors in membrane emulsification. *Chemical Engineering Research and Design*, **81**, 1077–1082. 135

Best, J.L., Kostaschuk, R.A., Peakall, J., Villard, P.V. & Franklin, M. (2005). Whole flow field dynamics and velocity pulsing within natural sediment-laden underflows. *Geology*, **33**, 765–768. 7

Betancourt, F., Bürger, R., Diehl, S. & Farås, S. (2014). Modeling and controlling clarifier–thickeners fed by suspensions with time-dependent properties. *Minerals Engineering*, **62**, 91–101. 2

Betteridge, K.F., Thorne, P.D. & Cooke, R.D. (2008). Calibrating multi-frequency acoustic backscatter systems for studying near-bed suspended sediment transport processes. *Continental Shelf Research*, **28**, 227–235. vi, xiii, 21, 35, 36, 39, 41, 45, 46, 48, 50, 57, 58, 59, 61, 62, 63, 64, 65, 66, 67, 152, 158

Biggs, S. & Grieser, F. (1995). Preparation of polystyrene latex with ultrasonic initiation. *Macromolecules*, **28**, 4877–4882. 109

Bolton, G., Bennett, M., Wang, M., Qiu, C., Wright, M., Primrose, K., Stanley, S. & Rhodes, D. (2007). Development of an electrical tomographic system for operation in a remote, acidic and radioactive environment. *Chemical Engineering Journal*, **130**, 165–169. 6

Booth, F. (1950). The electroviscous effect for suspensions of solid spherical particles. *Proceedings of the Royal Society of London A: Mathematical, Physical and Engineering Sciences*, **203**, 533–551. 156

Brooks, B. (2010). Suspension polymerization processes. *Chemical Engineering & Technology*, **33**, 1737–1744. xvii, 119, 124

Burns, J.L., Yan, Y.d., Jameson, G.J. & Biggs, S. (1997). A light scattering study of the fractal aggregation behavior of a model colloidal system. *Langmuir*, **13**, 6413–6420. 108

Bux, J., Peakall, J., Biggs, S. & Hunter, T.N. (2015). In situ characterisation of a concentrated colloidal titanium dioxide settling suspension and associated bed development: Application of an acoustic backscatter system. *Powder Technology*, **284**, 530–540. xiii, 8, 9, 24, 25, 26, 27, 28, 45, 72, 79, 90, 91, 125, 149, 150, 160

Carlson, J. & Martinsson, P.E. (2002). A simple scattering model for measuring particle mass fractions in multiphase flows. *Ultrasonics*, **39**, 585–590. xiii, 12, 18, 19

Challis, R., Povey, M., Mather, M. & Holmes, A. (2005). Ultrasound techniques for characterizing colloidal dispersions. *Reports on progress in physics*, **68**, 1541. 1, 6, 7, 10, 11, 12, 13, 29, 46, 149, 150

Chanamai, R., Coupland, J.N. & McClements, D.J. (1998). Effect of temperature on the ultrasonic properties of oil-in-water emulsions. *Colloids and Surfaces A: Physicochemical and Engineering Aspects*, **139**, 241–250. 43

Charcosset, C., Limayem, I. & Fessi, H. (2004). The membrane emulsification processa review. *Journal of chemical technology and biotechnology*, **79**, 209–218. 110, 118

Cheung, M.K., Powell, R.L. & McCarthy, M.J. (1996). Sedimentation of noncolloidal bidisperse suspensions. *AIChE journal*, **42**, 271–276. 2

Chu, C., Ju, S., Lee, D., Tiller, F.M., Mohanty, K. & Chang, Y. (2002). Batch settling of flocculated clay slurry. *Industrial & engineering chemistry research*, **41**, 1227–1233. 6

Cowell, D.M., Freear, S., Smith, I., Rice, H.P., Hunter, T.N., Njobuenwu, D., Fairweather, M., Peakall, J., Barnes, M. & Randall, G. (2015). Development of a real-time acoustic backscatter system for solids concentration measurement during nuclear waste cleanup. *Ultrasonics Symposium (IUS), 2015 IEEE International*, 1–4. 168

Crawford, A. & Hay, A.E. (1993). Determining suspended sand size and concentration from multifrequency acoustic backscatter. *The Journal of the Acoustical Society of America*, **94**, 3312–3324. 38

Cunningham, M.F. (2008). Controlled/living radical polymerization in aqueous dispersed systems. *Progress in polymer science*, **33**, 365–398. 119

De Clercq, J., Nopens, I., Defrancq, J. & Vanrolleghem, P.A. (2008). Extending and calibrating a mechanistic hindered and compression settling model for activated sludge using in-depth batch experiments. *Water research*, **42**, 781–791. 2, 5, 10, 26

De Luca, G., Sindona, A., Giorno, L. & Drioli, E. (2004). Quantitative analysis of coupling effects in cross-flow membrane emulsification. *Journal of membrane science*, **229**, 199–209. 106, 110

De Luca, G., Di Maio, F.P., Di Renzo, A. & Drioli, E. (2008). Droplet detachment in cross-flow membrane emulsification: comparison among torque- and force-based models. *Chemical Engineering and Processing: Process Intensification*, **47**, 1150–1158. 112, 130, 132

Deboeuf, A., Gauthier, G., Martin, J. & Salin, D. (2011). Segregation and periodic mixing in a fluidized bidisperse suspension. *New Journal of Physics*, **13**, 075005. 2

Dodds, J. (2015). Personal communication. Tech. rep., National Nuclear Laboratory - Email Received [2015-07-08]. xvi, 93

Dowding, P.J. & Vincent, B. (2000). Suspension polymerisation to form polymer beads. *Colloids and Surfaces A: Physicochemical and Engineering Aspects*, **161**, 259–269. 119, 120, 124, 138

Downing, A., Thorne, P.D. & Vincent, C.E. (1995). Backscattering from a suspension in the near field of a piston transducer. *The Journal of the Acoustical Society of America*, **97**, 1614–1620. 6, 20

Dragosavac, M.M., Sovilj, M.N., Kosvintsev, S.R., Holdich, R.G. & Vladisavljević, G.T. (2008). Controlled production of oil-in-water emulsions containing unrefined pumpkin seed oil using stirred cell membrane emulsification. *Journal of Membrane Science*, **322**, 178–188. 110

Dukhin, A. & Goetz, P. (2002). *Ultrasound for Characterizing Colloids*. Elsevier. 15

Dukhin, A.S. & Goetz, P.J. (1996). Acoustic and electroacoustic spectroscopy. *Langmuir*, **12**, 4336–4344. 10, 11, 13, 17, 155

Dukhin, A.S. & Goetz, P.J. (2001). Acoustic and electroacoustic spectroscopy for characterizing concentrated dispersions and emulsions. *Advances in Colloid and Interface Science*, **92**, 73–132. 2, 7, 8, 11, 15, 18, 42, 149, 152

Epstein, P.S. & Carhart, R.R. (1953). The absorption of sound in suspensions and emulsions. i. water fog in air. *The Journal of the Acoustical Society of America*, **25**, 553–565. 16

Finlayson, B. (1985). Field calibration of a recording turbidity meter. *Catena*, **12**, 141–147. 5

Fugate, D.C. & Friedrichs, C.T. (2002). Determining concentration and fall velocity of estuarine particle populations using adv, obs and lisst. *Continental Shelf Research*, **22**, 1867–1886. 5, 7, 8

Furlan, J.M., Mundla, V., Kadambi, J., Hoyt, N., Visintainer, R. & Addie, G. (2012). Development of a-scan ultrasound technique for measuring local particle concentration in slurry flows. *Powder technology*, **215**, 174–184. 18, 19

Gartner, J.W. (2004). Estimating suspended solids concentrations from backscatter intensity measured by acoustic doppler current profiler in san francisco bay, california. *Marine Geology*, **211**, 169–187. 7

Gartner, J.W., Cheng, R.T., Wang, P.F. & Richter, K. (2001). Laboratory and field evaluations of the lisst-100 instrument for suspended particle size determinations. *Marine Geology*, **175**, 199–219. 5

Gaunaurd, G. & Überall, H. (1983). Rst analysis of monostatic and bistatic acoustic echoes from an elastic sphere. *The Journal of the Acoustical Society of America*, **73**, 1–12. 37, 38

Gaunaurd, G., Huang, H. & Strifors, H. (1995). Acoustic scattering by a pair of spheres. *The Journal of the Acoustical Society of America*, **98**, 495–507. 16

Gijsbertsen-Abrahamse, A.J., Van der Padt, A. & Boom, R.M. (2004). Status of cross-flow membrane emulsification and outlook for industrial application. *Journal of Membrane Science*, **230**, 149–159. 109, 116, 125, 135

Goldburg, W. (1999). Dynamic light scattering. *American Journal of Physics*, **67**, 1152–1160. 5

Greenwood, M.S., Mai, J.L. & Good, M.S. (1993). Attenuation measurements of ultrasound in a kaolin–water slurry: a linear dependence upon frequency. *The Journal of the Acoustical Society of America*, **94**, 908–916. 15

Gregson, C.R., Hastings, J.J., Sims, H.E., Steele, H.M. & Taylor, R.J. (2011). Characterisation of plutonium species in alkaline liquors sampled from a uk legacy nuclear fuel storage pond. *Analytical Methods*, **3**, 1957–1968. 3, 4, 108

Gu, H., Duits, M.H. & Mugele, F. (2011). Droplets formation and merging in two-phase flow microfluidics. *International journal of molecular sciences*, **12**, 2572–2597. 114

Ha, H., Hsu, W.Y., Maa, J.Y., Shao, Y. & Holland, C. (2009). Using adv backscatter strength for measuring suspended cohesive sediment concentration. *Continental Shelf Research*, **29**, 1310–1316. 8

Hancocks, R., Spyropoulos, F. & Norton, I. (2013). Comparisons between membranes for use in cross flow membrane emulsification. *Journal of Food Engineering*, **116**, 382–389. xvii, 112

Hardy, R., Best, J., Parsons, D. & Keevil, G. (2011). On determining the geometric and kinematic characteristics of coherent flow structures over a gravel bed: a new approach using combined plif-piv. *Earth Surface Processes and Landforms*, **36**, 279–284. 5

Harker, A. & Temple, J. (1988). Velocity and attenuation of ultrasound in suspensions of particles in fluids. *Journal of Physics D: Applied Physics*, **21**, 1576. 16, 17

Hastings, J., Rhodes, D., Fellerman, A., Mckendrick, D. & Dixon, C. (2007). New approaches for sludge management in the nuclear industry. *Powder technology*, **174**, 18–24. 3, 4

Hay, A.E. (1991). Sound scattering from a particle-laden, turbulent jet. *The Journal of the Acoustical Society of America*, **90**, 2055–2074. 14, 15, 17

Haynes, W.M. (2014). *CRC handbook of chemistry and physics*. CRC press. 75

Haynes, W.M. (2015). *CRC handbook of chemistry and physics: a ready-reference book of chemical and physical data*. CRC Press, Boca Raton, Florida, 96th edn. 122

Hazlehurst, T.A., Harlen, O.G., Holmes, M.J. & Povey, M.J.W. (2014). Multiple scattering in dispersions, for long wavelength thermoacoustic solutions. *Journal of Physics: Conference Series*, **498**, 012005. xiv, 1, 2, 11, 16, 17, 29, 30, 149, 150, 155, 156, 168

Hernando, L., Omari, A. & Reungoat, D. (2015). Experimental investigation of batch sedimentation of concentrated bidisperse suspensions. *Powder Technology*, **275**, 273–279. 2, 5

Holdich, R.G., Dragosavac, M.M., Vladisavljevic, G.T. & Kosvintsev, S.R. (2010). Membrane emulsification with oscillating and stationary membranes. *Industrial & Engineering Chemistry Research*, **49**, 3810–3817. 110

Holmes, A.K., Challis, R.E. & Wedlock, D.J. (1993). A wide bandwidth study of ultrasound velocity and attenuation in suspensions: comparison of theory with experimental measurements. *Journal of colloid and interface science*, **156**, 261–268. 7, 28, 108

Hosseini, S., Patel, D., Ein-Mozaffari, F. & Mehrvar, M. (2010). Study of solid-liquid mixing in agitated tanks through electrical resistance tomography. *Chemical Engineering Science*, **65**, 1374–1384. 5

Hoyos, M., Bacri, J., Martin, J. & Salin, D. (1994). A study of the sedimentation of noncolloidal bidisperse, concentrated suspensions by an acoustic technique. *Physics of Fluids (1994-present)*, **6**, 3809–3817. 2

Hubner, T., Will, S. & Leipertz, A. (2001). Sedimentation image analysis (sia) for the simultaneous determination of particle mass density and particle size. *Particle & Particle Systems Characterization*, **18**, 70–78. 5

Hunter, T., Peakall, J. & Biggs, S. (2011). Ultrasonic velocimetry for the in situ characterisation of particulate settling and sedimentation. *Minerals Engineering*, **24**, 416–423. 2, 8

Hunter, T.N., Darlison, L., Peakall, J. & Biggs, S. (2012a). Using a multi-frequency acoustic backscatter system as an in situ high concentration dispersion monitor. *Chemical Engineering Science*, **80**, 409–418. xiii, 2, 9, 15, 17, 23, 24, 26, 27, 28, 32, 43, 50, 53, 54, 55, 72, 79, 80, 90, 154

Hunter, T.N., Peakall, J. & Biggs, S. (2012b). An acoustic backscatter system for in situ concentration profiling of settling flocculated dispersions. *Minerals Engineering*, **27**, 20–27. 26, 30, 31, 108, 150

Hunter, T.N., Unsworth, T., Acun, M., Peakall, J., Keevil, G. & Biggs, S. (2012c). Measuring erosion and dispersion of sediment beds in impinging-jet ballast tanks, using ultrasonic profilers. *Nuclear Fuel Cycle Conference*. 71, 93, 94, 98, 99

Hunter, T.N., Peakall, J., Unsworth, T.J., Acun, M.H., Keevil, G., Rice, H. & Biggs, S. (2013). The influence of system scale on impinging jet sediment erosion: Observed using novel and standard measurement techniques. *Chemical Engineering research and design*, **91**, 722–734. 70, 71

Iritani, E., Hashimoto, T. & Katagiri, N. (2009). Gravity consolidation–sedimentation behaviors of concentrated tio 2 suspension. *Chemical Engineering Science*, **64**, 4414–4423. 2, 5, 10, 26, 106

Isakovich, M. (1948). On the propagation of sound in emulsions. *Zh. Exper. I Teor. Fiz*, **18**, 907–912. 16

Jackson, S.F., Monk, S.D. & Riaz, Z. (2014). An investigation towards real time dose rate monitoring, and fuel rod detection in a first generation magnox storage pond (fgmsp). *Applied Radiation and Isotopes*, **94**, 254–259. 4, 108, 168

Jahanzad, F., Sajjadi, S. & Brooks, B.W. (2005). Characteristic intervals in suspension polymerisation reactors: an experimental and modelling study. *Chemical engineering science*, **60**, 5574–5589. 124, 128

Jaworski, A. & Bolton, G. (2000). The design of an electrical capacitance tomography sensor for use with media of high dielectric permittivity. *Measurement Science and Technology*, **11**, 743. 5

Joscelyne, S.M. & Trägårdh, G. (2000). Membrane emulsificationa literature review. *Journal of Membrane Science*, **169**, 107–117. xvii, 110, 111, 116, 124, 125, 134, 135

Kaushal, D. & Tomita, Y. (2007). Experimental investigation for near-wall lift of coarser particles in slurry pipeline using γ-ray densitometer. *Powder technology*, **172**, 177–187. 6

Kresse, R., Baudis, U., Jger, P., Riechers, H., Wagner, H., Winkler, J. & Wolf, H. (2000). *Ullmann's Encyclopedia of Industrial Chemistry*. Wiley-VCH Verlag GmbH & Co. KGaA. 71

Kricheldorf, H. (1991). *Handbook of Polymer Synthesis Part A*. Marcel Dekker, Inc. 140

Lawler, D.M. & Brown, R.M. (1992). A simple and inexpensive turbidity meter for the estimation of suspended sediment concentrations. *Hydrological processes*, **6**, 159–168. 5

Lepercq-Bost, É., Giorgi, M.L., Isambert, A. & Arnaud, C. (2008). Use of the capillary number for the prediction of droplet size in membrane emulsification. *Journal of membrane science*, **314**, 76–89. 131, 132, 133

Lepercq-Bost, É., Giorgi, M.L., Isambert, A. & Arnaud, C. (2010). Estimating the risk of coalescence in membrane emulsification. *Journal of Membrane Science*, **357**, 36–46. 131, 133, 134

Li, Y., Liu, G., Xu, J., Wang, K. & Luo, G. (2015). A microdevice for producing monodispersed droplets under a jetting flow. *RSC Advances*, **5**, 27356–27364. 113, 132

Libicki, C., Bedford, K.W. & Lynch, J.F. (1989). The interpretation and evaluation of a 3-mhz acoustic backscatter device for measuring benthic boundary layer sediment dynamics. *The Journal of the Acoustical Society of America*, **85**, 1501–1511. 9, 44

Lloyd, P. & Berry, M. (1967). Wave propagation through an assembly of spheres: Iv. relations between different multiple scattering theories. *Proceedings of the Physical Society*, **91**, 678. 16

Lynch, J.F., Irish, J.D., Sherwood, C.R. & Agrawal, Y.C. (1994). Determining suspended sediment particle size information from acoustical and optical backscatter measurements. *Continental Shelf Research*, **14**, 1139–1165. 5

Ma, G.H., Nagai, M. & Omi, S. (1999). Effect of lauryl alcohol on morphology of uniform polystyrene–poly (methyl methacrylate) composite microspheres prepared by porous glass membrane emulsification technique. *Journal of colloid and interface science*, **219**, 110–128. 122

Ma, G.H., Nagai, M. & Omi, S. (2001). Study on preparation of monodispersed poly(styrene-co-n-dimethylaminoethyl methacrylate) composite microspheres by spg (shirasu porous glass) emulsification technique. *Journal of Applied Polymer Science*, **79**, 2408–2424. 120, 124, 136

MacDonald, I.T., Vincent, C.E., Thorne, P.D. & Moate, B.D. (2013). Acoustic scattering from a suspension of flocculated sediments. *Journal of Geophysical Research: Oceans*, **118**, 2581–2594. 31, 108

Manga, M.S., Cayre, O.J., Williams, R.A., Biggs, S. & York, D.W. (2012). Production of solid-stabilised emulsions through rotational membrane emulsification: influence of particle adsorption kinetics. *Soft Matter*, **8**, 1532–1538. 110

McArthur, G.A., Tinsley, T.P. & McKendrick, D. (2005). Development of a liquid jet sludge re-suspension model (used on pulse jets or jet ballasts). *AIChE Annual Meeting, Conference Proceedings*. xv, xvi, 71, 95, 96, 97

McClements, D., Herrmann, N. & Hemar, Y. (1998). Influence of flocculation on the ultrasonic properties of emulsions: theory. *Journal of Physics D: Applied Physics*, **31**, 2950. 29, 30, 31, 108, 156

McClements, D.J. (1991). Ultrasonic characterisation of emulsions and suspensions. *Advances in Colloid and Interface Science*, **37**, 33–72. 2, 7, 28, 29, 42, 108, 152

McClements, D.J. (1994). Ultrasonic determination of depletion flocculation in oil-in-water emulsions containing a non-ionic surfactant. *Colloids and Surfaces A: Physicochemical and Engineering Aspects*, **90**, 25–35. 30, 108

Meinhart, C.D., Wereley, S.T. & Santiago, J.G. (1999). Piv measurements of a microchannel flow. *Experiments in fluids*, **27**, 414–419. 5

Meral, R. (2008). Laboratory evaluation of acoustic backscatter and lisst methods for measurements of suspended sediments. *Sensors*, **8**, 979–993. 5, 7, 9, 19, 42

MET-FLOW (2002). User manual: Uvp monitor model uvp-duo with software version 3. revision 5 ed. x, **1**, 1–1. xiii, 19, 42

Meyer, R.F. & Crocker, J.C. (2009). Universal dripping and jetting in a transverse shear flow. *Departmental Papers (CBE)*, 128. xvii, 114, 132, 134

Mi, Y., Zhou, W., Li, Q., Gong, F., Zhang, R., Ma, G. & Su, Z. (2015). Preparation of water-in-oil emulsions using a hydrophobic polymer membrane with 3d bicontinuous skeleton structure. *Journal of Membrane Science*, **490**, 113–119. 117

Moate, B.D. & Thorne, P.D. (2012). Interpreting acoustic backscatter from suspended sediments of different and mixed mineralogical composition. *Continental Shelf Research*, **46**, 67–82. 152, 161

Moore, S., Le Coz, J., Hurther, D. & Paquier, A. (2013a). Using multi-frequency acoustic attenuation to monitor grain size and concentration of suspended sediment in rivers. *The Journal of the Acoustical Society of America*, **133**, 1959–1970. xiii, 8, 9, 12, 13, 17, 24, 29, 50, 53, 74, 75, 165

Moore, S.A., Dramais, G., Dussouillez, P., Le Coz, J., Rennie, C. & Camenen, B. (2013b). Acoustic measurements of the spatial distribution of suspended sediment at three sites on the lower mekong river. *The Journal of the Acoustical Society of America*, **133**, 3227–3227. 19

Nakashima, T., Shimizu, M. & Kukizaki, M. (1992). Membrane emulsification by microporous glass. In *Key Engineering Materials*, vol. 61, 513–516, Trans Tech Publ. 110, 117

Napper, D. (1983). *Polymeric Stabalization of Colloidal Dispersions*. Academic Press. 121, 122, 141, 142, 144

Norisuye, T. (2016). Structures and dynamics of microparticles in suspension studied using ultrasound scattering techniques. *Polymer International*. 2, 10, 18

Nuisin, R., Omi, S. & Kiatkamjornwong, S. (2006). The effects of acrylate monomers and polystyrene addition on the morphology of dop-plasticized styrene–acrylate polymer particles prepared by spg emulsification and suspension polymerization. *Journal of applied polymer science*, **99**, 1195–1206. 118

Nunes, J., Tsai, S., Wan, J. & Stone, H. (2013). Dripping and jetting in microfluidic multiphase flows applied to particle and fibre synthesis. *Journal of physics D: Applied physics*, **46**, 114002. 111, 112, 113, 114, 133

of Trade & Industy, D. (2002). Managing the nuclear legacy, a strategy for action whitepaper 2002. Tech. rep., [Accessed 01-05-2016] http://webarchive.nationalarchives.gov.uk/+/http:/www.dti.gov.uk/nuclear cleanup/ach/whitepaper.pdf. 3

Omi, S., Katami, K., Yamamoto, A. & Iso, M. (1994). Synthesis of polymeric microspheres employing spg emulsification technique. *Journal of applied polymer science*, **51**, 1–11. 110, 118, 120, 124, 138

Omi, S., Katami, K., Taguchi, T., Kaneko, K. & Iso, M. (1995). Synthesis of uniform pmma microspheres employing modified spg (shirasu porous glass) emulsification technique. *Journal of applied polymer science*, **57**, 1013–1024. 118, 120, 122, 124

Omi, S., Ma, G.H. & Nagai, M. (2000). Membrane emulsification a versatile tool for the synthesis of polymeric microspheres. *Macromolecular Symposia*, **151**, 319–330. 117

Paul, N., Biggs, S., Edmondson, M., Hunter, T.N. & Hammond, R.B. (2013). Characterising highly active nuclear waste simulants. *Chemical Engineering Research and Design*, **91**, 742–751. 70, 71, 73, 75

Peakall, J. & Warburton, J. (1996). Surface tension in small hydraulic river models-the significance of the weber number. *Journal of Hydrology New Zealand*, **35**, 199–212. 114

Pellam, J.R. & Galt, J. (1946). Ultrasonic propagation in liquids: I. application of pulse technique to velocity and absorption measurements at 15 megacycles. *The journal of chemical physics*, **14**, 608–614. 16

Peng, S. & Williams, R.A. (1998). Controlled production of emulsions using a crossflow membrane: Part i: Droplet formation from a single pore. *Chemical Engineering Research and Design*, **76**, 894–901. xvii, 110, 113, 115, 116, 118, 127, 130

Powell, M.R., Onishi, Y. & Shekarriz, R. (1997). Research on jet mixing of settled sludges in nuclear waste tanks at hanford and other doe sites: A historical perspective. Tech. rep., Pacific Northwest Lab., Richland, WA (United States). 71

Rayleigh, L. (1897). On the incidence of aerial and electric waves upon small obstacles in the form of ellipsoids or elliptic cylinders and on the passage of electric waves through a circular aperture in a conducting screen. *Phil. Mag. XLIV*, **226**, 28–52. 16

Rehman, S.S. & Vincent, C. (1990). Underwater acoustic measurement of suspended sediments: the calibration of a high-frequency acoustic backscatter meter. *Geol. Bull. Univ. Peshawar*, **161**. 44

Rice, H.P., Fairweather, M., Hunter, T.N., Mahmoud, B., Biggs, S. & Peakall, J. (2014). Measuring particle concentration in multiphase pipe flow using acoustic backscatter: Generalization of the dual-frequency inversion method. *The Journal of the Acoustical Society of America*, **136**, 156–169. vi, xiii, 8, 9, 17, 23, 27, 28, 32, 33, 34, 35, 36, 40, 50, 51, 54, 57, 58, 61, 62, 63, 65, 66, 81, 90, 157, 163, 166

Rice, H.P., Fairweather, M., Peakall, J., Hunter, T.N., Mahmoud, B. & Biggs, S.R. (2015a). Measurement of particle concentration in horizontal, multiphase pipe flow using acoustic methods: Limiting concentration and the effect of attenuation. *Chemical Engineering Science*, **126**, 745–758. 28, 32

Rice, H.P., Fairweather, M., Peakall, J., Hunter, T.N., Mahmoud, B. & Biggs, S.R. (2015b). Particle concentration measurement and flow regime identification in multiphase pipe flow using a generalised dual-frequency inversion method. *Procedia Engineering*, **102**, 986–995. 28, 166

Richards, S. & Leighton, T. (2001). Acoustic sensor performance in coastal waters: solid suspensions and bubbles. *Proceedings Institute of Acoustics*, **23**, 399–406. 76

Richards, S., Heathershaw, A. & Thorne, P. (1996). The effect of suspended particulate matter on sound attenuation in seawater. *The Journal of the Acoustical Society of America*, **100**, 1447–1450. 17

Richardson, D. & Holdich, R. (2001). A novel and low cost probe for monitoring dispersed solids concentrations in liquids. *Chemical Engineering Research and Design*, **79**, 569–574. 5

Rose, C.P. & Thorne, P.D. (2001). Measurements of suspended sediment transport parameters in a tidal estuary. *Continental Shelf Research*, **21**, 1551–1575. 9, 22, 40

Rossing, T.E. (2007). *Springer Handbook of Acoustics*. Springer. 43

Rouhnia, M., Keyvani, A. & Strom, K. (2014). Do changes in the size of mud flocs affect the acoustic backscatter values recorded by a vector adv? *Continental Shelf Research*, **84**, 84–92. 108

Santos, J., Vladisavljević, G.T., Holdich, R.G., Dragosavac, M.M. & Muñoz, J. (2015). Controlled production of eco-friendly emulsions using direct and premix membrane emulsification. *Chemical Engineering Research and Design*, **98**, 59–69. 110, 133

Schaafsma, A.S. & Hay, A.E. (1997). Attenuation in suspensions of irregularly shaped sediment particles: A two-parameter equivalent spherical scatterer model. *The Journal of the Acoustical Society of America*, **102**, 1485–1502. 39

Sewell, C.J.T. (1910). The extinction of sound in a viscous atmosphere by small obstacles of cylindrical and spherical form. *Trans. Roy. Soc. London A*, **210**, 239–270. 16

Sheng, J. & Hay, A.E. (1988). An examination of the spherical scatterer approximation in aqueous suspensions of sand. *The Journal of the Acoustical Society of America*, **83**, 598–610. 15, 38

Shukla, A., Prakash, A. & Rohani, S. (2007). Particles settling studies using ultrasonic techniques. *Powder Technology*, **177**, 102–111. 2, 4

Shukla, A., Prakash, A. & Rohani, S. (2010). Particle size monitoring in dense suspension using ultrasound with an improved model accounting for low-angle scattering. *AIChE journal*, **56**, 2825–2837. 13, 14, 15

Simons, J., Keurentjes, J. & Meuldijk, J. (2013). Micron-sized polymer particles by membrane emulsification. *Macromolecular Symposia*, **333**, 102–112. 110, 134, 136, 139, 140, 141

Spyropoulos, F., Lloyd, D.M., Hancocks, R.D. & Pawlik, A.K. (2014). Advances in membrane emulsification. part b: recent developments in modelling and scale-up approaches. *Journal of the Science of Food and Agriculture*, **94**, 628–638. 111, 134

Sung, C., Huang, Y., Lai, J. & Hwang, G. (2008). Ultrasonic measurement of suspended sediment concentrations: an experimental validation of the approach using kaolin suspensions and reservoir sediments under variable thermal conditions. *Hydrological processes*, **22**, 3149–3154. 14, 15

Tanguchi, J., Murata, H. & Okamura, Y. (2010). Analysis of aggregation and dispersion states of small particles in concentrated suspension by using diffused photon density wave spectroscopy. *Colloids and Surfaces B: Biointerfaces*, **76**, 137–144. 5

Tebbutt, J. & Challis, R. (1996). Ultrasonic wave propagation in colloidal suspensions and emulsions: a comparison of four models. *Ultrasonics*, **34**, 363–368. xiii, 14, 16, 17, 28, 108, 152

Temkin, S. (1998). Sound propagation in dilute suspensions of rigid particles. *The Journal of the Acoustical Society of America*, **103**, 838–849. 2, 6, 17

Temkin, S. (2005). *Suspension acoustics: An introduction to the physics of suspensions*. Cambridge University Press. 9, 10, 43, 53

Thorne, P.D. & Buckingham, M.J. (2004). Measurements of scattering by suspensions of irregularly shaped sand particles and comparison with a single parameter modified sphere model. *The Journal of the Acoustical Society of America*, **116**, 2876–2889. 39

Thorne, P.D. & Hanes, D.M. (2002). A review of acoustic measurement of small-scale sediment processes. *Continental Shelf Research*, **22**, 603–632. 2, 7, 9, 17, 18, 19, 20, 22, 23, 33, 35, 36, 40, 44, 46, 51, 58, 59, 62, 67, 160, 162

Thorne, P.D. & Hardcastle, P.J. (1997). Acoustic measurements of suspended sediments in turbulent currents and comparison with in-situ samples. *The Journal of the Acoustical Society of America*, **101**, 2603–2614. 36

Thorne, P.D. & Meral, R. (2008). Formulations for the scattering properties of suspended sandy sediments for use in the application of acoustics to sediment transport processes. *Continental Shelf Research*, **28**, 309–317. 37, 38, 39, 41, 57, 58, 61, 62, 63, 64, 65, 66, 67, 152, 158, 164

Thorne, P.D., Hardcastle, P.J. & Soulsby, R.L. (1993). Analysis of acoustic measurements of suspended sediments. *Journal of Geophysical Research: Oceans*, **98**, 899–910. 14, 15, 36, 37, 38, 40, 63, 152, 163, 173

Thorne, P.D., Hurther, D. & Moate, B.D. (2011). Acoustic inversions for measuring boundary layer suspended sediment processes. *The Journal of the Acoustical Society of America*, **130**, 1188–1200. 17, 19, 23

Thorne, P.D., MacDonald, I.T. & Vincent, C.E. (2014). Modelling acoustic scattering by suspended flocculating sediments. *Continental Shelf Research*, **88**, 81–91. 31, 108

Topping, D., Wright, S., Melis, T. & Rubin, D. (2007). High-resolution measurements of suspended-sediment concentration and grain size in the colorado river in grand canyon using a multi-frequency acoustic system. *Proceedings of the 10th International Symposium on River Sedimentation*, **3**, 470. 19

Urick, R. (1948). The absorption of sound in suspensions of irregular particles. *The Journal of the acoustical society of America*, **20**, 283–289. 14, 15, 17

Urick, R. & Ament, W. (1949). The propagation of sound in composite media. *The Journal of the Acoustical Society of America*, **21**, 115–119. 16, 17

Utada, A., Chu, L.Y., Fernandez-Nieves, A., Link, D., Holtze, C. & Weitz, D. (2007). Dripping, jetting, drops, and wetting: the magic of microfluidics. *Mrs Bulletin*, **32**, 702–708. 113

Vincent, C.E. & MacDonald, I.T. (2015). A flocculi model for the acoustic scattering from flocs. *Continental Shelf Research*, **104**, 15–24. 31, 56, 108, 152, 156, 158, 161, 163, 168

Vladisavljević, G.T. & Williams, R.A. (2005). Recent developments in manufacturing emulsions and particulate products using membranes. *Advances in colloid and interface science*, **113**, 1–20. xvii, 110, 116, 117, 124

Wang, M., Ma, Y., Holliday, N., Dai, Y., Williams, R.A. & Lucas, G. (2005). A high-performance eit system. *Sensors Journal, IEEE*, **5**, 289–299. 6

Waterman, P.C. & Truell, R. (1961). Multiple scattering of waves. *Journal of Mathematical Physics*, **2**, 512–537. 16

Weser, R., Woeckel, S., Wessely, B., Steinmann, U., Babick, F. & Stintz, M. (2014). Ultrasonic backscattering method for in-situ characterisation of concentrated dispersions. *Powder Technology*, **268**, 177–190. 2, 9, 10, 18

Wheeler, J. & Chatterji, S. (1972). Settling of particles in fresh cement pastes. *Journal of the American Ceramic Society*, **55**, 461–464. 6

Williams, R., Xie, C., Bragg, R. & Amarasinghe, W. (1990). Experimental techniques for monitoring sedimentation in optically opaque suspensions. *Colloids and surfaces*, **43**, 1–32. 4, 6

Williams, R., Peng, S., Wheeler, D., Morley, N., Taylor, D., Whalley, M. & Houldsworth, D. (1998). Controlled production of emulsions using a crossflow membrane: part ii: industrial scale manufacture. *Chemical Engineering Research and Design*, **76**, 902–910. xvii, 110, 111, 115, 116, 118, 125, 132

Wolska, J. & Bryjak, M. (2009). Preparation of poly (styrene-co-divinylbenzene) microspheres by membrane emulsification. *Desalination*, **241**, 331–336. 118, 120, 124, 135, 138

Xia, H., Ishii, K. & Iwai, T. (2005). Hydrodynamic radius sizing of nanoparticles in dense polydisperse media by low-coherence dynamic light scattering. *Japanese journal of applied physics*, **44**, 6261. 5

Yuan, Q., Hou, R., Aryanti, N., Williams, R.A., Biggs, S., Lawson, S., Silgram, H., Sarkar, M. & Birch, R. (2008). Manufacture of controlled emulsions and particulates using membrane emulsification. *Desalination*, **224**, 215–220. 118, 120, 122, 127, 132

Yuan, Q., Cayre, O.J., Manga, M., Williams, R.A. & Biggs, S. (2010). Preparation of particle-stabilized emulsions using membrane emulsification. *Soft Matter*, **6**, 1580–1588. xvii, 117, 118, 120, 122, 126, 127, 132

Zou, X.j., Ma, Z.m., Zhao, X.h., Hu, X.y. & Tao, W.l. (2014). B-scan ultrasound imaging measurement of suspended sediment concentration and its vertical distribution. *Measurement Science and Technology*, **25**, 115303. 2, 10, 18